Dottorato di Ricerca in Ingegneria per la Gestione delle Acque e del Territorio (XXIV° ciclo)

Politecnico di Torino

Marzo 2012

Combined finite-discrete element modelling of key instabilities which characterise deep-seated landslides from massive rock slope failure

....
Giovanna Piovano
Author

....
Prof. Giovanni Barla
Advisor

....
Dott. Ing. Marco Barla
Advisor

....
Prof. Claudio Scavia
Head of the Ph.D. Programme in Geotechnical Engineering

Arriving at one point is the starting point to another.
JOHN DEWEY

Abstract

The expression "landslide from massive rock slope failure" (MRSF) is used to indicate large-scale landslides characterised by a variety of complex initial failure processes and unpredictable postfailure behaviour. In this context, deep-seated landslides are classified as "landslides from massive rock slope failure". Typically, deep-seated landslides are slow mountain deformations which may involve movement along discrete shear surfaces and deep seated mass creep.

The long-term development of deep-seated slope deformations creates suitable conditions for the subsequent occurrence of other slope deformations. Deep-seated landslides in mountain areas can be spatially interconnected with other types of slope deformations such as debris flows, debris slides, rock avalanches, topple, translational, rotational and compound sliding and complex type of mass movements.

It is to be recognized that many aspects of large-scale landslides need be investigated in order to gain the necessary confidence in the understanding and prediction of their behaviour and in the associated risk assessment. The present thesis is to contribute to such understanding with specific reference to a number of mass movements which characterize large-scale landslides.

An advanced numerical technique (FDEM) which combines finite elements with discrete elements has been applied in this thesis for improving such understanding. The open source research code, called Y2D, developed at the Queen Mary, University of London by Prof. Munjiza has been used. Considering that this code has not yet been applied to slope stability problems, a series of numerical tests have been carried out to assess its suitability to properly and efficiently simulate geomechanical problems.

To this purpose standard rock failure mechanisms as well as laboratory tests have been modelled first and the results obtained have been compared with available analytical and numerical solutions. The advantages of the application of FDEM has been outlined by showing that both the simulation of failure initiation and progressive development to fragmentation of the rock mass is possible as this is deposited at the slope toe. The case study of interest for this thesis is the Beauregard massive landslide located in the Aosta Valley (Northwestern Italy). At this site the presence of an extensive deep-landslide insisting on the left abutment of an arch-gravity dam is well recognised.

Based on detailed studies, the investigated area has been subdivided into zones which are characterised by different geomorphologic and geostructural features. Different landslide mechanics as well as different landslide activities upstream of the dam site have been identified and studied in detail.

Such an area is thought to be at an intermediate stage of development of the deep seated landslide compared with the sector which insists on the dam. The observed failure mechanism has been ascribed to a large sliding on a compound surface. Some other failure mechanisms have been recognized, such as large flexural toppling and local block toppling instability.

The final part of the thesis has been devoted to the FDEM numerical modelling of a large scale failure mechanism based on brittle behaviour of the rock mass. The aim is to apply the "total slope failure" approach through the application of FDEM. Such a technique has demonstrated the significant potential in predicting the development of possible slope instability phenomena.

Keywords: rock mechanics; slope stability; numerical modelling; FEM and FDEM.

Acknowledgements

First of all, I wish to express my gratitude to my tutor Professor Giovanni Barla, Professor of Rock Mechanics. He has always been an inspiration and a motivator. He taught me the art of rock engineering and numerical modelling. I truly enjoyed working in his research group.

I would also like to thank my advisor Doctor Marco Barla for his attentive solicitations and constant monitoring of my work. It was a great pleasure working with him. He contributes to many discussions that helped me in the research work.

I am specially grateful to Professor Giovanni Grasselli for giving me the opportunity to work with him and for the help during my stay in Canada. He also encourages me to pursue this research project. I wish to also acknowledge my colleagues at the University of Toronto, Andrea Lisjak and Omid K. Mahabadi, for the valuable theoretical and practical help in resolving modeling issues. Thank you for the answers, always so rapid.

I would also like to acknowledge the helpful suggestions from Professor Ante Munjiza, who introduced and supported me into the numerical analyses with the Y code. Thank you also for the help during my period in London.

My gratitude goes to my colleagues Alessia, Maria Elena and Francesco. You have been real friends. Thank you. Special thanks goes to my colleagues Nino and Qingrui for the time we spent together during the final year of the PhD program. Your friendship has helped me to complete my PhD research. These acknowledgements would not be complete without mentioning all my colleagues with whom I shared these years of work at the Department of Structural, Geotechnical and Building Engineering.

Last, but not least, I wish to thank my family who offered unconditional support and encouragement, and have always been there for me. This dissertation is lovely dedicated to them.

And, at the end, thanks to myself.

Contents

Chapter 1

Introduction

1.1 Framework

The expression "landslide from massive rock slope failure" (MRSF) is used by several authors to indicate large-scale landslides characterized by a variety of complex initial failure processes and unpredictable post-failure behaviour. A MRSF is frequently a multiple phase landslide characterized by primary and secondary processes: primary processes include transformation of movements mechanism, substantial changes in volume and changes in the characteristics of the moving mass; secondary processes are important aspects of the phenomena and may be instantaneous or delayed and extend the impact of a landslide beyond the boundaries of the primary landslide and may themselves result in catastrophic consequences.

The deep-seated landslides are classified as a type of "landslide from massive rock slope failure". The importance the deep-seated landslides is that they occur in many parts of the world and impact very significantly on infrastructures and on society. Many aspects of deep-seated landslides are poorly understood and need be investigated in order to gain the necessary confidence in predicting their behaviour. This is due to the many complexities of the phenomena which encompass the understanding of the underlying mechanisms, the initial and post-failure behaviour, and the different secondary processes resulting from instability.

1.2 Problem Statement

The areas affected by deep-seated landslides (DSGSD) are characterised by a high degree of rock mass subdivision. DSGSD disrupt bedrock, generates discontinuities and change slope morphology resulting in superficial reactivations of morphologically unstable segments of slopes, such as old steep landslide scarps and forefront parts of rotated and gravitationally subsided blocks. Generally, this activation concerns a relatively small part of the volume of a DSGSD, but it tends to have highly destructive consequences. Deep-seated landslides are associated with rocks which exhibit marked strength anisotropy such as shale, schist, gneiss, micaschist, slate etc.

A long-term development of deep-seated lanslides (in the order of thousands of years) creates suitable conditions for the subsequent occurrence of a wide range of other slope deformations. Rockfalls, rock avalanches, debris flows, rockslides and shallow translational and rotational landslides, flexural and block toppling are often the results of older deep-seated gravitational slope deformations.

1.3 Scope and objective

The scope of the present thesis is to contribute to the study of the landslides from massive rock slope failure by using the combined finite-discrete element method. The considered case study is the deep-seated gravitational slope deformation on the left slope of the Valgrisenche valley where the Beauregard dam was located. The occurrence of several instability mechanisms including sliding of large slope sectors on rotational or compound surfaces, rockfalls and topples (block and flexural) have been recognised on the landslide.

Attention has been focused firstly on the numerical technique used. The numerical code Y2D adopted for simulation, is based on the combined finite-discrete element method and have been developed by Munjiza (2004). It is a two-dimensional research code capable of modelling continuum and discontinuum behaviour. Considering that such a code has not yet been applied to slope stability problems, a series of numerical tests have been carried out to assess its suitability to properly and efficiently simulate geomechanical problems. This work has contributed to the development of Y2D and the implementation of new algorithms which allow to apply the code for rock slope stability analysis.

The following tasks have been undertaken:

- a preliminary study on massive landslides, with indication of major morphological features and modes of instability;

- detailed bibliographic study of conventional and advanced numerical techniques used in rock slope stability analysis; attention has been focused on the general formulation of continuum and discontinuum methods and on the description of principal algorithms of the combined finite-discrete element method;
- a validation of the Y2D code, with emphasis on the principal modes of failure characteristic of slope stability; numerical analysis of some laboratory tests performed on jointed rock samples to evaluate the effect of anisotropy on rock strength;
- numerical analysis of the instability modes which characterise the Beauregard Landslide.

1.4 Organization of thesis

This thesis is divided into 8 chapters. The present chapter is intended to provide a general introduction to the subject. Chapter 2 presents a general review of landslides associated with massive rock slope failure in order to introduce the main topic, such as deep-seated landslides from massive rock slope failure. Chapter 3 focuses on the numerical approach proposed by several authors to investigate failure mechanisms of rock slopes. A review of numerical techniques used in rock slope stability analysis is done, with emphasis on the use of the combined continuum-discontinuum numerical modelling technique. Chapter 4 is devoted to the description of the combined finite-discrete element method and its general formulation in terms of principal algorithmic solutions. Chapter 5 illustrates a series of numerical tests carried out to to provide a validation of the Y2D code, a numerical code based on the combined finite-discrete element method, which has been used in the present thesis. Chapter 6 is devoted to the description of the Beauregard Landslide and some of the characteristic instability modes. These selected types of instability are taken as case study. Chapter 7 illustrates the numerical simulations carried out and finally Chapter 8 draws some conclusions and suggestions for further work.

Chapter 2

Landslides from massive rock slope failure

2.1 Introduction

Landslides resulting from large-scale massive rock slope failure are an important geological hazard in many parts of the world, especially in mountainous regions, and have been responsible for some of the most destructive natural disasters in the world history. In the 20th century, disasters caused by massive rock slope failure have killed more than 50000 people. Massive rock slope failures occur with measurable frequency in the mountains of the world; based on twentieth century data, massive rock slope failures involving volumes equal or greater than 20 Mm^3 occur every 2.7 years (Evans, 2006).

A comprehensive review has been carried out in this chapter, in order to attempt a critical analysis of the state-of-the-art on catastrophic massive landslides. In the present literature a wide range of research papers have been published to describe the morphological features of this type of landslides, but also a great number of case histories have been studied and the literature contains many examples of catastrophic massive landslides from all around the world.

A general review of the range of landslides associated with massive rock slope failure is first described in order to introduce the main topic of the chapter, such as deep-seated landslides from massive rock slope failure.

2.2 Massive Rock Slope Failure

In the specialised literature, the expression “landslide from massive rock slope failure” (MRSF) is used by several authors to indicate large-scale landslides characterized by a variety of complex initial failure processes and unpredictable post-failure behaviour (Evans et al., 2006).

Several classification schemes for sub-aerial failures have been proposed over the past few decades; those most frequently mentioned are the slope movement types and processes according to the classifications proposed by Hoek and Bray (1977), Varnes (1958, 1978), Hutchinson (1988), Cruden and Varnes (1996), Hungr et al. (2001). In these classifications, complete unanimity does not exist, but there is wide agreement for massive, non-volcanic, rock slope failures (Hutchinson, 2006).

In the introduction to the NATO Advanced Research Workshop on *“Massive Rock Slope Failure: New Models for Hazard Assessment”* (Celano, Italy 16-21 June 2002), Evans et al. (2006) proposed a reviewed classification of landslides resulting from massive rock slope failure. The MRSF includes:

- Catastrophic Rockslides (see section 2.2.1);
- Catastrophic Spreads (see section 2.2.2);
- Rock Avalanches (see section 2.2.3);
- Rockfalls (see section 2.2.4);
- Catastrophic Debris Flows (see section 2.2.5);
- Landslide from Volcanoes (see section 2.2.6) ;
- Slow Mountain Slope Deformations (see section 2.2.7).

Hutchinson (2006) suggests that failures affecting volcanoes should be most conveniently treated as a separate category.

In this context, Evans et al. (2006) proposed the term “massive” to describe exceptionally large massive rock slope failure. In fact, the range of volume mobilized in massive landslides cover at least five orders of magnitude between 10^5 and 10^{10} m^3.

A MRSF is frequently a multiple phase landslide characterized by primary and secondary processes. A wide range of primary processes are involved in massive rock slope failure which include transformation of movements mechanism, substantial changes in volume and changes in the characteristics of the moving mass. For example, a disintegrating rock mass involved in an initial rockslide becomes transformed into a massive, rapid debris flow which travels well beyond expected limits. Besides, secondary processes associated with massive rock slope failure are important aspects of the phenomena. Catastrophic secondary effects may be instantaneous or delayed and extend the impact of a landslide beyond the boundaries of the primary landslide and may themselves result in catastrophic consequences. The landslide-generated waves and displaced water effects are examples of secondary processes.

The following description of several types of massive rock slope failure is mainly based on the review work made by Evans et al. (2006) for the introduction of the Celano Workshop.

2.2.1 Catastrophic Rockslides

Evans et al. (2006) define a rockslide like a landslide originated from an initial bedrock slope failure. In a rockslide a significant amount of debris remains on the initial sliding surface; usually the slide mass is subjected to an incomplete disintegration and the distance of travel is limited.

A rockslide characterized by high velocity is defined as a "catastrophic rockslide". In a catastrophic rockslide, the initial failure is usually characterized by a drastic initial strength loss through such processes as brittleness of internal shears, or passive failure of intact rock in the toe region of the landslide. Catastrophic failure could occur on a sharply curved pre-existing sliding surface and the debris peak velocity can reach even 20-30 m/s. Although emplaced rapidly, rockslide debris frequently contains massive transported blocks of relatively undisturbed bedrock. The vertical displacement of the centre of gravity of the slide mass may be relatively small despite the high velocity required.

2.2.2 Catastrophic Spreads

Spreads are another kind of catastrophic bedrock slope instability; the typical geological setting suitable for spreads instability is where a thickness of hard resistant caprock overlies weaker softer ductile rocks, such as tuffs, shales, marine clays or flysch sediments. Failure occurs as deformation in the subjacent weak rock layer which often results in tensile failure of caprock. This kind of instability may involve toppling and spreading of the subjacent weak layer and has catastrophic potential, because once the first signs of instability of the caprock occurred, the collapse can suddenly take place. Catastrophic spreads are common in layered volcanic rocks where the caprock is lava, and in the thrust and nappe belts of the European Alps and the Rocky Mountains of North America, where the cap rock is frequently overthrust Proterozoic or Paleozoic limestone and the subjacent material is Cretaceous shale (Evans et al., 2006).

2.2.3 Rock Avalanches

In 1904, the term “rock avalanche” was first used by several authors to describe the 1903 Frank Slide in the Alberta Rocky Mountains (Evans et al., 2006). A rock avalanche is a bedrock failure characterized by the complete fragmentation of the rock mass which leaves this original topographic surface completely, and travels a downslope distance far from its origin.

Rock avalanches are extremely rapid movements. Several authors estimated the mean velocity of a rock avalanche; in the 1970 Huascaran event, a mean velocity of about 75 m/s with peak velocities perhaps as high as 280 m/s, was estimated based on the analysis of the ballistic trajectory of huge granodiorite blocks. Some rock avalanches generate destructive winds and travel so rapidly that generate winds that not only felled mature trees but drove spear-shaped wood fragments into solid tree trunks along its margins (1984 Mount Cayley rock avalanche). Authors demonstrate that wind velocities in excess of 30 m/s are required to inflict this type of damage on mature pine trees.

During a rock avalanche the debris may exhibit high mobility effects in different ways such as abrupt changes in the direction of travel; they may run at right angles or even turn a full 180° to the original movement direction. The debris may run over significant obstacles in its path or run-up a considerable distance on opposing valley sides.

2.2.4 Rockfalls

Rockfalls involve the fall of a rock mass following initial detachment from a very steep rock slope, its disintegration and subsequent movement which may involve bouncing, rolling, or sliding generally down the steep source rock slope (Evans et al., 2006). Massive rockfalls frequently transform into highly mobile debris flows or rock avalanches.

The so called “fragmental rockfalls” are characterised by independent movement of individual rock fragments; usually these type of rockfalls are characterised by a threshold volume which varies with the source material. In hard non-porous rocks it is about 1 Mm^3 and in soft porous rocks it is about 500000 Mm^3.

Although rockfalls, thus defined, are much smaller than rock avalanches and rock slides they are more frequent and may be highly destructive over a limited area. Rockfalls may attain high velocities and the impact of large blocks detached from a cliff may be very catastrophic and in some cases they may generate a wind blast. Rockfalls are the most frequent landslide type triggered by earthquakes.

2.2.5 Debris Flows induced by rockslope failure

When a debris from a rockslope failure impacts on channel or valley floor sediments, a destructive debris flow may be mobilized that travels well beyond the margins of the initial landslide debris. This style of debris flow travels rapidly downslope (over 40 m/s). Further, the volume of entrained material from the landslide path may significantly enhance the volume involved in the initial rock slope failure. Splash zones are sometimes formed around the debris by fluidized material displaced from beneath the debris and compressional deformation structures may be formed in sediments beneath or adjacent to the debris sheet (Evans et al., 2006).

Similar effects may result from impacts of rockfall debris on saturated colluvium or talus forming the lower part of a valley side slope. Such responses of valley sediments and valley side deposits suggest that the impact loading of saturated materials can generate pore pressures which reduce the frictional resistance at the base of the moving debris; undrained loading generated by rapidly moving debris may thus be an important mechanism in explaining the anomalous mobility of certain rock avalanches and rockfall events.

2.2.6 Landslides from Volcanoes

Volcanoes are highly unstable piles of eruptive products and often are subjected to landslide activity, either in association with volcanic eruptions or during periods of quiescence. Landslides from volcanoes include large-scale flank collapses and smaller scale landslides (volcanic debris avalanches) involving part of the edifice. Sometimes these massive rock slope failures are transformed into lahars (volcanic debris flows).

Flank collapses are massive catastrophic failures of the volcanic edifice itself. Flank collapses may be triggered by magma emplacement, local tectonic displacements, oversteepening and overloading by the deposition of eruptive products, oversteepening and incision of the edifice by stream erosion, the generation of pore pressures generated as a result of magma intrusion or seismic shaking.

Smaller scale landslides also occur on the slopes of volcanoes without involving the failure of a large part of the volcano's superstructure. Initial failure volumes are typically less than 100 Mm^3 and commonly involve mechanically weak pyroclastic debris or hydrothermally altered rocks. Because of this, the "rock" mass involved in initial failure is easily fragmented and quickly becomes transformed into a rapidly moving rock or debris avalanche. Volcanic landslides of this type may be triggered by an eruption, small steam explosions, earthquake shaking, heavy rains, or glacier unloading.

Lahars are commonly associated with eruptions and may be triggered by a variety of processes including the snow or glacier ice melting by hot ejecta, the ejection, or breaching of the waters of a crater or caldera lake, the transformation of glowing ash avalanches, pyroclastic surges, or the transformation of an eruption-triggered flank collapse - debris avalanche.

2.2.7 Slow Mountain Slope Deformations

Mountain slope deformation consists of slow, deep-seated movement of a large rock mass which commonly exhibits loosening and fracturing in the sub-surface and signs of displacement on the surface of the slope itself (Evans et al., 2006). The process is termed “gravitational spreading” by Varnes et al. (1989) and "sagging” by Hutchinson (1988) who regards it as an early phase in the development of deep-seated landslides.

This style of slope movement may involve movement along discrete shear surfaces and deep seated mass creep. It is commonly manifested in topographic features such as cracks, fissures, trenches, antislope (counter) scarps at mid or upper slope locations, and, in some cases, slope bulging at lower slope locations. These linear geomorphic features may be collectively termed “sackungen”, after the German word for “sagging” (McCalpin and Irvine, 1995). Frequently, these surface features occur without well defined headscarps, lateral scarps, or lateral shear zones suggesting that slope movement is occurring without the formation of well defined shear surfaces in contrast to rockslides described earlier.

Mountain slope deformation features (or sackungen) present difficulties in landslide hazard assessment for several reasons:

- the precise movement mechanism is difficult to establish and thus to analyse;
- the potential for the development of catastrophic detachment is difficult to evaluate;
- the relationship to tectonic processes may be complex;
- the origin of the linears themselves may be problematic (i.e. whether they represent a tectonic fault formed by an earthquake or a response to mountain slope deformation, is not always clear; this issue is complicated by the fact that many examples of deep seated slope deformation occur in close association with pre-existing faults which may themselves be active).

Large-scale non-catastrophic rockslides are common in many mountainous areas of the world, particularly in metamorphic rocks. Rates of movement may be in the range of 1-2 mm/year. The precise mechanism of mountain slope deformation is difficult to establish even at sites that have been extensively studied.

Where the geological structure is favourable, mountain slope deformation involves some degree of toppling or sliding movement of a slope that has been previously disturbed by toppling. A major problem in the interpretation of massive rock slope movements is the prediction of the future behaviour of the slope and the establishment of conditions that determine the transition to possible catastrophic failure once ongoing mountain slope deformation has been detected. For example, it happens that a rock avalanche can take place in a slope that had undergone significant non-catastrophic deformation in the post-glacial period (1987 Valtellina rock avalanche). In the literature, the boundary between non-catastrophic ductile flexural toppling and catastrophic brittle block toppling has been examined by Nichol et al. (2002).

2.3 Initial rock slope failure

The initial rock slope failure of massive landslide depends on predisposing geological factors including lithology, particularly the presence of argillaceous strata, the presence of faults, slope angle and structural controls. In addition, periglacial disturbance and the melting of permafrost, glacial or fluvial erosion, hydrogeological and meteorological factors, neotectonics and seismicity, and both surface and hydrothermal weathering are factors causing slope instability (Hutchinson, 2006).

In *bedrock slope*, the mode of initial failure is strongly controlled by the slope geometry and geologic structure (Evans et al., 2006).

In *sedimentary rocks*, sliding frequently takes place along persistent planar discontinuities such as bedding planes, faults, joint surfaces, or lithological contacts.

In *dip-slopes*, sliding takes place on bedding planes and it is frequently facilitated by the presence of bedding plane shears resulting from tectonic processes. Dip-slope sliding may be facilitated by buckling or by shear across bedding.

Initial failure in *steep underdip slopes* and *reverse slopes* in bedded rock sequences is complex and my involve buckling, toppling or break-out across bedding. The dip of key discontinuities may vary in a given dip slope and the sliding surface may thus be concave or convex. Planar or gently curved discontinuities are also important in determining a failure mode in strongly foliated metamorphic rocks.

In *rocks with a complex structure*, failure is controlled by impersistent but closely spaced discontinuities and may be complex, consisting of multiple wedges combined with local toppling.

Evans et al. (2006) emphasize the importance of massive rock slope failure characteristics like morphology, internal structure and sedimentology. First of all, they are essential in the initial identification of massive rock slope failure deposits. The literature is rich of examples of MRSF deposits that were initially interpreted as glacial deposits. Second, they are useful to understand the processes of fragmentation, transport and final consolidation as well as the mechanism of the interaction with the substrata that the debris travels over. Sedimentological studies of prehistoric MRSF deposits have also given important information about the precise sequence of initial failure and possible secondary processes. Furthermore, the knowledge of MRSF deposits and their internal structure is a key requirement in assessing the present stability of deposits that form landslide dams, either with respect to slope stability, piping, and resistance to overtopping.

2.3.1 Pre-failure Features and Triggers

The successful assessment of the hazards of MRSF depends on the recognition of pre-failure features: initial failure may be preceded by observable slope deformations (widening tension cracks, increased rockfall activity) and the time-to-failure calculations may be made on the rate of movement of specific targets placed on the moving slope. Monitoring is a common approach to hazard management. However, initial rock slope failure may occur without warning as a result of a sudden earthquake trigger. Seismically induced landslides can be divided into direct failures, which occur essentially synchronously with the shock, and indirect failures which occur subsequently, often by up to hours or days, as a result of induced groundwater or other changes. Other common triggers of landslides are heavy or prolonged rainfall or snow melt, toe erosion, impounding of lakes or reservoirs and rapid draw-down following emptying. Recently, melting of mountain permafrost, in the Alps for example, has led to the stimulation of debris flow activity and may influence deep-seated failures (Hutchinson, 2006).

Failures in brittle compound slides can present particular danger. Even if their bounding slip surfaces are pre-existing and non-brittle, failures on their internal shears are generally first-time and brittle and can impart a sudden acceleration to the overall failure. The most dramatic example of such a process is provided by the Vaiont slide of 1963. The morphology of landslides in downslope section determines whether their incipient movements are kinematically admissible or kinematically inadmissible; in the former case the slide can move without internal deformation of the sliding block, whereas in the latter case the potential slide block is virtually locked in position until transformed into a mechanism, and thus released, by the formation of internal shears. Three common examples, the kinematically admissible planar and circular slides and the kinematically inadmissible compound slides, are shown in Figure 2.1. Particularly important in a compound slide, is the internal shear (A) towards the rear of the slide, which results in the formation of a graben.

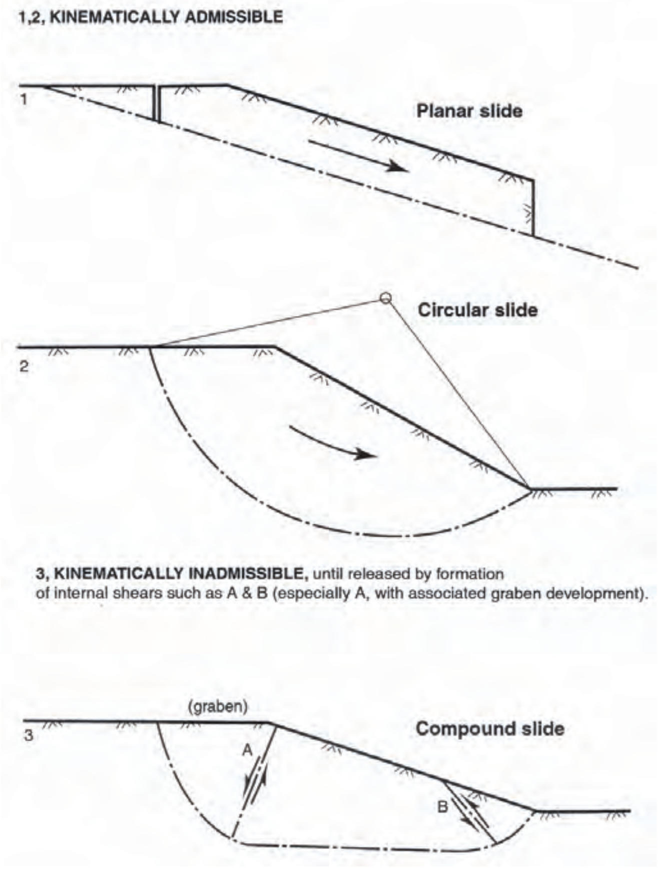

Figure 2.1: Kinematically admissible and inadmissible landslides (Hutchinson, 2006).

2.4 Deep-seated landslide from Massive Rock Slope Failure

The so called *"slow mountain slope deformation"*, classified by Evans et al. (2006) as a type of "landslide from massive rock slope failure", has been extensively studied by several scientists in the past decades.

The importance of slow mountain slope deformations, also called deep-seated landslides, is that they occur in many parts of the world, are considered to be a major geological hazard, and impact very significantly on infrastructures and on society. It is to be recognized that many aspects of deep-seated landslides are poorly understood and need be investigated in order to gain the necessary confidence for anticipating and predicting their behaviour, assess the risk, and find possible preventive/remedial measures. This is indeed due to the many complexities of the phenomena involved which encompass the understanding of the underlying mechanisms, the initial and post-failure behaviour, and the different secondary processes resulting from instability (Barla, 2010).

In the literature, large-scale slope deformations have been defined by authors in many different ways based on the study approach or the failure mechanism. Although this style of landslide has long been identified, the study of these deformations has been restricted to the identification of morphological aspects and description of movement rates. More problematic is to study the geomechanical behaviour, particularly because of the difficulty to investigate the rock at considerable depth. Independent of this, several authors carried out laboratory work to better understand the behaviour of rock along shear surfaces of deep-seated landslides.

In the next subsection an historical review as well as the main features of this type of landslide are presented.

2.4.1 Historical background

Many high mountain ridges are affected by large-scale deep-reaching gravitational deformations. They may attain lengths of several kilometres and heights even over 1000 m. This expressive geomorphological manifestations were observed long ago, but they were attributed to other factors, mainly to the action of snow, wind, regelation, etc. The opinion that they may be the manifestation of deep-reaching deformations of mountain slopes was supported mainly by the works of Ampferer (1939) and Stini (1941), who described merely phenomenological structures of such mass movements as "Bergzerreißung" (ridge top spreading) and "Talzuschub" (bulging toe).

The first definition of deep-reaching gravitational deformations has been given by Heim (1932), who referred to "sackung" as the slow, steep to vertical deformation of mountain slopes, wherein the internal structure is not changed considerably and displacement is concentrated on a distinct shear surface. In general "sacken" (to sag) means "a vertical movement".

The first hypotheses on the deformation mechanisms based on deep creep and tentative of explanations of the possible causes, appeared in the literature in the sixties. Terzaghi (1962) pointed to the danger of deep-seated rock slides for the construction of dams in deep mountain valleys. He stated that «practically nothing is known concerning the mechanics of deep seated, large-scale rock slides. It is not known whether the slides took place rapidly or slow by, and it is doubtful whether they are preceded by important creep deformation of the rocks located within the shear zone».

Ter-Stepanian (1966) also proposed the theory of deep creep of slopes and identified three main groups of creep deformations in rock masses: *planar*, *rotational* and *general* (Figure 2.2): mechanisms from a) to e) are examples of *planar* creep, f) and g) are examples of *circular* creep, h) and i) are examples of *general* creep. Experience accumulated shows that *rotational* creep deformations of rock slopes as defined by Ter-Stepanian (1966) take places in many cases. Such conditions were described by Zischinsky (1966) in the Alps.

On the basis of systematic investigations, Zischinsky (1966) pointed out that the existence of a basal sliding plane is not absolutely necessary for a mass movement in some type of rocks such as phyllite, micaschist, paragneiss and similar rock masses. Thus, large mass movements do not have to be slides and continuous creep of rock plays a particular role in such mass movements. Zischinsky (1966) suggested a Bingham body when modelling rock creep and in his work he showed only "low angle dipping displacement vectors" in the profile of the mass movements investigated. For unexplained reasons Zischinsky called such mass movement "sackung", though "low angle dipping displacement vectors" contradict the meaning of "sag" (vertical movement) introduced in literature by Heim (1932).

The term "sackung" was used by Zischinsky for a large-scale gravitational movement that takes place by gradual displacements along a series of disconnected planes or by plastic deformation of a rock mass without formation of a through-going slide plane. It may pass into or be combined with movement along a slide surface (Figure 2.3). He recommended that the term be applied to movements in which the amount of pervasively distributed deformation is large in relation to the displacement along a discrete surface of sliding.

Almost all profiles drawn by Zischinsky show normal faults in the upper slope area (Figure 2.3). Zischinsky argued that these movements are continuous in space, because these normal faults are small in relation to the deformed area on the whole. However, normal faults are not consequence of creep. Creep of a rock mass produces tensile stress above slope surface bends. This corresponds to the "Bergzerreißung" described by

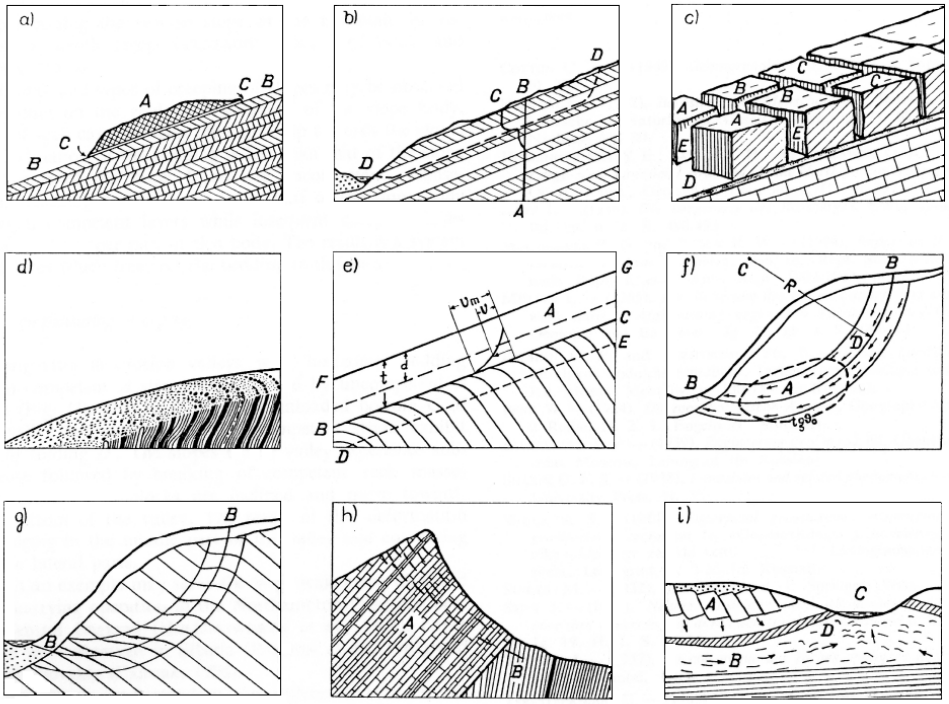

Figure 2.2: Rock creep typologies after Ter-Stepanian (1966); **a)** creeping of slabs; **b)** consequent creeping; **c)** creeping away of blocks; **d)** outcrop creeping; **e)** terminal creeping; **f)** asequent creeping; **g)** S-like creeping; **h)** insequent creeping; **i)** compensating creeping.

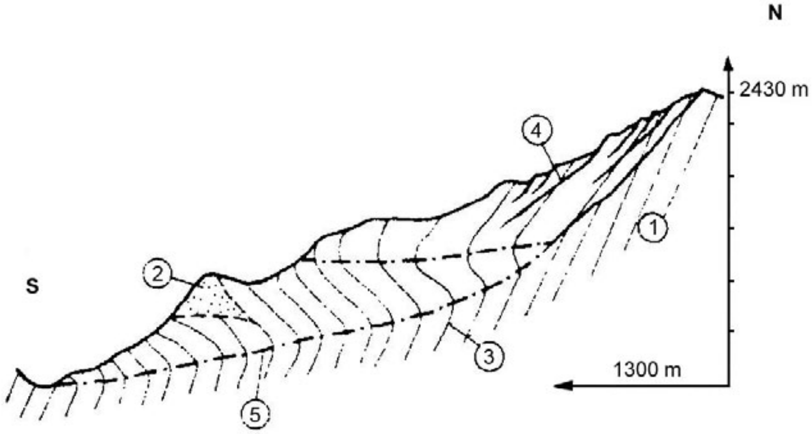

Figure 2.3: Typical profiles of "sackung" from Zischinsky (1966). Cross section of the Matrai-Glunzenberg slope: **1**-phyllite and paragneiss in original position; **2**-carbonates; **3**-indication of foliation planes; **4**-shear planes; **5**-probable depth of deformation.

Ampferer (1939). Thus a "Bergzerreißung" results from tensile stresses parallel to the surface above a slope surface bend, and is therefore a more or less vertical tensile crack. Normal faults like those drawn e.g. by Zischinsky in his profiles, do not result directly from creeping of rock masses in slopes and therefore are not a "Bergzerreißungen".

In a recent review lecture, Poisel and Kieffer (2010) try to demystify the ambiguity of the term "sackung", concluding that the mechanism called "sackung" by Zischinsky (1966) cannot be explained and modelled only by creep of rock masses and is an extremely complex process depending on a lot of parameters of rock.

In the classification of slope movements presented by Varnes (1958, 1978), the large-scale gravitational movement can be considered as a *flow type* of movement in rock, in which motion takes place by relative movement of particles within the moving mass, as contrasted with a slide-type movement, in which an entire mass moves relative to the stable underlying slope along a through-going surface of shear. This definition is similar to Zischinsky's definition of sackung.

Other authors refer to this style of deep reaching gravitational deformations in their research work. According to the Nemcok et al. (1972) classification, these deformations belong to the *creep* group; the proposed classification of mass movements divides them into four type of processes: *creep*, *sliding*, *flow,* and *fall.*

In this classification, *creep* is defined as a geologically long-term movement of non-increasing velocity without well-defined sliding surfaces. In most cases it can refer to deep-seated (or viscous) flow. Thus, the movements are designated as creeping movements, whereas the resulting phenomenon is rock creep, talus creep or soil creep. When an expressive acceleration is involved, the deformation passes from creep into one of the catastrophic forms (*sliding*, *flow* or *fall*). In solid rocks they are predominantly rockslides, but rockfalls are also frequent.

Nemcok et al. (1972) give a number of examples of *creep* (Figure 2.4): examples 1-8 are examples of deep-reaching creep, whereas example 9 is an example of superficial creep. Example 1 and 2 are loosening of the rocks in the valley slope by cracks parallel to the surface and initial disturbing of the stability of the slope by opening of tension cracks, typical of brittle materials. Example 3 and 4 are deep-seated creep, phenomenon previously described under the term of "Bergzerreißung" (crack in a mountain ridge) and "Talzuschub" (deformation at the toe of a slope), typical of brittle rocks. The type of deep-reaching creep is controlled in the first place by the geological structure of the slope.

In 1977 the Congress of the International Association of Engineering Geology held in Prague, devoted a session to "Deep-seated gravitational slope deformation" (DSGSD). Nemcok and Baliak (1977) briefly describe gravitational deformations in Mesozoic rocks of the West Carpathian mountain ranges. These areas are affected by slope movements of all the four principal groups according to the Nemcok et al. (1972) classification. Most frequently the creep slope deformations are accompanied by disintegration of mountain ridges. An example of such deformations is the deformation on Sivy mountain. The marked difference in behaviour was found between the southern steep slope of the Sivy mountain ridge which does not display any movement, and the northern gentler slope which is dissected by cracks, furrows and down throws into a system of blocks moving toward the valley (Figure 2.5).

In Italy, a study group on deep-seated gravitational slope deformations was set up in the eighties and included more than 80 researchers.

Hutchinson (1988) classified mass movements according to their morphology, mechanism, type of rock and movement velocity. He introduced in the class *creep*, the type *deep-seated continuous creep* or *mass creep*, as considered by Zischinsky (1966); then he used the term "sagging" of mountain slope in a considerably wider sense than the Zischinsky's original "sackungen".

Hutchinson (1988) therefore instigated many misunderstandings and imprecisions by allocating one type of mass movement to two classes (Poisel and Kieffer, 2010).

Sorriso-Valvo and Dramis (1994) contributed to investigate large-scale gravitational movements. They described the DSGSDs as a group of mass movement phenomena

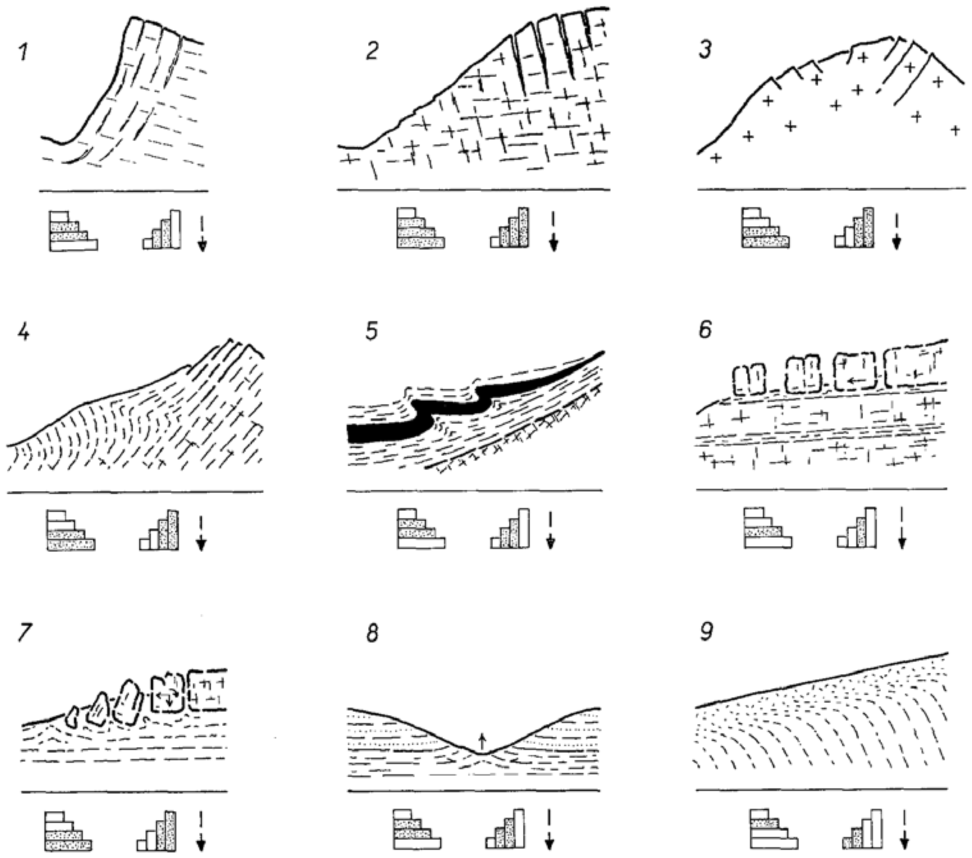

Figure 2.4: Examples of *creep* types from Nemcok et al. (1972).

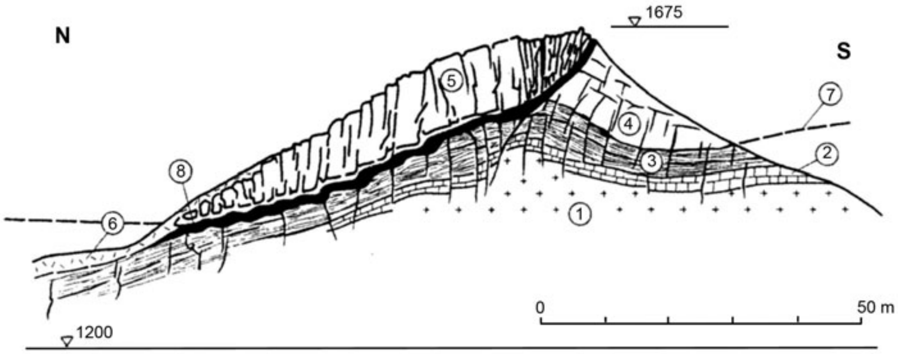

Figure 2.5: Cross section through the ridge of Sivy mountain (Nemcok and Baliak, 1977). **1**-biotitic quartz diorites and granodiorites (Paleozoic); **2**-limestones, dolomites, coloured shales, dolomite intercalations and quartzites of the Carpathian Keuperian (Triassic); **3**-shales and sandstones, marly limestones and shales (Jurassic - Neocomian); **4**-dolomites and limestones (Triassic Choc nappe); **5**-block in the Triassic limestones and dolomites; **6**-trenches, step-like scarps; **7**-thrust faults; **8**-shear zone.

characterised by the following elements:

(a) The deforming mass may or may not be bounded by a continuous yielding surface; however, the continuity of such surface is not indispensable to explain the superficial deformations.

(b) The volume of masses involved is of the order of several hundred thousands of cubic meters or more, the thickness is several tens of meters or more.

(c) Scale factors may influence the mechanical properties of the rock and, consequently, the deformation mechanism.

(d) The total displacement is small in comparison to the magnitude of the mass involved.

With the above conditions some phenomena cannot be classified precisely, as often happens with classifications of most natural phenomena. Three basic types of DSGSD were defined as follows:

(1) Sackung (Zischinsky, 1966), or the rock-flow type in Varnes (1958, 1978).

(2) Lateral spread of ridges (Varnes, 1978 and Hutchinson, 1988).

(3) Lateral spread of thrust fronts (may correspond to the complex types in Varnes (1978)).

According to the above points (a) to (d), the types 1 and 3 of the DSGSD basic type correspond to deep-seated, pre-failure creep and to the different types of sagging in Hutchinson (1988).

In 2002, declared by the United Nations, the "Year of the Mountains", a NATO Advanced Research Workshop, known as "Celano Workshop", was purposely organized to bring together scientists involved in a range of research topics related to massive rock slope failure. The idea was to attempt a critical assessment of the state-of-the-art concerning catastrophic massive rock slope failure. In that workshop, Evans et al. (2006) identify the large-scale deep-reaching gravitational deformations as a type of *landslide from massive rock slope failure*, called by the authors "slow mountain slope deformation", as already described in Section 2.2.

2.4.2 Morphological, geomechanical and structural features of deep-seated landslides

Deep-seated landslides from massive rock slope failure are slow to extremely slow moving massive natural slopes characterized by a failure deformation which occurs at great depth in excess of 100 m and up to 250-300 m (Barla, 2010). They occur on high relief energy hill-slopes, with size comparable to the whole slope, and with displacements relatively small in comparison to the slope itself. In cases such deformation takes place along a basal sliding surface which is described as a zone of sheared and cataclastic rock, locally reduced to a soil-like material with silt and clay. They are most often associated with rocks which exhibit marked strength anisotropy such as shale, schist, gneiss, micaschist, slate etc., but the phenomenon is also associated with igneous (plutonic) rocks such as granite and diorite, volcanic rocks (Tabor, 1971). They are less usual in sedimentary rocks, also if some authors have been observed such phenomenon in massive sedimentary rocks (Beck, 1968; Radbruch-Hall (1978)).

The typical morphological and structural features of deep-seated landslides are impressive mainly in the *crest part*. The exposures of shear planes on the surface are manifest as rock steps and furrows running parallel to the crest. Small lakes and double crests form on the ridges and linear fissures often occur behind the shear plane scars (Mahr and Nemcok, 1977).

In the *upper* and *middle parts* of the slope, mainly in rocks of higher mechanical strength (i.e. granitoids, orthogneiss), there are uphill-facing (antislope) scarps. Rock steps and uphill-facing scarps on the crests sometimes create forms similar to graben, 50-100 m wide, 6-50 m deep and several hundred meters long (Radbruch-Hall et al., 1976). The authors are of the opinion that the existence of a graben implies that the top of the ridge dropped down as the south-west-facing sloped bulged out (Figure 2.6). As the movement proceeded, reverse slippage took place along the major joint system. The rock below the plane of slippage moved upward relative to the one above it, forming uphill-facing scarps on the mountain side.

If the rock is weaker, such as low-grade metamorphic rock or crushed gneiss, deformation is ductile and the geomorphological manifestations like trenches may not develop. In more plastically deforming rocks the deformation in the central part of the slope appears as rippling of the slope, and the strikes and dips of foliation or bedding planes scatter enormously. In some cases arching up has been observed in the central and lower parts of the slope (Mahr, 1977).

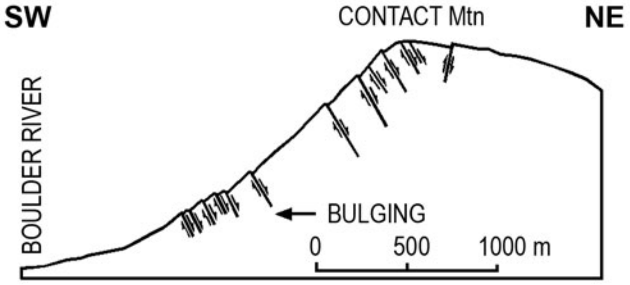

Figure 2.6: Cross section of Contact Mountain, Montana, according to Radbruch-Hall et al. (1976).

The morphological manifestations are less marked at the *foot* of the slope. Rocks extending into the valley quickly disintegrate and are transported by strongly eroding water courses flowing in mountain valleys. At other places they are overlapped by accumulation forms or by fluvial and glaciofluvial deposits. An example of such an overlap is cited by Desio (1973). During the construction of the Beauregard arch dam it was found that the bottom of the valley is overlapped by sediments more than 40 m thick (Figure 2.7).

Two opposing hypotheses have been proposed for the *subsurface geometry* of a sackung in massive competent rocks (McCalpin and Irvine, 1995). The first hypothesis is due to Zischinsky (1969) and Mahr (1977) who state that in such cases «a well defined

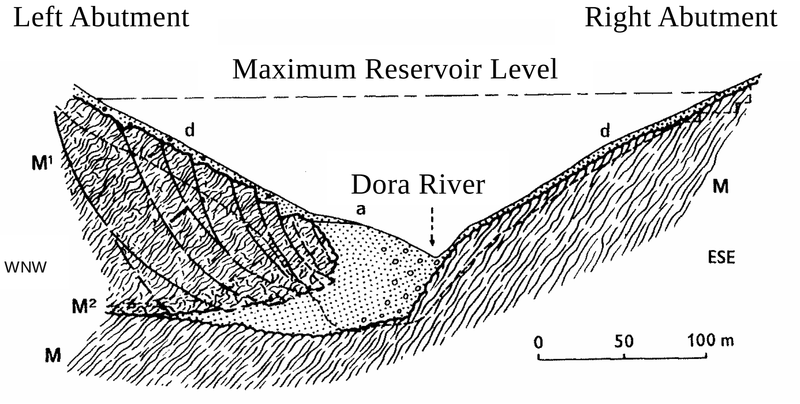

Figure 2.7: Geological cross section at the Beauregard dam site showing the accumulation of fluvial and glaciofluvial deposits (Desio, 1973). **M**, compact mica schists; $\mathbf{M^1}$, fractured and mylonitic mica schists; $\mathbf{M^2}$, mica schists as $\mathbf{M^1}$ but very disjointed; **a**, fine and coarse alluvial deposits; **d**, debris; glacial deposits. Foundations excavations in dashed line.

slide plane near the headscarp passes downward into a broader zone of rock creep. Consequently the lower portion of this type of failure simply bulges out into the valley». Such slow failure mechanism results into well developed tensional features near the head, but often without evidence of typical landslide features in the central part of the slope and at the toe. The second hypothesis is that sackung is a shallow surface manifestation of toppling and flexural slip along discontinuities that dip steeply into a mountain mass (Jahn, 1964; Beck, 1968; and Bovis, 1982). This was termed by Bovis as "flexural toppling", in which outward rotation blocks and dilation of sackung cracks lead to attenuation of movement with time, which Bovis (1982) compared to strain-hardening in granular material.

Agliardi et al. (2001) used the term "morpho-structure" to describe the morphological expression of a deformational structure of tectonic or gravitative origin. The morpho-structures have been described and mapped in the past prevalently with a morphological approach. Terms as "scarp", "up-hill facing scarp" or "antislope scarps" introduced by Radbruch-Hall et al. (1976), have been used to point out an upward or downward facing break in the slope profile with different origins.

Hutchinson (1988) distinguished three main types of feature:

- DD (normal down-slope down-movement facing scarps);
- UD (up-slope down-movement facing counterscarp);
- UU (up-slope up-movement facing counterscarp);

but again no complete information is given about the kinematics. In fact, Hutchinson (1988) in his work on classifications, state that «movement is used in the sense of the overall, eventual slide movement, not a local movement associated with scarp formation». All these different approaches caused some misunderstanding in the kinematic interpretation of the DSGSD structures, so that Agliardi et al. (2001) gave kinematically consistent nomenclature in order to minimize ambiguities. According to them, the following terms have been adopted (Figure 2.8):

- **Scarp**: morphological expression of a down-hill dipping collapse or main failure surface with a down-slope movement;
- **Counterscarp**: surface evidence of an upward dipping surface, standing alone or antithetically associated to a major scarp with an up-slope movement;
- **Trench**: linear and deeply cut form, expression of extensional opening of a vertical or downward dipping surface.

2.4.3 Failure mechanisms and structural evolution

McCalpin and Irvine (1995) state that the stress field that produces a sackung may have five possible origins:

a) Ice wedging (Zischinsky, 1969).

b) Gravity forces that produce slow deformation in a rock mass.

c) Stored forces resulting from prior loading conditions (e.g. glaciation).

d) Seismic shacking.

e) Displacement connected to deep-seated seismogenic faults.

Almost all researchers agree that *tectonics* is one of the relevant factors for the development of mass-movement, especially when large-scale landslides, sackung and lateral spreads are concerned. In most of the cases studied in the literature, it is evident that the subsequent development of these type of movements may be determined in large

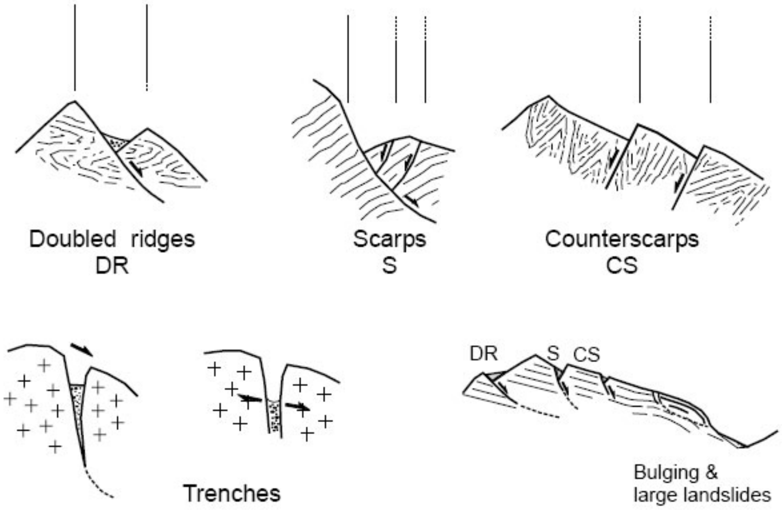

Figure 2.8: Morpho-structural features typical of a DSGSD (Agliardi et al., 2001).

part by geomorphologic evolution. Sorriso-Valvo and Dramis (1994) observe a possible relationship that exists between some type of mass movement and tectonics. They state that it is possible to recognize the following conditions:

(A) Sackung evolving progressively towards rock slide and debris avalanche, for nearly homogeneous, low to high grade metamorphic, igneous, densely jointed rocks, on high fault scarps and on steep slopes of recently deglaciated areas.

(B) Lateral spread with sliding components, for crystalline and sedimentary rocks, hard and jointed, and decompressed by the relief of tectonic stress because erosion, or by the relief of glacial pressure;

(C) Opening of tension crack due to gravitation-driven movement, for layered rocks most frequently sedimentary, with alternating layers of different competence, folded and thrusted; or in case of thrusting and anticlinal folding, lateral spreading, evolving progressively towards rock sliding or debris avalanche.

As far as the sackung deformation is concerned, some researchers propose different models to explain the *mechanism of failure*. As previously described, sackung consists of creeping-flow type deformation in hard, jointed rock forming high steep slopes, whereas if the rock is hard and little jointed (as in a granite or massive sandstone), it probably deforms through micro-fracturing (Sorriso-Valvo and Dramis, 1994).

Some researchers accept the model by *Mencl (1968)*. They say that morphological forms found on the creep deformation in the slope correspond well to the theoretical considerations based on the assumption of contractant dilatation behaviour of the rock in deformation (Mahr, 1977). The problem of dilatancy and contractancy was analysed by Mencl. He proposed a simple model of contractant and dilatant rock mass and he proved that dilatant masses which in shear disturbance increase their volume deform along a "thin" shear plane and, contractant rocks which in shear disturbance decrease their volume deform in a "thick" zone. In slope movement it happens that the rock behaves differently under different loading; by compressing the contractant zone, considerable deformations take place in the central part of the slope. In the upper and lower parts when the stresses are smaller, the rock behaves dilatantly and sharp shear planes develop. An example based on Mencl's work is given in Figure 2.9.

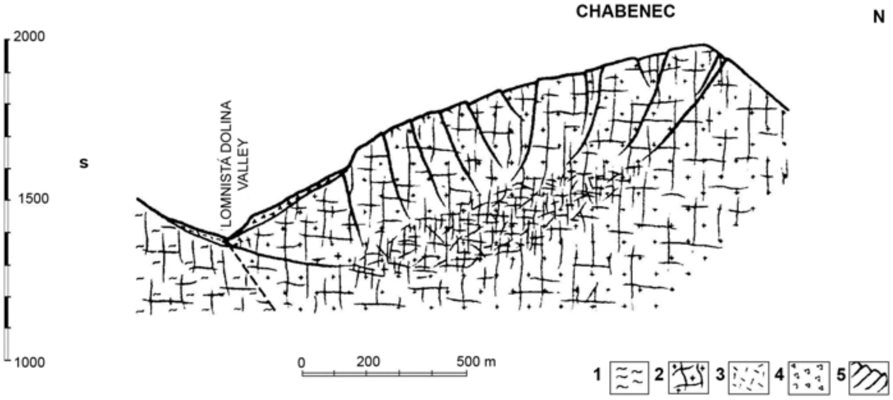

Figure 2.9: Cross section of the Chabenec Southern slope: **1**-orthogneiss; **2**-biotite quartz diorite to granodiorites with joints; **3**-slope debris; **4**-accumulation of rock slide; **5**-dilatant shear planes (from Mahr, 1977).

Inside a sufficiently high slopes, where the limit of pressures between the contractant and dilatant behaviour of the rock is exceeded, a thick crushed and compressed contractant zone forms. At the slope foot and on the crest of the slope shear planes form as a result of the dilatant behaviour of little loaded rock or of a deformation of considerable extent of the contractant zone.

A scheme of progressive slope deformation on the example of Chabenec in the Low Tatras mountain range was proposed by Feda (1973) (Figure 2.10). Since the slope failed locally, but the total stability was not surpassed, it implies a progressive failure. He states that decisive for the failure progression will be the mechanical behaviour of the rock mass; this can be either brittle (dilatant) or ductile (contractant). Feda's hypothesis of the development of slope deformation is based on theoretical considerations and on the field observation. First tension cracks originate at the slope crests, then sliding surfaces at the slope toe, later sliding surface near the slope crests originate and the failure spreads toward the slope centre. After contractant failure has occurred, the volume of the middle part of the slope decreases. Secondary shear planes develop, because the rock behaviour at the surface is again brittle (Mahr, 1977). On the basis of the above mentioned mechanism of failure, deep-reaching gravitational slope deformations of mountains, can be classified into the group of *rotational depth creep*, according to Ter-Stepanian's classification.

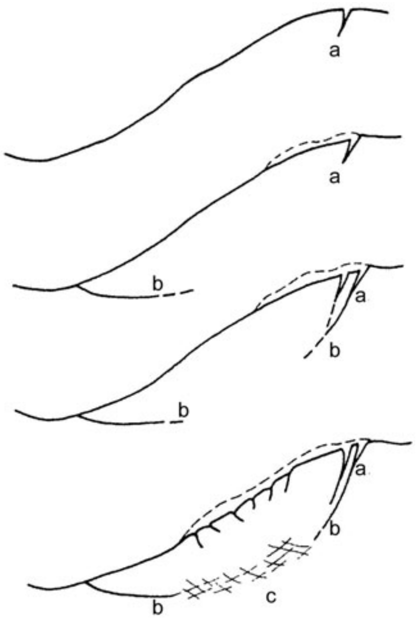

Figure 2.10: Development of slope failure according to Feda (1973): **a)** tension cracks; **b)** shear planes; **c)** shear zone with ductile behaviour (from Mahr, 1977).

Savage and Varnes (1987) introduced a model for sackung that implies a plastic *flow solution* with a continuous basal shearing surface. This could be referred to the final stage of evolution of a deep-seated landslide, when all the rock mass is on the verge of a catastrophic failure. In addiction, the assumption that the slope material has the same characteristics at every point within the interior of the slope cannot be accepted because of the large volumes involved. Even though the material is uniform, the high confining pressure at depth, combined with dense jointing, is supposed to be able to induce brittle-ductile transition in the material, so that the model of Mencl could be justified (Sorriso-Valvo and Dramis (1994)).

Both models explain the presence of scarps in the highest and lowest parts of the slope, but the movement along mid-slope shearing surfaces is reversed (Figure 2.11).

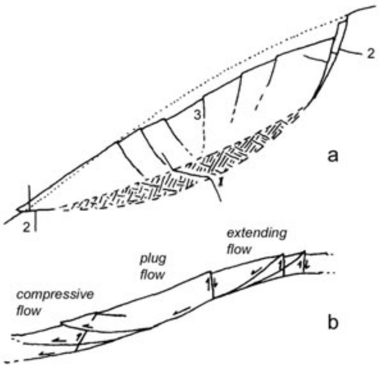

Figure 2.11: Deformation occurring in a sackung according to the distributed shear model (a) and the plastic failure model (b), (from Sorriso-Valvo and Dramis, 1994). **1**-zone of viscous deformation, with contractant material; **2**-shearing on discrete surface; **3**-shearing in the brittle (shallow) zone to accommodate the volume decrease in ductile (deep) zone.

As the creeping deformation continues, it can change into an accelerated phase that leads to the catastrophic collapse of large-scale rock avalanches. In this manner, some authors consider sackung as the initial stage of a rock avalanche, whereas others prefer to keep sackung as a separate type, because it is peculiar in terms of affected rock and slope morphology (Sorriso-Valvo and Dramis, 1994). With respect to the evolution of a deep-seated landslide it is important to determine if the relief of the slope is increasing by for example observing the activity of the fault that originate the scarp.

Petley and Allison (1997) investigate the mechanical behaviour of deep-seated landslides. In their laboratory study they try to simulate the stress-strain environment at the bottom of these type of particularly large mass movements. They state that deep-seated landslides mechanism of failure is a consequence of three deformation modes. At the lowest stresses the material have a brittle behaviour, leading to catastrophic movement as a result of the development of a shear surface. At depth, some materials have a purely ductile behaviour, leading to continuous, creep-like movement. The experimental study carried out on mudrocks sample, suggests that some materials also show a combination of ductile and brittle deformation, inducing long periods of creep followed by abrupt brittle failure.

2.4.4 Types of movements characterising deep-seated massive landslides

In young orogenic areas, the most hazardous and destructive types of slope deformation, such as rockfalls, rock avalanches, debris flows, rockslides and shallow translational and rotational landslides, are often predisposed by older deep-seated gravitational slope deformations (Dikau et al., 1996).

The study presented by Hradecky and Panek (2008) demonstrates the link between DSGSDs and the occurrence of landslide hazards in the highest part of the Flysch Carpathians within the territory of the Czech Republic. The working hypothesis of the study assumes that a long-term development of deep-seated slope deformations (in the order of thousands of years) creates suitable conditions for the subsequent occurrence of a wide range of other slope deformations. The hypothesis verification has been demonstrated on case studies with a varied link between DSGSDs and consequent mass movements.

DSGSDs disrupt bedrock, generate discontinuities and change slope morphology resulting in superficial reactivations. Generally, this activation concerns a relatively small part of the volume of a DSGSD, but it tends to have highly destructive consequences (Deng et al., 2000). Areas affected by DSGSDs are characterized by the existence of morphologically unstable segments of slopes, such as old steep landslide scarps and forefront parts of rotated and gravitationally subsided blocks.

Gravitational disequilibrium of mountain ridges in the uppermost part of the Flysch Carpathians, in the territory of the Czech Republic, is related to the vertical contact of nappe structures of contrasting mechanic characteristics. Mountain ridges are formed by rigid sandstone complexes (the Godula Nappe) thrust over mainly plastic incompetent claystones and thinly bedded sandstones (the Tesin Nappe). In such a way the density of slope failure is thus most often associated with two types of geological structures (Figure 2.12).

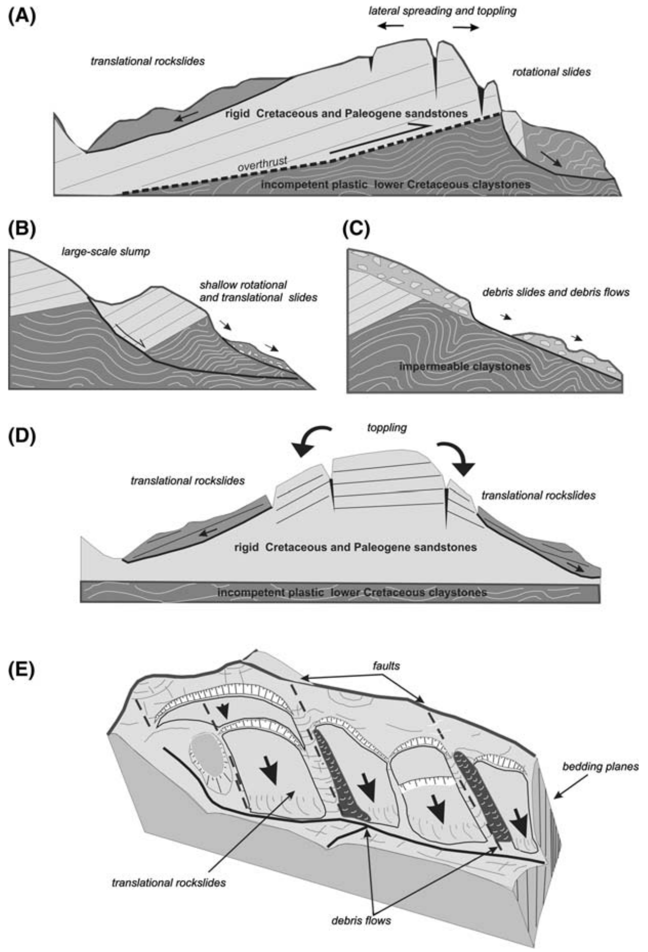

Figure 2.12: Scheme of gravitational disequilibrium in the culmination part of the flysch Carpathians (Hradecky and Panek, 2008). **(A)** Genesis of a DSGSD in the forefront part of the Godula Nappe connected with denuded contact of overlying rigid layers with underlying plastic formations, typical development of translational landslides on bedding planes features the back part of the nappe. **(B)** Large scale rotational landslides on the contact of Godula and Tesin Nappes initiate the development of presently active shallow translational and rotational landslides in their forefront parts. **(C)** Development of shallow translational landslides and debris flows is located on the contact of pervious sandstone debris generated from higher situated outcrops and underlying impervious claystones. **(D)** Toppling initiate tilting of bedding planes comformingly with the slope inclination, which causes the development of rockslides and rock avalanches. **(E)** Development of translational rockslides on bedding planes of flysch formations is aligned by transversal tectonic lines which predispose scarps of landslides and the direction of debris flows.

The study of active landslide areas within the studied territory of the Flysch Carpathians proved that the key causative factor for the development of young (particularly shallow) landslides is the presence of DSGSDs (Baron et al., 2004). With some exceptions, young active landslides developed and are still formed in zones of DSGSDs, which has been described even in other young orogenic parts of the Earth (e.g. Bisci et al. (1996)).

A geomorphic analysis of key localities and a preliminary study of other slope deformations in the area of the highest mountain groups of the Czech part of the Carpathians proved that the causes of landslide hazards are conditioned by the functioning of three factors:

- structural causes;
- the intensity of incision of the valley bottom;
- Quaternary landscape development, including climatic oscillations and increasing human activities during the course of the given historic periods.

The structure is a determinative factor of the widespread extension and volume of slope deformations (Margielewski and Urban, 2003). The first level of preparatory factors consists in the tectonic break-up of the autochton of flysch nappes. Moreover, the reactivated tectonic failures of the Paleozoic fundament of nappes had a crucial influence. At present, many extensional structures and evidence of gravitational disintegration on the highest ridges of the area are related to the development of the inherited Paleozoic failures. The second level of preparatory factors is caused by the compression movement of nappes and pressure on clastic Miocene sediments. The third level of preparatory factors is caused by the actual lithological and tectonic structure of flysch nappes. In terms of slope instabilities, they have a suitable monoclinal structure and gravitationally unstable distribution of complexes of layers, as soft and incompetent layers occur in stratigraphically lower levels while higher structural levels are formed by rigid competent formations. These preparatory factors have led to a state in which practically all parts of the range have an exposed position with respect to the occurrence of deep-seated slope deformations and their subsequent shallow accelerations.

The primary preparatory factors mentioned above would not lead to the creation of slope instabilities without vertical dissection and denudation. The preliminary analysis of several hundred slope deformations within the studied area, showed that an incised valley is essential for the development of large-scale landslides, but what appears to be much more important, is the valley incision below the boundary between rigid overlying and underlying plastic layers. In this context, during recent decades, most streams in the area underwent anthropogenic accelerated change from an accumulation into an erosion regime. This effect leads to active vertical erosion which further deepens mountain valleys and shifts the position of valley bottoms below the boundary between rigid and plastic layers. This change can lead to the development or acceleration of the collapse in areas where slope deformations are still in the initial succession stage.

2.5 Summary

This chapter attempts to describe the complexities related to landslides resulting from massive rock slope failure. Hazard assessment of massive rock slope failure is made difficult by a variety of complex initial failure processes and unpredictable post-failure behaviour, which includes transformation of movement mechanism, substantial changes in volume by deposition and/or entrainment, and changes in the characteristics of the moving mass. Initial failure mechanisms are strongly influenced by geology and topography, and, because of this, the development of geological models is essential for the analysis of these mechanisms.

In the second part of the chapter, deep-seated landslides from massive rock slope failure are illustrated. Generally, in the scientific literature the understanding of such a phenomena is not uniform. Large-scale slope deformations have been defined by authors in many different ways based on the study approach or the failure mechanism. Although these landslides have long been identified, their study has been restricted to the identification of morphological aspects and description of movement rates. A sufficient understanding of massive landslides and the hazards connected with them require a multidisciplinary approach using geological, geomorphological, geophysical technologies. Also monitoring of deep-seated landslides is a common approach to hazard management. The study presented in the last section of the chapter is an example of comprehensive study in order to acquire a thorough knowledge of the causes, mechanism and history of large-scale slope deformations. The emphasis is on the types of slope deformations which are often linked with older deep-seated gravitational slope deformations.

References

Agliardi, F., Crosta, G., and Zanchi, A. (**2001**). "Structural constraints on deep-seated slope deformation kinematics." *Engineering Geology*, 59: 83–102.

Ampferer, O. (**1939**). "Über einige Formen von Bergzerreißung." *Sitzungsberichte der Akademie der Wissenschaften Wien*, 148: 1–14.

Barla, G. (**2010**). "Progress in the understanding of deep-seated landslides from massiver rock slope failure." In "ISRM International Symposium and 6th Asian Rock Mechanics Symposium, 23-27 October 2010, New Delhi, India," .

Baron, I., Cilek, V., Krejci, O., Melichar, R., and Hubatka, F. (**2004**). "Structure and dynamics of deep-seated slope failures in the Magura Flysch Nappe, outer Western Carpathians (Czech Republic)." *Natural Hazards and Earth System Sciences*, 4: 549–562.

Beck, A. (**1968**). "Gravity faulting as a mechanism of topographic adjustment." *New Zealand Journal of Geology and Geophysics*, 11: 191–199.

Bisci, C., Burattini, F., Dramis, F., Leoperdi, S., Pontoni, F., and Pontoni, F. (**1996**). "The Sant' Agata Feltria landslide (Marche Region, central Italy): a case of recurrent earthflow evolving from a deep-seated gravitational slope deformation." *Geomorphology*, 15: 351–361.

Bovis, M. J. (**1982**). "Uphill-facing (antislope) scarps in the Coast Mountains, Southwest British Columbia." *Geological Society of America Bulletin*, 93: 804–812.

Cruden, D. and Varnes, D. (**1996**). *Landslides: Investigation and Mitigation*, chapter 3 - landslide types and processes, pages 36–75. National Academy Press, Washington, D.C.

Deng, Q., Zhu, Z., Cui, Z., and Wang, X. (**2000**). "Mass rock creep and landsliding on the Huangtupo slope in the reservoir area of the Three Gorges Project, Yangtze River, China." *Engineering Geology*, 58: 67–83.

Desio, A. (**1973**). *Geologia applicata alla Ingegneria*. Hoepli.

Dikau, R., Brunsden, D., Schrott, L., and Ibsen, M. (**1996**). *Landslide recognition: identification, movement and causes*. Wiley, Chichester.

Evans, S. (**2006**). "Single-event landslides resulting from massive rock slope failure: characterising their frequency and impact on society." In S. G. Evans, G. Scarascia Mugnozza, A. L. Strom, and R. L. Hermanns, editors, "Landslides from Massive Rock Slope Failure," volume 49 of *NATO Science Series: IV: Earth and Environmental Sciences*, pages 53–73. Springer Netherlands.

Evans, S., Scarascia Mugnozza, G., Strom, A., Hermanns, R., Ischuk, A., and Vinnichenko, S. (**2006**). "Landslides from massive rock slope failure and associated phenomena." In S. G. Evans, G. Scarascia Mugnozza, A. L. Strom, and R. L. Hermanns, editors, "Landslides from Massive Rock Slope Failure," volume 49 of *NATO Science Series: IV: Earth and Environmental Sciences*, pages 03–52. Springer Netherlands.

Feda, J. (**1973**). "Stability of natural slopes." In "Proceedings of th 8th International Conference on Soil Mechanics and Foundation Engineering (Moscow). Oral discussion.", Session 6.

Heim, A. (**1932**). *Bergsturz und Menschelenben (Landslide and Human Lives)*. BiTech Publishers, Vancouver (1989).

Hoek, E. and Bray, J. (**1977**). *Rock slope engineering. Revised 2nd Edition.* Institution of Mining and Metallurgy, London.

Hradecky, J. and Panek, T. (**2008**). "Deep-seated gravitational slope deformations and their influence on consequent mass movements (case studies from the highest part of the Czech Carpathians)." *Natural Hazards*, 45: 235–253.

Hungr, O., Evans, S. G., Bovis, M. J., and Hutchinson, J. N. (**2001**). "A review of the classification of landslides of the flow type." *Environmental Engineering Geoscience*, 7(3): 221–238.

Hutchinson, J. (**1988**). "General Report. Morphological and geotechnical parameters of landslides in relation to geology and hydrogeology." In "Proceedings of th 5th International Symposium on Landslides, Lausanne, Switzweland," volume 1, pages 3–35. Balkema.

Hutchinson, J. (**2006**). "Massive Rock Slope Failure. Perspectives and retrospectives on the state-of-the-art." In S. G. Evans, G. Scarascia Mugnozza, A. L. Strom, and R. L. Hermanns, editors, "Landslides from Massive Rock Slope Failure," volume 49 of *NATO Science Series: IV: Earth and Environmental Sciences*, pages 619–662. Springer Netherlands.

Jahn, A. (**1964**). "Slopes morphological features resulting from gravitation." *Zeitschrift fur Geomorphologie*, Supplementband 5: 59–72.

Mahr, T. (**1977**). "Deep-reaching gravitational deformations of high mountain slopes." *Engineering Geology*, 16: 121–127.

Mahr, T. and Nemcok, A. (**1977**). "Deep-seated creep deformations in the crystalline cores of the Tatry Mts." *IAEG Bulletin*, 16: 104–106.

Margielewski, W. and Urban, J. (**2003**). "Crevice-type caves as initial forms of rock landslide development in the Flysch Carpathians." *Geomorphology*, 54: 325–338.

McCalpin, J. and Irvine, J. (**1995**). "Sackungen at Aspen Highlands Ski Area, Pitkin County, Colorado." In "Environmental and Engineering Geoscience," volume 1, pages 277–290.

Mencl, V. (**1968**). "Plastizitatslebre und das wirkliche Vethalten von Gehirgsmassen." *Felsmech. und Ing. Geologic.*, Suppl. IV: 1–8.

Nemcok, A. and Baliak, F. (**1977**). "Gravitational deformations in Mesozoic rocks of the Carpathian mountain ranges." *Engineering Geology*, 16: 109–111.

Nemcok, A., Pasek, J., and Rybar, J. (**1972**). "Classification of Landslides and Other Mass Movements." *Rock Mechanics*, 4: 71–78.

Nichol, S., Hungr, O., and Evans, S. G. (**2002**). "Large scale brittle and ductile toppling of rock slopes." *Canadian Geotechnical Journal*, 39: 773–788.

Petley, D. N. and Allison, R. J. (**1997**). "The mechanics of deep-seated landslides." *Earth Surface Processes and Landforms*, 22(8): 747–758.

Poisel, R. and Kieffer, S. (**2010**). "The Problem with Sackung." In "5th Colloquium Rock Mechanics - Theory and Practice," pages 53–66.

Radbruch-Hall, D. (**1978**). "Gravitational creep of rock masses on slopes." In B. Voight, editor, "Rockslides and Avalanches: Natural Phenomena (Developments in Geotechnical Engineering)," volume 1, chapter 17, pages 607–658. Elsevier, Amsterdam.

Radbruch-Hall, D., Varnes, D., and Savage, W. (**1976**). "Gravitational spreading of deep-seated ridges ("sackung") in Western United States." *Engineering Geology*, 14: 23–35.

Savage, W. and Varnes, D. (**1987**). "Mechanics of gravitational spreading of steep-sided ridges ("sackung")." *Bulletin of Engineering Geology and the Environment*, 35: 31–36.

Sorriso-Valvo, M. and Dramis, F. (**1994**). "Deep-seated gravitational slope deformations, related landslides and tectonics." *Engineering Geology*, 38: 231–243.

Stini, J. (**1941**). "Unsere Täler wachsen zu." *Geologie und Bauwesen*, 13: 71–79.

Tabor, R. (**1971**). "Origin of ridge top depressions by large-scale creep in the Olympic Mountains, Washington." *Geological Society of America Bulletin*, 82: 1811–1822.

Ter-Stepanian, G. (**1966**). "Types of depth creep of slopes in rock masses." In "Proceedings of 1st Congress of the International Society of Rock Mechanics, Lisbon," .

Terzaghi, K. (**1962**). "Stability of steep slopes on hard underweathered rock." *Géothechnique*, 12: 251–270.

Varnes, D. (**1958**). "Landslides types and processes." In E. Eckel, editor, "Landslides and engineering practice, Highway Research Board," Special Report 29, pages 20–47. NAS-NRC Pubblication 544, Washington, D.C.

Varnes, D. (**1978**). "Slope movement, types and processes." In R. L. Schuster and R. J. Krizek, editors, "Landslides: Analysis and Control," volume 176, pages 11–35. National Academy of Science. Washington, DC.

Varnes, D., Hall-Radbruch, D., and Savage, W. (**1989**). "Topographic and structural conditions in areas of gravitational spreading of ridges in the Western United States." *United States Geological Survey*, 1496: 1–28.

Zischinsky, U. (**1966**). "On the deformation of high slope." In "Proceedings of 1st Congress of the International Society of Rock Mechanics, Lisbon," volume 2, pages 179–185.

Zischinsky, U. (**1969**). "Uber sackungen." *Rock Mechanics*, 1: 30–52.

Chapter 3

Numerical modelling of landslides from massive rock slope failure

3.1 Introduction

Rock slope stability analyses are routinely performed in order to assess the safe and functional design of excavated slopes and the equilibrium conditions of natural slopes. The method chosen depends on both site conditions and the potential mode of failure, with careful consideration being given to the varying strengths, weaknesses and limitations inherent in each technique. This chapter presents the approach proposed by several authors to investigate failure mechanisms of rock slopes.

In accordance with this approach, analyses may be undertaken using different levels of sophistications. In this context, a review of numerical techniques used in rock slope stability analysis is done, with emphasis on the use of combined continuum-discontinuum numerical modelling codes as a powerful tool to model landslides from massive rock slope failure.

It should be emphasized that the use of such codes which involve fracture mechanics theory in rock slope analysis is still very much at the research stage. It is essential that these codes be constrained through analyses in which they are used in conjunction with conventional continuum and discontinuum approaches in order to establish an experience database for varied failure mechanisms. The application of these techniques to study the total slope failure of a massive rock slope will be a step forward.

3.2 The study of rock slope instability

In rock engineering design there are no simple universal rules for acceptability nor are there standard factors of safety which can be used to guarantee that a rock structure will be safe and it will perform adequately (Hoek, 1991). To demonstrate this, Hoek (1991) summarizes some of the typical problems, critical parameters, analysis methods and acceptability criteria which apply to a number of different rock engineering structures. The table relating to slope stability analysis is shown in Figure 3.1.

In general, the primary objectives of rock slope stability analyses are (Eberhardt, 2003):

- to determine the rock slope stability conditions;
- to investigate the potential failure mechanisms;
- to determine the slopes susceptibility to different triggering mechanisms;
- to test and compare different support and stabilization options;
- to design optimal excavated slopes in terms of safety, reliability and economics.

A site investigation study should precede any stability study and includes elements of geological and discontinuity mapping to provide the necessary input data for the stability analysis. The collection of data ideally involves rock mass characterization and the sampling of rock materials and discontinuities for laboratory analysis (i.e. strength and constitutive behaviour determination), field observations and in situ measurements. In situ monitoring of spatial and temporal variations in pore pressures, slope displacements, stresses and subsurface rock mass deformations, provide valuable data for constraining and validating the stability analysis undertaken.

In order to properly conduct such investigations, and to analyse and evaluate the potential hazard relating to an unstable rock slope, it is essential to understand the processes and mechanisms driving the instability. Landslide movements, as described in the previous chapter, may be considered as falls, topples, slides, spreads or flows (Cruden and Varnes, 1996a), and in some cases involve different combinations of several failure modes (referred to as composite slides). These mechanisms are often complex and act at depth, making the investigation and characterization of contributing factors difficult. This poses a problem in the analysis stage of the investigation as uncertainties arise concerning the analysis technique to be employed and what input data is required (Figure 3.1).

STRUCTURE	TYPICAL PROBLEMS	CRITICAL PARAMETERS	ANALYSIS METHODS	ACCEPTABILITY CRITERIA
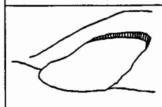 Landslides.	Complex failure along a circular or near circular failure surface involving sliding on faults and other structural features as well as failure of intact materials.	• Presence of regional faults. • Shear strength of materials along failure surface. • Groundwater distribution in slope, particularly in response to rainfall or to submergence of slope toe. • Potential earthquake loading.	Limit equilibrium methods which allow for non-circular failure surfaces can be used to estimate changes in factor of safety as a result of drainage or slope profile changes. Numerical methods such as finite element or discrete element analysis can be used to investigate failure mechanisms and history of slope displacement.	Absolute value of factor of safety has little meaning but rate of change of factor of safety can be used to judge effectiveness of remedial measures. Long term monitoring of surface and subsurface displacements in slope is the only practical means of evaluating slope behaviour and effectiveness of remedial action.
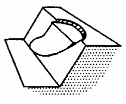 Soil or heavily jointed rock slopes.	Circular failure along a spoon-shaped surface through soil or heavily jointed rock masses.	• Height and angle of slope face. • Shear strength of materials along failure surface. • Groundwater distribution in slope. • Potential surcharge or earthquake loading.	Two-dimensional limit equilibrium methods which include automatic searching for the critical failure surface are used for parametric studies of factor of safety. Probability analyses, three-dimensional limit equilibrium analyses or numerical stress analyses are occasionally used to investigate unusual slope problems.	Factor of safety > 1.3 for "temporary" slopes with minimal risk of damage. Factor of safety > 1.5 for "permanent" slopes with significant risk of damage. Where displacements are critical, numerical analyses of slope deformation may be required and higher factors of safety will generally apply in these cases.
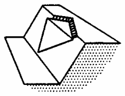 Jointed rock slopes.	Planar or wedge sliding on one structural feature or along the line of intersection of two structural features.	• Slope height, angle and orientation. • Dip and strike of structural features. • Groundwater distribution in slope. • Potential earthquake loading. • Sequence of excavation and support installation.	Limit equilibrium analyses which determine three-dimensional sliding modes are used for parametric studies on factor of safety. Failure probability analyses, based upon distribution of structural orientations and shear strengths, are useful for some applications.	Factor of safety > 1.3 for "temporary" slopes with minimal risk of damage. Factor of safety > 1.5 for "permanent" slopes with significant risk of damage. Probability of failure of 10 to 15% may be acceptable for open pit mine slopes where cost of clean up is less than cost of stabilization.
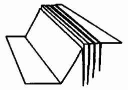 Vertically jointed rock slopes .	Toppling of columns separated from the rock mass by steeply dipping structural features which are parallel or nearly parallel to the slope face.	• Slope height, angle and orientation. • Dip and strike of structural features. • Groundwater distribution in slope. • Potential earthquake loading.	Crude limit equilibrium analyses of simplified block models are useful for estimating potential for toppling and sliding. Discrete element models of simplified slope geometry can be used for exploring toppling failure mechanisms.	No generally acceptable criterion for toppling failure is available although potential for toppling is usually obvious. Monitoring of slope displacements is the only practical means of determining slope behaviour and effectiveness of remedial measures.
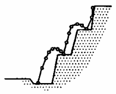 Loose boulders on rock slopes.	Sliding, rolling, falling and bouncing of loose rocks and boulders on the slope.	• Geometry of slope. • Presence of loose boulders. • Coefficients of restitution of materials forming slope. • Presence of structures to arrest falling and bouncing rocks.	Calculation of trajectories of falling or bouncing rocks based upon velocity changes at each impact is generally adequate. Monte Carlo analyses of many trajectories based upon variation of slope geometry and surface properties give useful information on distribution of fallen rocks.	Location of fallen rock or distribution of a large number of fallen rocks will give an indication of the magnitude of the potential rockfall problem and of the effectiveness of remedial measures such as draped mesh, catch fences and ditches at the toe of the slope.

Figure 3.1: Typical problems, critical parameters, methods of analysis and acceptability criteria for slope (Hoek, 1991).

Today, complex numerical analyses of rock slopes are ordinarily performed in rock slope engineering. Actually, a vast range of slope stability analysis tools exist for both rock and mixed rock-soil slopes; these range from simple infinite slope and planar failure limit equilibrium techniques, to sophisticated coupled finite-discrete element codes. Given the wide scope of numerical applications available today, it has become essential to fully understand the varying strengths and limitations of each different methodology.

3.3 Rock slope instability analysis techniques

In rock engineering, a wide range of tools for the analysis of rock slopes are available to the engineer and geoscientist. Stead et al. (2006) propose a flow chart illustrating how rock slope analyses may be undertaken using three levels of landslide sophistications (see Figure 3.2). The key aspect of the approach is the failure mechanism and the concept of progressive failure. Such a concept was originally introduced in the literature to explain discrepancies between average shear stresses calculated from back analysis along failure surfaces in overconsolidated clay slopes and shear strengths of the same clay material in laboratory testing (Bjerrum, 1967).

Level I includes preliminary kinematic and limit equilibrium analysis. These methods are particularly suited to translational failures where basal shear, lateral and rear release all take place on persistent joints, particularly at the residual angle of friction. Such conditions are rare in practice.

Modification to *Level I* techniques has been attempted by many authors to accommodate deformation mechanisms involving step-paths and intact rock fracture (Jennings, 1970; Baczynski, 2000). Other authors have viewed the problem of cohesive strength along a potential failure surface in the context of progressive failure (Bjerrum, 1967). In order to account for a non-persistent failure plane, Terzaghi (1962) included an effective cohesion along the shear surface to allow for the increased resistance to shear failure provided by intact rock bridges. Similarly, consideration has also been given to the development of tensile fractures orthogonal to the non-persistent sliding surface where some stepping is required to allow kinematic release.

Limit equilibrium techniques have found little application toward simulation of progressive failure. This is generally due to the complexity involved in the time-dependent geometrical development, of even the most simple shear surfaces. This highlights a major limitation to the *Level I* techniques, as only processes active along the developing translational shear plane are considered.

Where geometrical constraints on the slide mass are present, this may necessitate

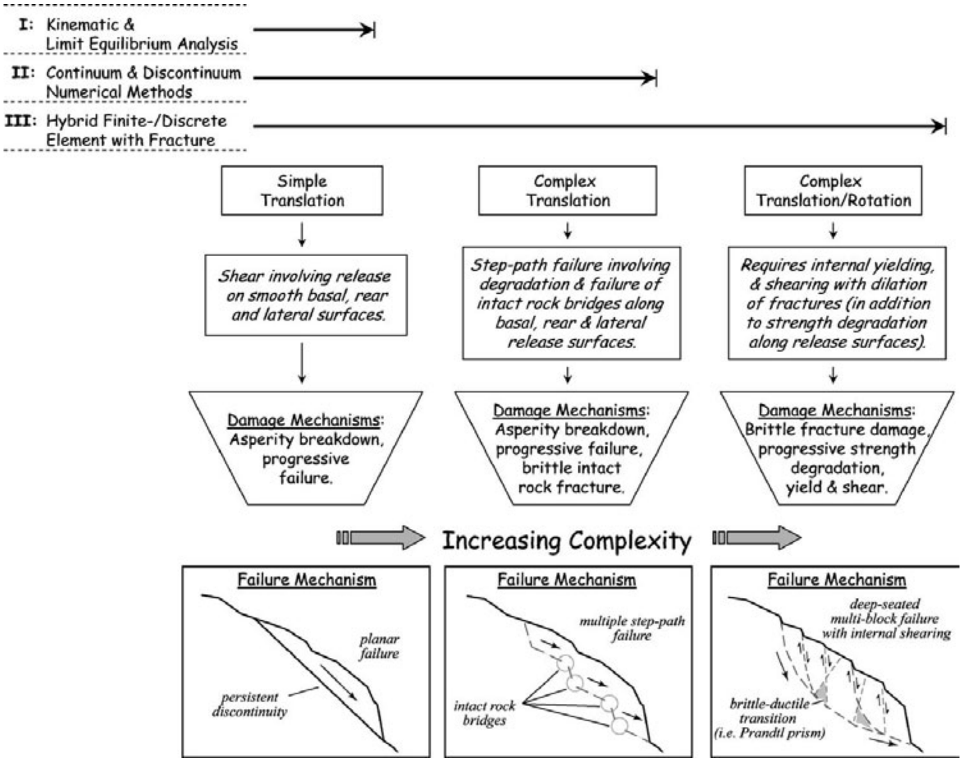

Figure 3.2: Flowchart illustrating three levels of landslide analysis and the mode of translational/rotational failure they apply to (from Stead et al., 2006).

internal deformation, yielding and shearing of the rock mass. Mencl proposed the development of a Prandtl wedge (i.e., damage zone) to explain failure along bi-planar slide surfaces with regard to the 1963 Vaiont slide. This concept was developed further by other authors to simulate the transmission of stresses within a rock slope from an active to passive block along a primary system of plane traversal shear surfaces (Figure 3.3).

The active portion of the slide is bounded by a surface, for example bedding, that is coincident with the slope face. The active block moves downslope creating a “bearing load” on the more stable passive block, leading to rock mass damage, yield and failure between the active and passive blocks. The bearing failure portion of the slide is termed the Prandtl zone and is the transition zone between the active and passive sliding blocks. The Prandtl zone allows the force generated by the active block to be transmitted to the passive block below.

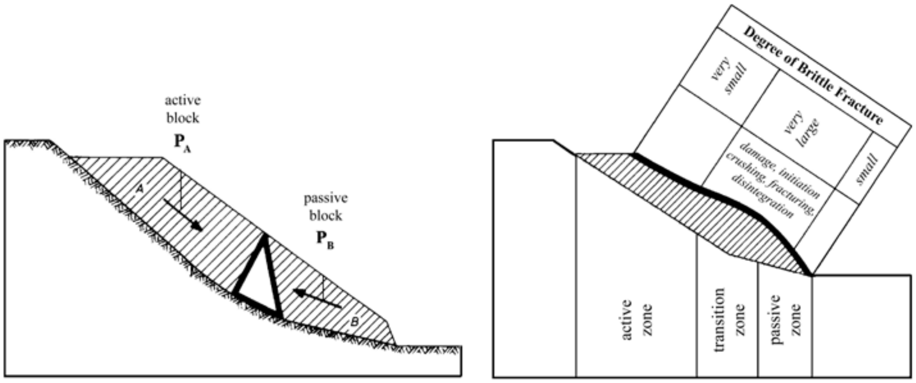

Figure 3.3: Prandtl’s prism transition zone and the corresponding locations of zones with different degrees of fracturing (from Stead et al., 2006).

In summary, the primary kinematic controls on massive rock slope failure can be viewed as both strength degradation in the form of shear plane development (i.e., progressive failure) and strength degradation manifested through internal slide mass deformation (i.e., brittle–ductile yielding or shearing). The latter component is most dominant in situations where the failure surface is non-planar (i.e., transition from *Level I* to *Level II* analyses).

Level II analysis techniques include numerical modelling methods that provide approximate solutions to problems incorporating intact rock deformation (strain) during rock slope failure. Many of these techniques address complexities relating to geometry, material anisotropy, non-linear behaviour, in situ stresses and the presence of several coupled processes (e.g., pore pressures, seismic loading, etc.).

The availability of several numerical modelling codes means that the simulation of potential rock slope failure mechanisms could, and in many cases should, form a standard component of a rock slope investigation.

Level III analyses involve the use of combined continuum-discontinuum codes (also called hybrid codes) with fractures simulation capabilities. These codes are applicable to a wide range of rock slope failure, but are particularly well suited to complex translation/rotational instabilities where failure requires internal yielding, brittle fracturing and shearing and strength degradation along a release surface.

3.4 Conventional methods of rock slope analysis

Conventional methods of rock slope analysis can be generally divided into kinematic and limit equilibrium techniques. These methods are suitable for *Level I* landslide analysis. Table 3.1 provides a summary of the techniques that are routinely applied together with their inherent advantages and limitations (Stead et al., 2006). In addition, analytical computer-based methods have been developed to analyse discrete rock block falls (commonly referred to as rockfall simulators).

Kinematic techniques

Kinematic methods concentrate on the feasibility of translational failures due to the formation of manifested wedges or planes. As such, these methods need a detailed evaluation of rock mass structure and the geometry of existing discontinuity sets that may contribute to block instability (Eberhardt, 2003). This assessment may be carried out by means of stereo-net plots or specialized computer codes which focus on planar and wedge formation.

Limit equilibrium analysis

Limit equilibrium techniques are routinely used in the analysis of landslides where translational or rotational movements occur on distinct failure surfaces. Analyses are undertaken to provide either a factor of safety or, through back-analysis, a range of shear strength parameters at failure.

Analysis method	Critical input parameters	Advantages	Limitations
Stereographic and kinematic	Critical slope and discontinuity geometry; representative shear strength characteristics.	Simple to use and show failure potential. Some methods allow analysis of critical key-blocks. Can be used with statistical techniques to indicate probability of failure and associated volumes.	Suitable for preliminary design or for non-critical slopes, using mainly joint orientations. Identification of critical joints requires engineering judgement. Must be used with representative joint/discontinuity strength data.
Limit equilibrium	Representative geometry, material/joint shear strength, material unit weights, groundwater and external loading/support conditions.	Much software available for different failure modes (planar, circular, wedge, toppling, etc.). Mostly deterministic but some probabilistic analyses in 2-D and 3-D with multiple materials, reinforcement and groundwater profiles. Suitable for sensitivity analysis of FofS to most inputs.	FofS calculations must assume instability mechanisms and associated determinacy requirements. In situ stress, strains and intact material failure not considered. Simple probabilistic analyses may not allow for sample/data covariance.
Rockfall simulation	Representative slope geometry and surface condition. Rock block sizes, shapes, unit weights and coefficients of restitution.	Practical tool for siting structures and catch fences. Can utilize probabilistic analysis. 2-D and 3-D codes available.	Limited experience in use relative to empirical design charts.

Table 3.1: Conventional methods of analysis (Stead et al., 2006).

All limit equilibrium techniques share a common approach based on a comparison of resisting forces/moments mobilized and the disturbing forces/moments. Methods may vary, however, with respect to the slope failure mechanism in question (e.g. translational or rotational sliding), and the assumptions adopted in order to achieve a given solution.

In general, these methods are the most commonly adopted solution methods in rock slope engineering, even though many failures involve complex internal deformation and fracturing which bears little resemblance to the 2D rigid block assumptions required by limit equilibrium analyses. However, limit equilibrium analyses may be highly relevant to simple block failure along discontinuities or rock slopes that are heavily fractured or weathered (i.e. behaving like a continuum equivalent rock mass).

Considerable developments in limit equilibrium approaches have taken place in recent years. 3D limit equilibrium techniques have been developed and 2D limit equilibrium codes now include, for example, probabilistic techniques (e.g. geostatistics), capabilities for including support, improved routines for critical surface searching, integrate groundwater-stress limit equilibrium analysis and incorporation of unsaturated soil mechanics.

Rock fall simulation

In the case of rockfalls, consideration must be given to the design of protective measures near structures endangered by the falling blocks (Eberhardt, 2003). The problem of rockfall protection work, therefore, largely involves the determination of travel paths and trajectories of unstable blocks that have detached from a rock slope face.

Analytical solutions proposed by Hungr and Evans (1988) treat the rock block as a point with a mass and velocity that moves on a ballistic trajectory while in the air, and bounces, rolls or slides when in contact with the slope surface. This is done by reversing and reducing the normal and tangential components of velocity upon contact, through coefficients of normal and tangential restitution. The two restitution coefficients are taken as bulk measures of all impact characteristics, incorporating deformational work, contact sliding and transfers of rotational to translational momentum and vice versa. As a result, the coefficient must depend on fragment shape, slope surface roughness, momentum and deformational properties and, to a large extent, on the chance of certain conditions prevailing in a given impact (Eberhardt, 2003).

3.5 Numerical analysis of rock slope instability

Conventional methods of slope analysis are limited to simplified problems, including simple slope geometries and basic loading conditions, and as such provide little insights into slope failure mechanisms. Many rock slope stability problems involve complexities relating to geometry, material anisotropy, non-linear behaviour, in situ stresses and the presence of several coupled processes (e.g. pore pressures, seismic loading, etc.). To address these limitations, numerical modelling techniques have been proposed to provide approximate solutions to problems, which otherwise would not have been possible to solve using conventional techniques. Numerical methods of analysis used for rock slope stability investigations may be divided into **conventional applications** and **advanced applications** (Stead et al., 2006).

3.5.1 Conventional applications

Conventional numerical modelling approaches may be conveniently subdivided into:

- Continuum methods (e.g., finite element, finite difference, etc.);

- Discontinuum methods (e.g., distinct element; discontinuous deformation analysis, etc.).

Table 3.2 briefly summarizes the characteristics, the advantages and limitations inherent in these different numerical modelling approaches (Stead et al., 2006).

Analysis method	Critical input parameters	Advantages	Limitations
Continuum modelling (e.g., finite element, finite difference)	Representative slope geometry; constitutive criteria (e.g., elastic, elasto-plastic, creep, etc.); groundwater characteristics; shear strength of surfaces; *in situ* stress state.	Allows for material deformation and failure, including complex behaviour and mechanisms, in 2-D and 3-D with coupled modelling of groundwater. Can assess effects of critical parameter variations on instability mechanisms. Can incorporate creep deformation and dynamic analysis. Some programs use imbedded language (e.g., FISH) to allow user to define own functions and subroutines.	Users should be well trained, experienced, observe good modelling practice and be aware of model/software limitations. Input data generally limited and some required inputs are not routinely measured. Sensitivity analyses limited due to run time constraints, but this is rapidly improving.
Discontinuum modelling (e.g., distinct element, DDA)	Slope and discontinuity geometry; intact constitutive criteria (elastic, elasto-plastic, etc.); discontinuity stiffness and shear strength; groundwater and *in situ stress* conditions.	Allows for block deformation and movement of blocks relative to each other. Can model complex behaviour and mechanisms (combined material and discontinuity behaviour, coupled with hydro-mechanical and dynamic analysis). Able to assess effects of parameter variations on instability. Some programs use imbedded language (e.g., FISH) to allow user to define own functions and subroutines.	As above, experienced users needed. General limitations similar to those listed above. Need to simulate representative discontinuity geometry (spacing, persistence, etc.). Limited data on joint properties available (e.g., joint stiffness, jk_n and jk_s).

Table 3.2: Numerical methods of rock slope analysis (Stead et al. (2006)).

Continuum modelling is best suited for the analysis of slopes that consist of massive, intact rock, weak rocks and soil-like or heavily jointed rock masses. Discontinuum modelling is appropriate for slopes controlled by discontinuity behaviour.

Early numerical analyses of rock slopes were predominantly undertaken using continuum finite element codes. Kalkani and Piteau (1976), for example, used this method to analyse toppling of rock slopes at Hells Gate in British Columbia, Canada; preliminary finite element modelling of the Frank Slide in Alberta, Canada, was undertaken by Krahn and Morgenstern (1976). Radbruch-Hall et al. (1976) similarly used a finite element analysis to simulate the stress distributions in rock slopes in order to investigate mechanisms of high mountain deformation and "sackung" formation.

Continuum approaches used in slope stability analysis include the *finite difference* and *finite element methods*. In both these methods the problem domain is discretized into a set of sub-domains or elements. A solution procedure may then be based on numerical approximations of the governing equations, i.e. the differential equations of equilibrium, the strain-displacement relations and the stress-strain equations, as in the case of the Finite Difference Method (FDM). Alternatively, the procedure may exploit approximations to the connectivity of elements, and continuity of displacements and stresses between elements, as in the Finite Element Method (FEM). The use of *finite difference* codes has predominantly involved the use of the FLAC 2D and 3D codes (Itasca, 2005). Both *finite element* and *finite difference* models are ordinarily used in engineering landslide investigations and are most appropriate in the analysis of slopes involving weak rock, soils or rock masses where failure is controlled by the deformation of the intact material (i.e., continuum) or through a restricted number of discrete discontinuities such as a bedding plane or fault.

Where the stability of the rock slope is controlled by movement of joint-bounded blocks and intact rock deformation then the use of discontinuum *discrete element* codes should be considered. *Discrete element* codes have found increasing use in the analysis of rock slopes in recent years. Two principal methods are in use, Distinct Element Method (DEM; Hart, 1993) and Discontinuous Deformation Analysis (DDA; Shi and Goodman, 1985), the former becoming more common in engineering practice. The predominant discontinuum method in use however, is the *distinct element* code UDEC (Itasca, 2005). This code has been used to investigate a wide variety of rock slope failure mechanisms including those ranging from simple planar mechanisms, to complex deep-seated toppling instability (Barla and Chiriotti, 1995; Chiriotti, 1997; Benko and Stead, 1998; Nichol et al., 2002) and buckling (Stead and Eberhardt, 1997). These authors illustrate the need to consider both intact rock and joint-controlled displacements in the analysis of complex rock slope instabilities.

The use of 3D Distinct Element techniques has been more limited to date. Adachi et al. (1991) in an early application of the 3DEC code (Itasca, 2005) analysed toppling slopes along a highway in Japan. Kalenchuk et al. (2010) provide a recent application of the 3DEC code to investigate the Beauregard massive landslide located in the Aosta Valley in northwestern Italy. Numerical simulations of the Beauregard Landslide use three-dimensional mixed continuum-discontinuum methods to explore the role and importance of sophisticated geometric interpretations in analysing landslide mechanics and to test model sensitivity to shear zone strength parameters.

Recent developments in continuum and discontinuum numerical methods allow simulation of complex rock slope failure processes, including:

- hydro-mechanical coupling;
- dynamic analysis;
- advanced and user-defined constitutive criteria (strain softening, creep, damage, etc.);

- support interaction;
- improved integration with empirical rock mass classification schemes.

An example of application of the conventional numerical techniques has been provided by Barla and Chiriotti (1995) who studied the slope stability problems which characterize the Rosone slope deformation, located in northwestern Alps in Italy. Based on the evaluation of the site conditions in terms of geology, structure, and rock mass properties, two sectors of the slope have been analyzed by using the distinct element method and the finite difference method respectively. A number of factors which could adversely affect the stability conditions of the slope in both sectors were evidenced by these models Chiriotti (1997). In the first case, the predominant geological structure with the plane of schistosity dipping down-slope and transient water pressures are shown to be critical factors in slope stability. In the second case, the stability of the slope is controlled mainly by the strong toe buttress and by the groundwater conditions.

Another example of application is given by Eberhardt et al. (2002); the authors use a strain-softening criterion to simulate internal strength degradation and damage contributing to massive rock slope failure and the development of a Prandtl yield zone within a deforming crystalline rock slope. Figure 3.4 shows that a zone of yield due to shear damage develops near the base of the eventual slide surface and transforms into a tensile failure zone as straining occurs. This zone of tensile damage continues upwards through the intact slide mass dividing the rockslide into two distinct blocks, approximating the contact between the first and second failure events of a massive rock slide in southern Switzerland.

3.5.2 Advanced applications

Conventional, *Level II* continuum and discontinuum models although able to simulate certain aspects of progressive shear plane development, often fail to realistically simulate the progressive failure of rock slopes, particularly the dynamics of kinematic release accompanying complex internal distortion, dilation and fracture. Thus, they are not suited to the modelling of progressive failure though brittle fracture initiation and propagation. The importance of developing kinematic release through fracturing in selected mechanisms is a key issue in rock slope analysis that is not addressed by conventional numerical models. Stead et al. (2004) emphasize the need to consider rock slope failures using the principles of fracture mechanics with appropriate consideration of damage, energy, fatigue and time dependency.

Early work to address the influence of fracturing in rock engineering was undertaken by Williams et al. (1985) and Mustoe (1989) who developed a *discrete element* code

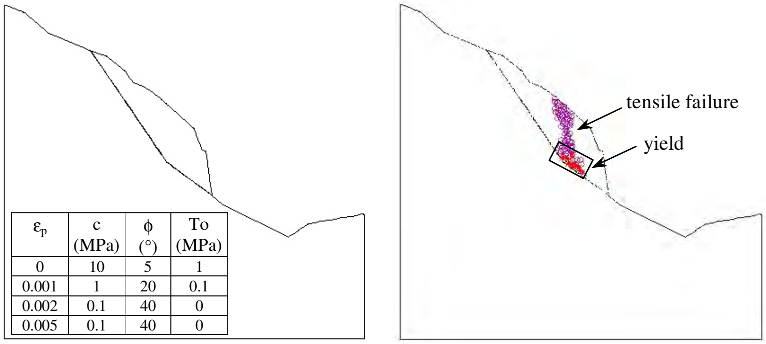

ε_p	c (MPa)	ϕ (°)	To (MPa)
0	10	5	1
0.001	1	20	0.1
0.002	0.1	40	0
0.005	0.1	40	0

Figure 3.4: Distinct-element strain-softening model showing development of Prandtl yield zone at base of slide surface and propagation of tensile damage upwards through intact slide mass, dividing the slide mass along the contact between first and second rockslide events (from Eberhardt et al., 2002).

that incorporated fracturing through a Mohr–Coulomb criterion with a tension cut-off. Through their algorithms, an element could fracture through its centroid or along an element edge. Cundall and Strack (1979) adopted a variation of the *discrete element* method to simulate particular material behaviour. This led to the development of the Particle Flow Code, PFC Itasca (2005), in which clusters of particles can be bonded together to form joint-bounded blocks. This code is capable of simulating fracture of the intact rock blocks through the stress-induced breaking of bonds between the particles. This is a significant development as it allows the influence of internal slope deformation to be investigated both due to yield and intact rock fracture of jointed rock.

It is evident from both rock slope observations and intensive fragmentation occurring during the failure process that intact brittle fracture mechanisms are an important component of many failures. A major weakness of the previously described methodologies is that they only imitate intact rock fracture; they do not follow basic principles related to brittle fracture mechanics.

A new numerical approach was proposed by Munjiza (Munjiza, 2004) in the early 1990s. The new method combines the advantage of both FEM and DEM into a *combined finite-discrete* modelling methodology (Table 3.3), called FEM/DEM (reported as FDEM). In FDEM each discrete element is discretised into finite elements meaning that there is a finite element mesh associated with each discrete element. The method is suitable to model intact behaviour, interactions along existing discontinuities and, when incor-

Analysis method	Critical input parameters	Advantages	Limitations
Particle flow code (e.g., PFC, ELFEN)	Problem geometry, particle shape, size and size distribution; particle density, bond stiffness and strength (normal and shear); bonding type and tightness of packing configuration.	Ideal for simulating particle flow, but can also simulate behaviour of solid material (e.g., intact or jointed rock) through bonded assemblage of particles, most notably the fracturing and disintegration of the bonded assemblage. Dynamic analysis possible, as well as 2-D and 3-D simulations. Some programs use imbedded language (e.g., FISH) to allow user to define own functions and subroutines.	Input parameters are based on micromechanical properties, requiring calibration through simulation of laboratory testing configurations (i.e., to correlate particle bonding properties to Young's modulus, compressive strength, etc.). Particles are rigid and often cylindrical (2-D) or spherical (3-D). Simulation of brittle fracture not based on physical laws/principles of fracture mechanics.
Hybrid finite-/discrete-element codes (e.g., ELFEN)	Combination of input parameters listed in Table 2 for both continuum and discontinuum stand alone models (e.g., elastic, elasto-plastic, etc., for continuum; stiffness, shear strength, etc., for discontinuities); damping factors; tensile strength and fracture energy release rate for fracture simulation.	Combines advantages of both continuum and discontinuum methods. Coupled finite-/discrete-element models able to simulate intact fracture propagation and fragmentation of jointed and bedded media. Incorporates efficient automatic adaptive re-meshing routines. Dynamic, 2-D and 3-D analyses possible using wide variety of constitutive models (plastic, visco-plastic, etc.).	Complex problems require high memory capacity. Comparatively little practical experience in use. Requires ongoing calibration and constraints. Yet to be coupled with groundwater.

Table 3.3: Advanced hybrid numerical methods of analysis (Stead et al., 2006).

porating fracture mechanics principles, the initiation and development of new fractures (i.e., the transition from a continuum to a discontinuum). Eberhardt (2006) identifies the *combined finite-discrete element method* suitable for *Level III* of landslide analysis.

The *combined finite-discrete element method* was implemented in the Munjiza's Y code (Y2D, Munjiza, 2004). ELFEN (Rockfield, 2004) is another example of *combined finite-discrete element* code, which enables the modelling of brittle fracture initiation and propagation through adaptive remeshing techniques coupled with contact search algorithms. The program uses a finite element mesh to represent the intact joint bounded blocks and discrete elements to model joint behaviour. The simulation of fracturing, damage and associated softening within a rock slope prior to and during failure is accomplished using a fracture energy approach.

Stead et al. (2006) illustrate several examples of rock slope analyses performed using the *combined finite-discrete element* code ELFEN. The first example is the simulation of step-path geometries. Figure 3.5 illustrates an ELFEN model of a translational failure requiring intact fracture between two joint sets to allow kinematic release. Excess shearing stresses along a discontinuity result in the propagation of orthogonal tensile fractures until eventually cross over fractures provide a continuous, but stepped, failure surface and overall failure occurs. Step-path feature is not restricted to basal shear surface development but are also important in the development of lateral and rear release surfaces. Although a 3D global step path failure has yet to be considered, the process is undoubtedly extremely important in localized failure throughout massive deforming rock slope masses. Time dependent degradation of the cohesive and tensional strength of both discontinuities and the intact rock mass are of significant importance (Stead et al., 2006).

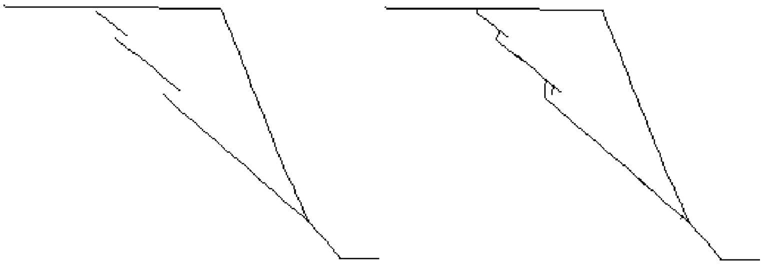

Figure 3.5: Simulation of a stepped-path failure through a 100 m high rock slope (from Stead et al., 2006).

Bi-planar rock slope failure is the second example studied by Stead et al. (2006). As

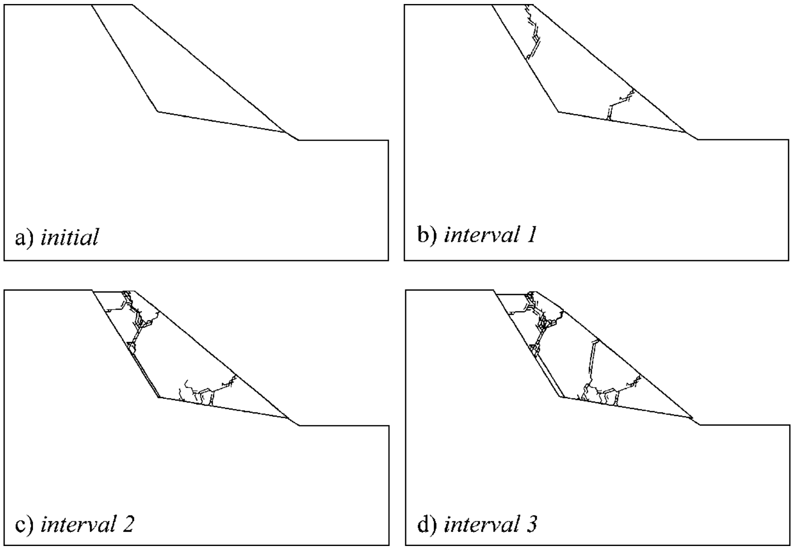

Figure 3.6: Simulation of a 50 m high rock slope with a bi-planar (active-passive) failure surface, showing the initial problem geometry and three stages of fracture release, leading to the kinematic release and failure (from Stead et al., 2006).

previous described, early *Level I* analyses of this failure mechanism were proposed using an active-passive wedge approach by Mencl (1966). An interface was assumed between an upper active driving block and a lower passive or resisting block in order to allow a solution that satisfied the kinematics of the failure geometry. The active–passive wedge approach or non-circular methods of slices have been applied to rock slope geometries where the upper failure surface may for example be a high angle fault and the lower failure surface along weak bedding planes or intra formational shears. Stead and Eberhardt (1997) illustrate the application of discontinuum modelling techniques to the analysis of active–passive failures in surface coal mine footwalls. Major rockslides, such as the Vajont slide, have exhibited a similar active–passive wedge or chair-shaped failure surface geometry in which internal yielding and fracturing within the rock slope must occur for kinematic release. Evidence of this internal distortion and fracturing can be observed as surface faults and graben features within the post failure topography.

Figure 3.6 illustrates a *combined finite-discrete element* model of a bi-planar failure geometry showing the stages in the development of brittle internal fracturing that accompanies rock slope failure and kinematic release. The development of tensile fractures above and below the intersection of the upper and lower failure surfaces is evident. These are followed at a later stage by the development of a wedge interface fracture. Stead et al. (2006) suggest that intact fracture can realistically simulate the complex processes that occur in such massive bi-planar rock slopes failures or indeed wherever the failure surface has rapid changes in curvature.

3.5.3 Total Slope Failure approach

By using *combined finite-discrete element* techniques with brittle fracture propagation, Stead et al. (2006) state that a first step may be taken in what they term a "total slope failure" analysis. This is in marked contrast to traditional rock engineering approaches where the analysis of rock slopes has emphasized either the initiation mechanism or the transport/deposition stage. Figure 3.7, modified after Stead et al. (2006), shows the varied stages of the "total slope failure" analysis with the appropriate *Level I*, *II* and *III* analysis codes.

Conventional *Level I* approaches have been used to characterize the hazard presented by the failure initiation using 2D and 3D deterministic limit equilibrium techniques. If the true risk is to be ascertained, then the characteristics of the deformation as a precursor to failure and the post failure movement must be linked to the initiation analysis (Stead et al., 2006). This requires a detailed rock mass characterization in order to allow a combination of continuum, discontinuum and hybrid approaches. Specifically, additional data is required to constrain the degree of intact fracturing either associated with

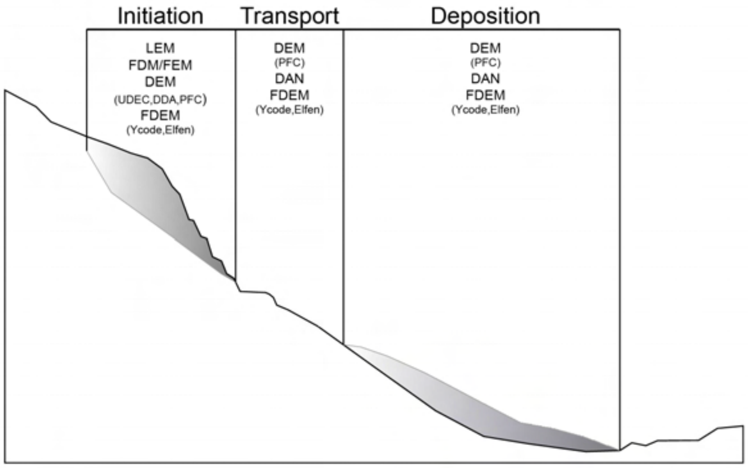

Figure 3.7: Stages of a "total slope failure" analysis with the appropriate *Level I*, *II* and *III* analysis codes (from Stead et al. 2006, modified).

failure, in a back-analysis scenario, or the probability for release, in a hazard assessment investigation. Field data should be gathered throughout the initiation, transportation and deposition zones in order to constrain the degree of comminution associated with failure, and similar controls on debris characteristics (e.g., block size, jointing, tensile strength). The transportation and comminution stage follows the initiation of failure. Comminution may be visualized as occurring both during initial rock failure and during the gravity driven rock debris transport. Both *particle flow* codes and *combined finite-discrete element* codes with fracture propagation have been shown to be suitable for the modelling of rock debris transport.

Stead et al. (2006) suggest that *Level III* codes offer immense potential in furthering the knowledge of the mechanisms and processes at work during the breakdown of the slope mass continuum through failure initiation, transportation and deposition, that is, the "total slope failure". This is essential in order to develop robust recommendations with regard to rockslide run-outs and the associated temporal and spatial risks due to massive rock slope failure.

3.6 The study of massive rock slope instability

The study of massive rock slope instability problems, in general, has largely been descriptive and qualitative. Studies that focus on some quantitative aspect of large-scale mass movements are often limited to individual processes or triggering mechanisms (e.g. correlating landslide activity with heavy precipitation events). As such, traditional treatments have primarily been directed towards phenomenological methodologies, both in terms of monitoring, prediction and stability analysis (Eberhardt, 2006).

Phenomenological-based approaches represent the interpretation of large-scale observations/measurements with the purpose of translating them into a usable form for engineering design (e.g. an empirical relationship, a failure criterion, etc.). One of the more common phenomenological techniques, employed in rock slope stability investigations, involves the use of surface displacement measurements recorded over time, which are then extrapolated or analysed for accelerations in order to predict catastrophic failure. Such measurements are commonly used as a form of early warning system and may cover a variety of scales, from that of a crack meter spanning an open tension crack to a system of geodetic measuring points covering an entire slope (Eberhardt, 2006).

Significant advancements have been made through these techniques, yet success is variable. In the literature there are many studies which have extrapolated displacement versus time plots, to predict the correct date of catastrophic collapse. The collapse criterion is usually a displacement value based on engineering judgement, displacement data, rock mass quality and lessons learned from previous failure. In this sense, the adopted methodology was purely phenomenological and relied heavily on experience gained over time.

Extrapolation of displacement *versus* time records to predict catastrophic failure had a successfully application at the Chuquicamata mine in the Chilean Andes. In contrast, such an approach have led to incorrect forecasts, for example at Kilchenstock in the Swiss Alps (Eberhardt, 2006). The case of Kilchenstock may have occurred 70 years ago, but today, the same phenomenological-based "displacement versus time" analyses are still being employed and often with the same variability in terms of success.

Such examples demonstrate the inherent difficulty in relying on phenomenological-based analyses in which the mechanisms of the problem are largely ignored. The prevalent use of surface displacement measurements obviously addresses certain economic restraints in terms of what may be feasible for on-site monitoring of a given rock slope. Yet it must also be asserted that only so much can be inferred at surface when the problem itself transpires at depth. Thus lies the problem in relying solely on phenomenological methodologies (Eberhardt, 2006).

3.6.1 Progressive failure in massive rock slopes

In massive natural rock slopes, potential failure surfaces are often considered as being extensive, continuous planes. The justification for this is partly due to post-failure observations where fully persistent discontinuities are fitted to the failure surface to explain its origin in a geological context, and partly due to the constraints of the analysis technique employed (many of which require the input of fully persistent discontinuities, e.g. limit equilibrium wedge or planar analysis, DEM, etc.). Such assumptions are often only valid in cases where the volume of the failed block is relatively small (e.g. 1000 m^3) or where major persistent faults or bedding planes are present (Eberhardt et al., 2003).

In contrast, Terzaghi (1962) argues that the persistence of key discontinuity sets is in reality more limited and that a complex interaction between existing natural discontinuities and brittle fracture propagation through intact rock bridges is required to bring the slope to failure. Eberhardt et al. (2003) state that such processes must be considered to explain the temporal nature of massive natural rock slope failures. For example, prior to failure a particular rock slope may have existed in a relatively stable state over periods of thousands of years (e.g. since deglaciation), having experienced major precipitation and snow melt events, and seismic activity over time. Thus, unless failure is driven by external changes to the geometry of the problem (e.g. undercutting, erosion at the toe, etc.) or addition of external loads through human activity, a component of strength degradation with time must occur within the rock mass. In effect, such processes are similar to those proposed by Bjerrum (1967) and others, indicated as progressive failure.

The key aspect of progressive failure in rock slopes is that the process is predominantly driven by the propagation of fractures (e.g. through intact rock bridges between existing discontinuities), and strength degradation, strain softening, internal deformation and dilation through increasing brittle fracture, damage and shearing (Eberhardt et al., 2003).

Figure 3.8 illustrates the primary conceptual controls contributing to massive rock slope failure viewed as a function of strength degradation in the form of shear plane development and strength degradation manifested through internal deformation, dilation and damage mechanisms. For example, Martin and Kaiser (1984) showed that these internal shears, and the internal distortions that occur along them, are necessary in certain modes of rock slope instability to accommodate motion along a basal sliding surface. Depending on the complexity of the geology, topography and subsurface structure, these controls will vary in their influence on the overall instability state.

To treat these problems, new developed *combined finite-discrete element* codes have been proposed because they allow for the modelling of both intact behaviour and the development of fractures.

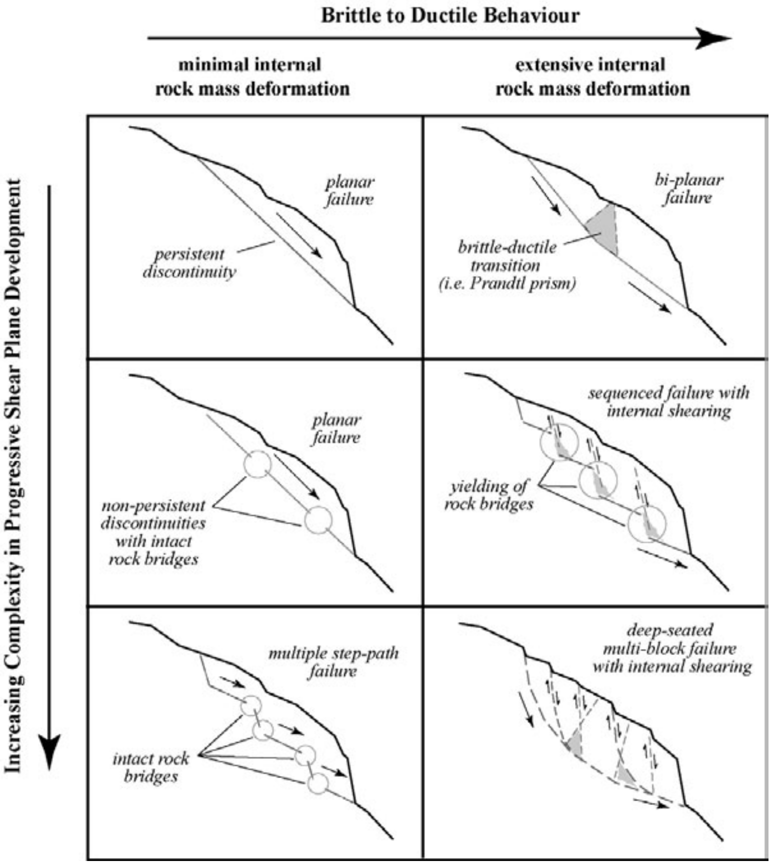

Figure 3.8: Massive rock slope sliding mechanisms as controlled by progressive shear plane development and internal rock mass damage (Eberhardt et al., 2003).

3.6.2 The Total Slope Failure approach applied to massive rock slope instability

In the literature applications of the "total slope failure" approach (i.e. *Level III* analyses) to the study of massive rock slope instability have been recently proposed by several authors. The first published use of the *combined finite-discrete element* method in rock slide simulation using the total slope failure approach was proposed by Eberhardt et al. (2003). They have undertaken a preliminary ELFEN modelling of the April-May 1991 Randa rockslide, Switzerland. The ELFEN model complements continuum and discontinuum models (i.e. *Level II* analyses) previously undertaken by Eberhardt et al. (2004). As described in their study, the geology of the Randa rock slope comprises predominantly gneiss with several well developed joint sets (Figure 3.9). Modelling analyses have emphasized the importance of progressive rock mass degradation and damage within the rock slope prior to eventual slope failure. This damage appears to be rooted as far back as the initial unloading of the rock slope during deglaciation, which has been shown to result in tensile damage at the slope toe. Figure 3.10 shows the failure process at different stages.

These analyses used as input the observed rock slide failure surfaces and were undertaken to illustrate the potential of the *combined finite-discrete element* method in simulating the progressive fragmentation of the rock slope mass both during initiation, transportation and deposition, that is "during the total slope failure process". Modelling also showed that internal deformation and damage within the slope mass due to strength degradation would result in brittle-ductile transition processes subdividing the slide mass into two key units through sub vertical tensile brittle fracturing. These model results closely agree with the observed boundaries delineating the two slide phases constituting the 1991 Randa rockslide. Furthermore, the inclusion of tensile brittle fracture processes using the combined modelling techniques provided important insights as to the underlying mechanisms corresponding to the episodic nature of the rockslide and its relatively short run out distance when compared to other major rockslides of comparable volumes (Stead and Coggan, 2006).

Another example of total slope failure analysis proposed by the same authors was the simulation of the Elm rockslide, occurred on 1881 and resulted in the loss of 115 lives. It is described in Heim's classic work "Landslides and Human Lives" (Heim, 1932), as a clear example of what he termed "rubble stream" phenomenon in rock avalanche run out. The rockslide occurred within fine cleavage slates quarried at the slope toe and dipping into the mountain at 30°. The rock slope mass also comprises flysch sandstone, greensands and glauconitic limestones.

Stead and Coggan (2006) presented a preliminary analysis of the Elm rockslide based on the Heim's section (Figure 3.11). In this analysis the development of fracturing due

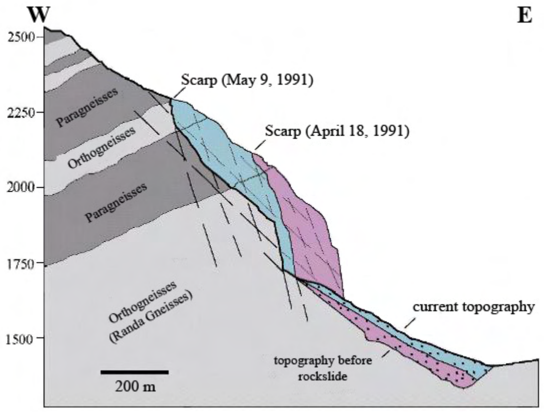

Figure 3.9: Geological section and geometry of the 1991 Randa rockslides (Stead and Coggan, 2006).

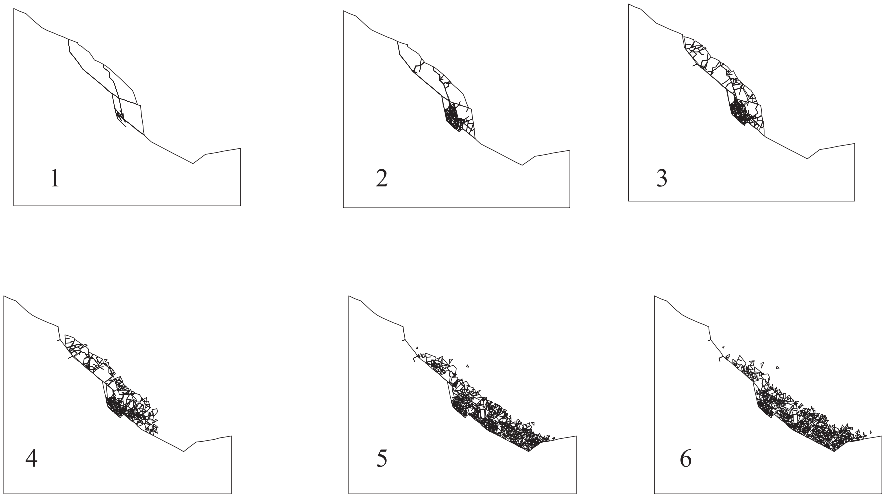

Figure 3.10: Combined finite-discrete element analysis of the Randa rockslide showing several stages of progressive brittle fracture (Stead and Coggan, 2006).

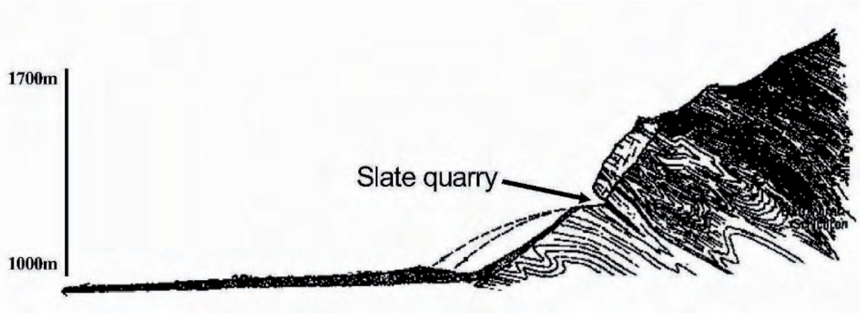

Figure 3.11: The Elm rockslide, 1881 after Heim (1932).

to the quarry at the toe was simulated along with the run out of a dry fragmented rock mass. Figure 3.12 illustrates stages in the rock slope failure and run-out. Initial results had been promising in terms of the comparative run-out magnitude simulated assuming frictional transport. Preliminary ELFEN analyses assumed properties for a weak highly anisotropic rock mass (Stead and Coggan, 2006).

Stead and Coggan (2006) used the total slope failure approach to study the rock slope failure at Delabole Slate quarry in Devon, U.K. The Delabole rockslide had been previously studied by Coggan and Pine (1996) who undertook UDEC discontinuum modelling (i.e. *Level II* analyses). Figure 3.13 shows the pre and post failure geometry. The mechanism of the failure has been described as due to the two blocks in the upper part of the slope promoting toppling and sliding of the lower blocks. Toppling mechanisms are indicated by both UDEC modelling and a long period of surface slope monitoring using tension crack gauges and electronic distance meters (EDM). Selected stages of the *combined finite-discrete element* simulation of the Delabole failure are illustrated in Figure 3.13.

Through the adoption of new combined numerical modelling techniques, the results presented demonstrate the value of explicitly modelling brittle fracture processes in understanding complex rock slope failure mechanisms.

Rock slope simulations incorporating concepts relating to progressive strength degradation and failure show that pre-existing fully persistent geological structures are not necessary to explain failure. Instead, models using the *combined finite-discrete element* method suggest a failure process largely driven by the initial formation of brittle tensile fractures, eventually leading to shear failure and mobilization once the rock mass cohe-

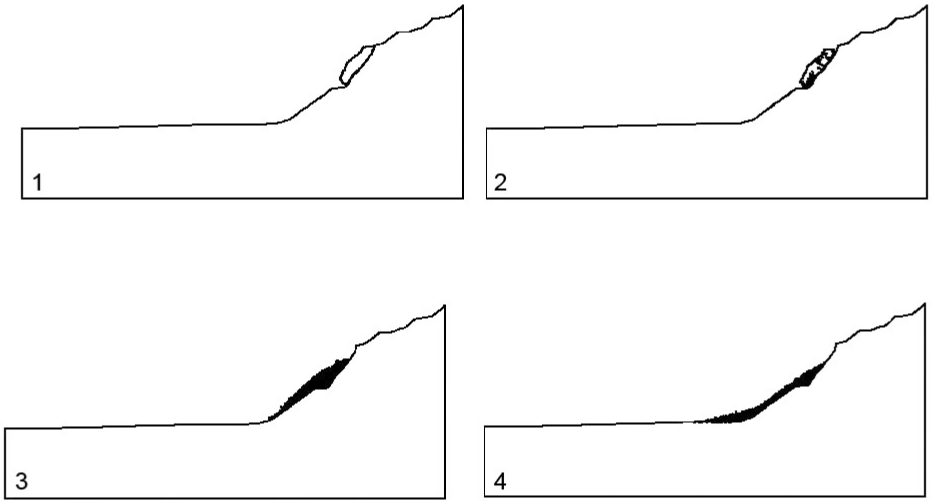

Figure 3.12: Stages in the combined finite-discrete element simulation of the Elm slide (Stead and Coggan, 2006).

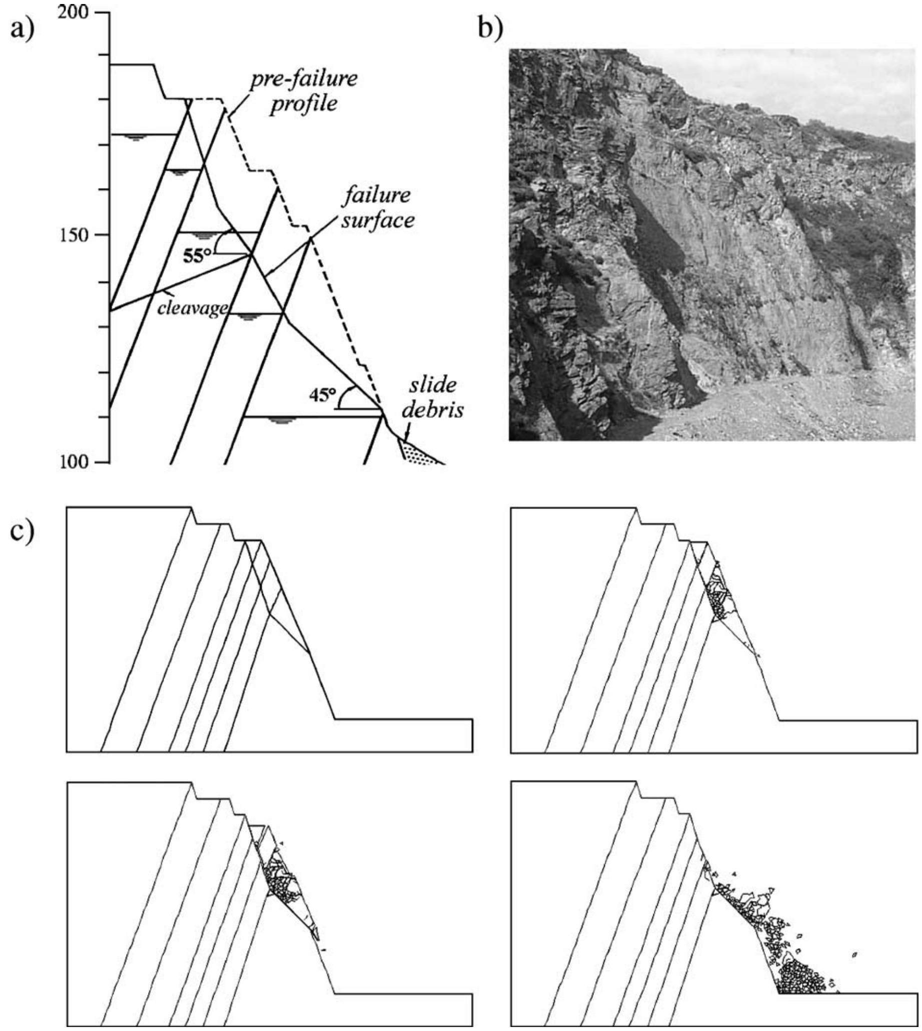

Figure 3.13: Combined finite-discrete element "total slope failure" analysis of the Delabole slate quarry failure in the U.K., showing: (a-b) cross-section and photo of the rockslide scarp; (c) stages from initial failure to run out obtained by ELFEN numerical simulation (Stead and Coggan, 2006).

sion is significantly degraded. In other words, shear failure only becomes a factor after enough tensile fracture damage is incurred to allow mobilization.

Barla et al. (2011) proposed an early application of the Munjiza's Y2D code, based on the *combined finite-discrete element* method, to the rockslides observed at the Alpetto open pit mine in Italy. On the 28-29th June 1997 a severe instability occurred at the Alpetto open pit mine where majolica is mined to manufacture cement. The instability occurred along a section in the eastern zone, during a persistent and intensive rainfall event and extended from the toe to the crest of the main exploitation front, for a total height of 130 m, involving an estimated volume of 50000 m^3 (Figure 3.14). A back analysis of the rock slide and the assessment of the stability conditions of the high-cuts in the western sector were part of a comprehensive study of the mine slopes performed after the failure (Barla et al., 2003). The Y2D model complements continuum and discontinuum models previously undertaken; the focus was posed on the capability of the *combined finite-discrete element* method to simulate the evolution and run out of the instabilities. Figure 3.14 shows different consecutive screenshots of the numerical simulation of the Alpetto mine rockslide performed with the Y2D code. The results obtained shown in terms of run out profiles are in good agreement with site observation and numerical modelling previously conducted with the distinct element method (Figure 3.15).

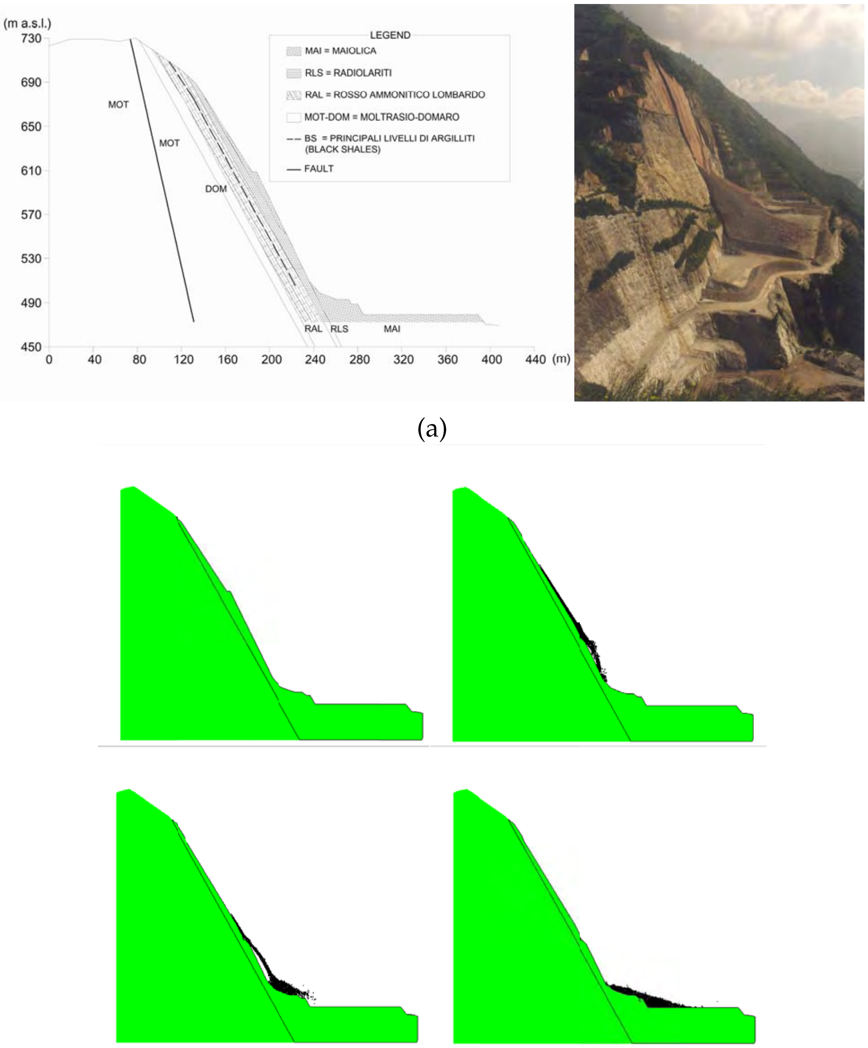

(a)

(b)

Figure 3.14: The Alpetto mine rockslide, 1997. a) cross section and photo of the rockslide, b) progressive failure simulated with Y2D code (Barla et al., 2011).

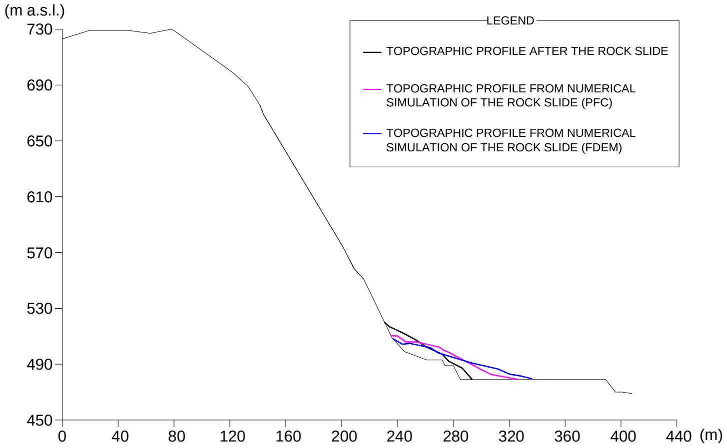

Figure 3.15: Final topographic profile obtained with numerical simulations (PFC and FDEM) compared with the 1997 landslide profile (Barla et al., 2011).

3.7 Summary

This chapter illustrates the wide range of tools available for the analysis of rock slopes with particular emphasis on advanced numerical modelling methods that allow realistic simulations of rock slope failure. The analysis of rock slope stability has changed significantly during recent years with a transition from limit equilibrium analyses to the application of numerical modelling. These techniques have evolved to allow routine analysis treating the slope mass as either a continuum (e.g. finite-element method) or a discontinuum (e.g. discrete-element method). Furthermore, the complexity which characterizes most landslides from massive rock slope failure involves elements of both deformation of the continuum, interactions along existing discontinuities and the creation of new fractures.

To treat these problems, new developments in combined finite-discrete element codes have been proposed. These codes have demonstrated the significant potential in the analysis of “total slope failure processes”, from initiation through transportation comminution to deposition. It must be emphasized that advanced numerical methods offer the chance to simulate the complex mechanisms of failure, like those described in the previous chapter, which characterize the landslide from massive rock slope failure. Even though the advanced numerical techniques are useful to study the rock mass failure from a “total slope failure processes” perspective, it is recognized that numerical modelling is only a tool and not a substitute for critical thinking and judgement. Still, through the proper use of numerical modelling, key steps can be taken to transcend the phenomenological methodologies that dominate massive rock slope stability investigations today, thereby improving the visualization and understanding of the coupled processes and complex mechanisms driving such instabilities.

References

Adachi, T., Ohnishi, Y., and Arai, K. (**1991**). "Investigation of toppling slope failure at route 305 in Japan." In Wittke, editor, "Proceedings of the 7th International Congress on Rock Mechanics, Aachen, Germany," volume 2, pages 843–846. Balkema.

Baczynski, N. (**2000**). "Stepsim4 - Step path method for slope risks." In "Proceedings GeoEng2000, International Conference on Geotechnical and Geological Engineering," Melbourne.

Barla, G., Barla, M., Chiappone, A., Rabagliati, U., and Repetto, L. (**2003**). "Continuum and discontinuum modelling of a high rock cut." In "ISRM 2003. Technology roadmap for rock mechanics, South African Institute of Mining and Metallurgy," .

Barla, G. and Chiriotti, E. (**1995**). "Insights into the behaviour of the large deep-seated gravitational slope deformation of Rosone, in the Piemonte Region (Italy)." *Felsbau, Proc. of 44th Geomechanics Colloquium, Salzburg*, 6: 425–432.

Barla, M., Piovano, G., and Grasselli, G. (**2011**). "Rock slide simulation with the combined finite discrete element method." *International Journal of Geomechanics*.

Benko, B. and Stead, D. (**1998**). "The Frank slide: a reexamination of the failure mechanism." *Canadian Geotechnical Journal*, 35: 299–311.

Bjerrum, L. (**1967**). "Progressive failure in slopes of overconsolidated plastic clay and clay shales." *Journal of Soil Mechanics and Foundation Division of the ASCE*, 93: 1–49.

Chiriotti, E. (**1997**). *Mathematical modelling of the behaviour of the large deep-seated gravitational slope deformation of Rosone (in italian).* Ph.D. thesis, Politecnico di Torino, Turin, Italy.

Coggan, J. and Pine, R. (**1996**). "Application of distinct-element modelling to assess slope stability at Delabole slate quarry, Cornwall, England." *Transactions of the Institution of Mining and Metallurgy. Section A: Mining Industry*, 105: A22–A30.

Cruden, D. and Varnes, D. (**1996**a). *Landslides: Investigation and Mitigation*, chapter 3 - landslide types and processes, pages 36–75. National Academy Press, Washington, D.C.

Cundall, P. and Strack, O. (**1979**). "A discrete numerical model for granular assemblies." *Géotechnique*, 29: 47–65.

Eberhardt, E. (**2003**). "Rock Slope Stability Analysis - Utilization of Advanced Numerical Techniques." Technical report, Earth and Ocean Sciences at UBC - Vancouver, Canada.

Eberhardt, E. (**2006**). "From cause to effect usign numerical modelling to understand rock slope instability mechanisms." In S. G. Evans, G. Scarascia Mugnozza, A. L. Strom, and R. L. Hermanns, editors, "Landslides from Massive Rock Slope Failure," volume 49 of *NATO Science Series: IV: Earth and Environmental Sciences*, pages 85–101. Springer Netherlands.

Eberhardt, E., Kaiser, P. K., and Stead, D. (**2002**). "Numerical analysis of progressive failure in natural rock slopes." In "EUROCK 2002. Proceedings of the ISRM International Symposium on Rock Engineering for Mountainous Regions, Funchal, Madeira," pages 145–153.

Eberhardt, E., Stead, D., and Coggan, J. (**2004**). "Numerical analysis of initiation and progressive failure in natural rock slope - the Randa rockslide." *International Journal of Rock Mechanics & Mining Sciences*, 41: 69–87.

Eberhardt, E., Stead, D., Coggan, J., and Willenberg, H. (**2003**). "Hybrid finite-discrete element modelling of progressive failure in massive rock slopes." In "ISRM 2003 - Technology roadmap for rock mechanics," pages 275–280. South African Institute of Mining and Metallurgy.

Hart, R. D. (**1993**). "An Introduction to Distinct Element Modeling for Rock Engineering." In J. A. Hudson, editor, "Comprehensive Rock Engineering: Principles, Practice and Projects," volume 2, pages 245–261. Pergamon Press.

Heim, A. (**1932**). *Bergsturz und Menschelenben (Landslide and Human Lives, translated by Nigel Skermer, 1989, BiTech Publishers, Vancouver).* Fretz and Wasmuth Verlag, Zurich.

Hoek, E. (**1991**). "When is a rock engineering design acceptable." In A.A., editor, "Proceedings of the 7th international Congress on Rock Mechanics," pages 1495–1497. Balkema.

Hungr, O. and Evans, S. (**1988**). "Engineering evaluation of fragmental rockfall hazards." In C. Bonnard, editor, "Proceedings of the 5th International Symposium on Landslides, Lausanne," volume 1, pages 685–690. Balkema, Rotterdam.

Itasca (**2005**). *Itasca Software Products - FLAC, FLAC3D, UDEC, 3DEC, PFC, PFC3D*. Itasca Consulting Group Inc., Minneapolis.

Jennings, J. (**1970**). "A mathematical theory for the calculation of the stability of slopes in open-cast mines." In P. van Rensburg, editor, "Proceedings of Open Pit Mines Symposium, Johannesburg," pages 87–102. Southern African Institute of Mining and Metallurgy, Balkema.

Kalenchuk, K., Hutchinson, D., Diederichs, M., Barla, G., Barla, M., and Piovano, G. (**2010**). "Three dimensional mixed continuum discontinuum numerical simulation of the Beauregard Landslide." In "EUROCK 2010. Proceedings of the European Rock Mechanics Symposium," Lausanne.

Kalkani, E. and Piteau, D. (**1976**). "Finite element analysis of toppling failure at Hell's Gate Bluffs, British Columbia." *Bull. Assoc. Eng. Geol.*, 13: 315–327.

Krahn, J. and Morgenstern, N. R. (**1976**). "Mechanics of the Frank slide." In "Rock Engineering for Foundations and Slopes, ASCE Geotech. Eng. Specialty Conf., Boulder (Colorado)," volume 1, pages 309–331.

Martin, C. D. and Kaiser, P. K. (**1984**). "Analysis of a rock slope with internal dilation." *Canadian Geotechnical Journal*, 21(4): 605–620.

Mencl, V. (**1966**). "Mechanics of landslides with non-circular slip surfaces with special reference to the Vaiont slide." *Géotechnique*, 16 (4): 329–337.

Munjiza, A. (**2004**). *The Combined Finite-Discrete Element Method*. Wiley.

Mustoe, G. G. W. (**1989**). "Special elements in discrete element analysis." In G. Mustoe, M. Henriksen, and H.-P. Huttelmaier, editors, "Proceedings of the 1st U.S. Conference on Discrete Element Methods," CSM Press, Golden (Colorado).

Nichol, S. L., Hungr, O., and Evans, S. G. (**2002**). "Large scale brittle and ductile toppling of rock slopes." *Canadian Geotechnical Journal*, 39: 773–788.

Radbruch-Hall, D. H., Varnes, D. J., and Savage, W. Z. (**1976**). “Gravitational spreading of deep-seated ridges ("Sackung") in Western United States.” *Engineering Geology*, 14: 23–35.

Rockfield (**2004**). *ELFEN 2D/3D Numerical Modeling Package*. Rockfield Software Ltd, Swansea.

Shi, G. H. and Goodman, R. E. (**1985**). “Two dimensional discontinuous deformation analysis.” *International Journal for Numerical and Analytical Methods in Geomechanics*, 9(6): 541–556.

Stead, D. and Coggan, J. (**2006**). “Numerical modelling of rock slopes using total slope failure approach.” In S. G. Evans, G. Scarascia Mugnozza, A. L. Strom, and R. L. Hermanns, editors, “Landslides from Massive Rock Slope Failure,” volume 49 of *NATO Science Series: IV: Earth and Environmental Sciences*, pages 129–138. Springer Netherlands.

Stead, D., Coggan, J. S., and Eberhardt, E. (**2004**). “Realistic simulation of rock slope failure mechanisms: the need to incorporate principles of fracture mechanics.” In “Regional ISRM Sinorock 2004 Symposium, International Journal of Rock Mechanics and Mining Sciences,” volume 41, pages 1–6.

Stead, D. and Eberhardt, E. (**1997**). “Developments in the analysis of footwall slopes in surface coal mining.” *Engineering Geology*, 46(1): 41–61.

Stead, D., Eberhardt, E., and Coggan, J. (**2006**). “Developments in the characterization of complex rock slope deformation and failure using numerical modelling techniques.” *Engineering Geology*, 83: 217–235.

Terzaghi, K. (**1962**). “Stability of steep slopes in hard unweathered rock.” *Geotechnique*, 12: 251–270.

Williams, J., Hocking, G., and Mustoe, G. (**1985**). “The theoretical basis of the discrete element method.” In J. Middleton and G. N. Pande, editors, “NUMETA 85. Proceedings of the International Conference on Numerical Methods in Engineering, Theory and Applications, Swansea,” pages 897–906.

Chapter 4

The Combined Finite-Discrete Element Method

4.1 Introduction

As described in the previous chapter, numerical modelling is an unavoidable tool for better understanding the behaviour of rock masses. Although both continuum and discontinuum numerical analyses provide useful means to study rock slope stability problems, advanced numerical techniques such as hybrid methods can better represent the complexity of landslides from massive rock slope failure. For this purpose, the combined finite-discrete element method is the most suitable numerical technique in order to apply the total slope failure approach to complex mechanisms of failure.

After introducing the numerical methods commonly applied in rock engineering and based on previous work made by Jing (2003), the general formulation of the combined finite-discrete element method is described. The description of principal algorithms is based on the textbook "The Combined Finite-Discrete Element Method" authored by Munjiza (Munjiza, 2004).

4.2 Numerical modelling of rock masses

The reason for the general difficulty in modelling rock masses, by whatever numerical method, is that rock is a natural geological material, and so the physical or engineering properties have to be established, rather than defined through a manufacturing process.

The rock mass is largely Discontinuous, Anisotropic, Inhomogeneous and Not-Elastic (DIANE) (Harrison and Hudson, 2000). A rock mass is also a fractured porous medium containing fluids, under complex in situ conditions of stresses, temperature and fluid pressures. The complex nature makes rock mass a difficult material for mathematical representation via numerical modelling.

The nature of the rock masses is generally discontinuous. Usually rock masses contain through-going pre-existing fractures, as well as fractures introduced by the excavation process. In rock mechanics the term "fracture" is used to indicate natural breaks in the rock continuum, e.g. faults, joints, bedding planes, fissures. Thus, the term "fracture" is used here as a synonym for "discontinuity".

One of the main tasks of numerical modelling in rock mechanics is to be able to characterize such mechanical discontinuities in a computer model (either explicitly or implicitly). To adequately represent the rock mass in computational models, capturing such fracturing and the complete DIANE nature of the rock mass, it is necessary to be able to include the following features during model conceptualization:

- the relevant physical processes and their mathematical representations by Partial Differential Equations (PDEs);
- the relevant mechanisms and constitutive laws with the associated variables and parameters;
- the pre-existing state of rock stress (the rock mass being already under stress);
- the pre-existing state of temperature and water pressure (the rock mass is porous, fractured, and heated by a natural geothermal heat gradient or man made heat sources);
- the presence of natural fractures (the rock mass is discontinuous);
- variations in properties at different locations (the rock mass is inhomogeneous);
- variations of properties in different directions (the rock mass is anisotropic);
- time/rate-dependent behaviour (the rock mass is not elastic and may undergo creep or plastic deformation);
- variations of properties at different scales (the rock mass is scale-dependent);
- the effects resulting from the engineering perturbations (the geometry is altered).

The extent to which these features can actually be incorporated into a computer model will depend on the physical processes involved and the modelling technique used.

4.2.1 Numerical methods in rock engineering

The most commonly applied numerical methods for rock mechanics problems are:

continuum methods

- the Finite Difference Method (FDM);
- the Finite Element Method (FEM);
- the Boundary Element Method (BEM).

discontinuum methods

- Discrete Element Method (DEM);
- Discrete Fracture Network (DFN) methods.

hybrid continuum/discontinuum models

- Hybrid FEM/BEM;
- Hybrid DEM/DEM;
- Hybrid FEM/DEM, and
- Other hybrid models.

In Appendix A the general formulation of the main methods, typically used in rock mechanics, is described. The possibility to perform a fracture analysis is then outlined for each method.

The choice of *continuum* or *discrete* methods depends mainly on the problem scale and fracture system geometry. Figure 4.1 illustrates the alternative choices for different fracture circumstances in rock mechanics problems.

Continuum approaches should be used for rock masses with no fractures or with many fractures, the behaviour of the latter being established through equivalent properties (Figure 4.1a and 4.1d). The continuum approach can be used if only a few fractures are present and no fracture opening is possible (Fig. 4.1b).

The discrete approach is most suitable for moderately fractured rock masses where large-scale displacements of individual blocks are possible (Fig. 4.1c).

Modelling fractured rocks demands high performance numerical methods and computer codes, especially regarding fracture representations, material heterogeneity and non-linearity, coupling with fluid flow and heat transfer and scale effects. To provide adequate representations for the most significant processes *hybrid* models are often used. In

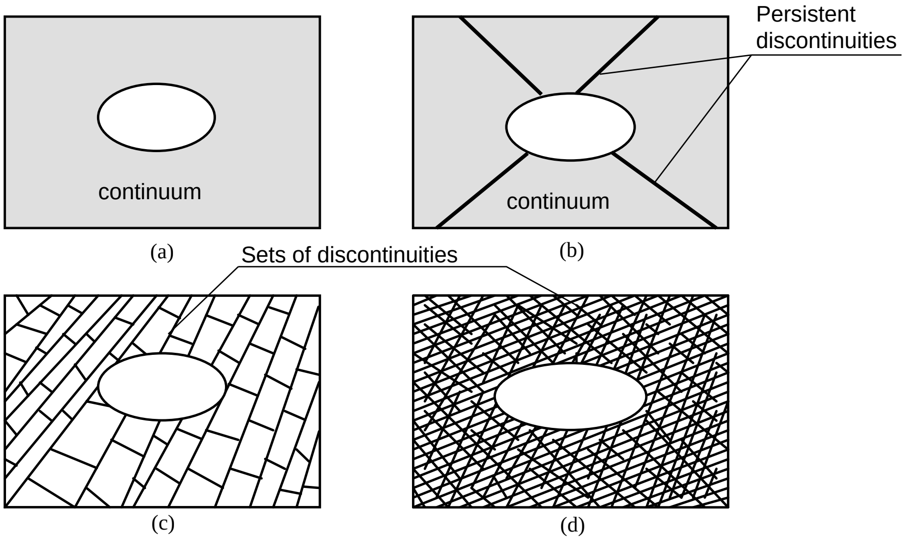

Figure 4.1: Suitability of different numerical methods for an excavation in a rock mass: (a) continuum method; (b) either continuum with fracture elements or discrete method; (c) discrete method; and (d) continuum method with equivalent properties (from Jing, 2003).

the last decade of the 20th century, the *discrete element method* has been coupled with the *finite element method*. The new *hybrid* method was termed the "combined finite-discrete element method" and was proposed by Munjiza (Munjiza et al., 1995). In the review paper of Jing (2003)such a new *hybrid* method has been classified as a DEM.

4.3 The combined finite-discrete element method. History

The *combined finite-discrete element method* was designed with the objective of bridging the gap between methods based on the assumption of *continuum* and methods based on the assumption of *discontinuum*.

The method was first proposed by Munjiza in 1989 and in 1990 the first combined finite-discrete element method code was developed. Since early 1990s some other codes have been developed (Munjiza, 2010) including Elfen, the first commercial code. Elfen was originally a stand alone finite element package. In 1993, Munjiza implemented the combined finite-discrete element routines into Elfen including elaborate contact and fracture solutions. In 1996, Munjiza developed a completely new combined finite-discrete element method code named "Y code", which is open source. The field of applications of the combined finite-discrete element method is ever growing and research groups all over the world have continued the development of the *Y code* so that these days there are at least six versions of the code with different emphasis (Munjiza (2004), Mahabadi et al. (2010)).

4.4 The combined finite-discrete element method

The *combined finite-discrete element method* (FDEM) merges finite element tools and techniques with discrete element algorithms. Finite element-based analysis of continuum is combined with discrete element-based transient dynamics, contact detection and contact interaction solutions.

A typical FDEM problem may contain thousands, even millions of discrete elements which represent each single particle (body) of the domain. Each discrete element has a separate (triangular) finite element mesh. Individual particles can also fracture in addition to being deformable and interacting with each other.

The nature of the deformation of individual discrete elements involves at least finite rotations, whereas finite strains may be involved depending on the material that discrete elements are made of. In addition, material non-linearity including fracture and fragmentation are considered. These processes are in essence processes of transition from continuum to discontinuum, which results in ever-changing geometry of individual discrete elements and/or changing the total number of discrete elements comprising the model.

Transient dynamics of each discrete element, together with the possible state of rest, has to be considered. For instance, in a explosive induced fragmentation, where a detonation gas pushes against the walls of discrete elements causing fracture, the kinetic energy of the system and the velocity of individual discrete element increase. On the contrary, energy dissipation mechanisms such as elastic hysteresis, plastic straining of the material, fracture of the material and friction between discrete elements, eventually lead to the state of rest being reached when all discrete elements have zero kinetic energy.

All these features combined together result in a need for robust CPU and RAM efficient algorithmic solutions. The *combined finite-discrete element method* includes algorithms such as:

- contact interaction algorithms;
- contact detection algorithms;
- finite strain elasticity-plasticity;
- temporal discretization and integration;
- transition from continua to discontinua algorithms;
- coupled problems such as gas-solid interaction;
- application-specific algorithms, visualization, key diagnostics, etc.

4.5 Contact Interaction Algorithm

The combined finite-discrete element method is aimed at problems involving transient dynamics of systems comprising a large number of deformable bodies that interact with each other, and that may in general fracture and fragment, thus increasing the total number of discrete elements. Each individual discrete element has a general shape and size, and is modelled by a single discrete element. Each discrete element is discretised into finite elements to analyse deformability, fracture and fragmentation. A typical combined finite-discrete element system comprises a few thousand to a few million separate interacting solids, each associated with separate finite element meshes. In this context, one of the key issues in the development of the combined finite-discrete element method is the treatment of contact, i.e. the enforcement of the constraint that no point in space is occupied by more than one body at the same time.

From an algorithmic point of view, there are two aspects of contact in the combined finite-discrete element method:

- contact detection;
- contact interaction.

Contact detection is aimed at detecting couples of discrete elements close to each other, i.e. eliminating couples of discrete elements that are far from each other and cannot possibly be in contact. In that sense, contact detection is aimed at reducing CPU requirements, i.e. reducing processing (run) times. Once couples of discrete elements in contact have been detected, a *contact interaction* algorithm is employed to evaluate contact forces between discrete elements in contact. Contact interaction between neighbouring discrete elements occurs through solid surfaces which are in general irregular and, as a consequence, the contact pressure between two solids is actually transferred through a set of points at which surfaces touch.

In the computational literature, theoretical assumptions about contact are simplified by employing *variational formulation of contact* combined with the most simple contact law that defines contact pressure as a function of approach, with tangential resistance to motion being a function of normal pressure or slip condition.

The variational formulation of a boundary value problem with contact is equivalent to the problem of making a functional stationary subject to the contact constraints over boundaries of the domain:

$$\mathbf{C}(\mathbf{u}) = 0 \tag{4.1}$$

Variational formulation of contact problems involves an additional functional due to contact, through which no penetration conditions are enforced.

The *penalty function method*, used in the FDEM, is one of the classic approaches employed in the computational literature, introduced with the aim of eliminationg the drawbacks of the Lagrange multipliers method. To enforce contact constraints on the boundary Γ, the additional functional

$$p \int_{\Gamma} \mathbf{C}^T(\mathbf{u})\mathbf{C}(\mathbf{u})d\Gamma \tag{4.2}$$

is added to the original functional

$$\tilde{\Pi}(\mathbf{u}, \lambda) = \Pi(\mathbf{u}) + p \int_{\Gamma} \mathbf{C}^T(\mathbf{u})\mathbf{C}(\mathbf{u})d\Gamma \tag{4.3}$$

where p is the penalty parameter. As

$$\int_{\Gamma} \mathbf{C}^{T}(\mathbf{u})\mathbf{C}(\mathbf{u})d\Gamma \geq 0 \tag{4.4}$$

if Π is a minimum of the solution, then p must be a positive number. The solution obtained by minimizing the modified functional satisfies the contact constraint only approximately. The larger the value of penalty, the better the contact constraints achieved. Only with an infinite penalty are the contact constraints satisfied exactly.

The *penalty function method* is either used to impose an impenetrability condition in an iterative manner, or to violate this condition in such a way that the correct response of the physical system is still recovered. This is achieved by using a sufficiently large penalty term.

In the finite element method, kinematics of contact is considered by employing slideline algorithms, where one surface is designated as the master (target) surface, while the other is designated as the slave (contactor) surface. Inconsistent contact kinematics produces energy imbalance. An example of this is shown in Figure 4.2. As the potential energy is proportional to δ^2 where δ is penetration, the total amount of kinetic energy transferred into potential energy is proportional to δ_B^2, while the total amount of recovered kinetic energy after contact release is proportional to δ_C^2. As $\delta_C^2 > \delta_B^2$ the final total energy is greater than the initial total energy.

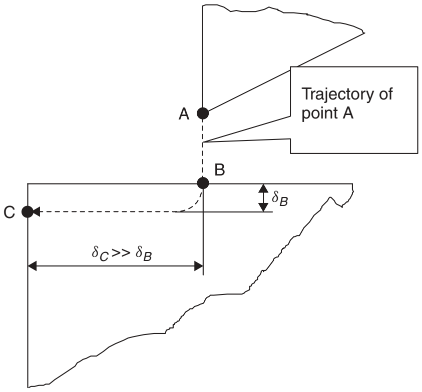

Figure 4.2: Node A penetrates through point B and exits through point C, thus numerically creating energy (from Munjiza, 2004).

Problems of contact interaction in the context of the FDEM are even more important, due to the fact that the problem of contact interaction also defines the "constitutive" behaviour of the system, because of the presence of large numbers of separate bodies. Thus, algorithms employed must pay special attention to contact kinematics in terms of the realistic distribution of contact forces, energy balance and robustness.

The latest generation of contact interaction algorithms makes use of finite element discretizations of discrete elements, and combines this with the so-called potential contact force concept. They also yield realistic distribution of contact forces over finite contact areas resulting from the overlap of discrete elements that are in contact. Thus, numerical distortion of local strain fields close to the boundary due to contact is much reduced - an important aspect when the fracture of brittle material is analysed.

4.5.1 The penalty function method

The *penalty function method* in its classical form assumes that two bodies in contact penetrate each other, and this penetration results in a contact force. The standard contact functional for the penalty function method takes the form

$$\mathbf{U}_c = \int_{\Gamma_c} \frac{1}{2} p(\mathbf{r}_t - \mathbf{r}_c)^T (\mathbf{r}_t - \mathbf{r}_c) d\Gamma \tag{4.5}$$

where p is the **penalty term**, while $\mathbf{r}_t$ and $\mathbf{r}_c$ are position vectors of the points on the overlapping boundaries of the target and contactor bodies, respectively. In the limit for infinite penalty terms, no penetration would occur, i.e.

$$\lim_{p \to \infty} U_c = 0 \tag{4.6}$$

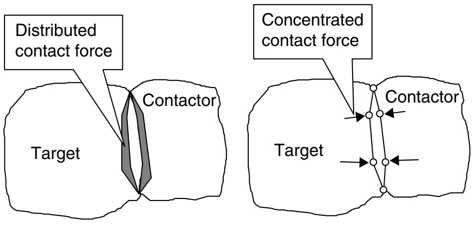

Figure 4.3: Distributed and concentrated contact force approach (from Munjiza, 2004).

However, in practice large penalty terms are coupled with integration problems in the temporal domain, and in practical applications the penalty function method is therefore coupled with overlaps between bodies in contact.

When implemented into actual codes, the penalty function method in general deals with either concentrated or distributed contact force (Figure 4.3). The concentrated contact force approach usually assumes nodal contact forces being a function of penetration of individual contactor nodes into the target, while the distributed contact force is in general evaluated from the shape and size of overlap between the contactor and target.

4.5.2 Potential contact force

The distributed contact force is adopted for two discrete elements in contact, one of which is denoted as the contactor and the other as the target. When in contact, the contactor and target discrete elements overlap each other over area S, bounded by boundary Γ (Figure 4.4).

It is assumed that penetration of any elemental area dA of the contactor into the target results in an infinitesimal contact force, given by

$$d\mathbf{f} = \left[grad\varphi_c\left(P_c\right) - grad\varphi_t\left(P_t\right)\right] dA \tag{4.7}$$

where $d\mathbf{f}$ is the infinitesimal contact force due to infinitesimal overlap dA, defined by overlapping points P_c belonging to the contactor and P_t belonging to the target. Equation A.7 can also be written as

$$d\mathbf{f} = -d\mathbf{f}_t + d\mathbf{f}_c \tag{4.8}$$

where

$$\begin{aligned} d\mathbf{f}_c &= -grad\varphi_t(P_t)dA_c \qquad & dA_c &= dA \\ d\mathbf{f}_t &= -grad\varphi_c(P_c)dA_t \qquad & dA_t &= dA \end{aligned} \tag{4.9}$$

In other words, the contact as described by A.7 can be viewed as first the elemental area of the contactor penetrating the target, and then the elemental area of the target penetrating the contactor.

Thus, for each of the discrete elements in contact, the contact force is calculated as a gradient of the corresponding potential function. The field of contact forces is therefore a conservative field for both the target penetrating contactor and the contactor penetrating target.

Preservation of the energy balance requires that the total energy of the system before and after the contact is the same, i.e. that no work is done by the contact force. Thus, provided that the potentials on the boundary of both the contactor and target discrete elements are constant, the contact force as given by A.7 preserves the energy balance regardless of the geometry or shape of contactor and target discrete elements, the size of the penalty term or the size of penetration (overlap) when in contact. The total contact force is obtained by integration of A.7 over the overlapping area S

$$\mathbf{f}_c = \int_{S=\beta_t \cap \beta_b} \left[grad\varphi_c - grad\varphi_t \right] dA \tag{4.10}$$

which can also be written as an integral over the boundary of the overlapping area Γ

$$\mathbf{f}_c = \oint\limits_{\Gamma_{\beta_t \cap \beta_c}} n_\Gamma \left(\varphi_c - \varphi_t \right) d\Gamma \tag{4.11}$$

where n is the outward unit normal to the boundary of the overlapping area.

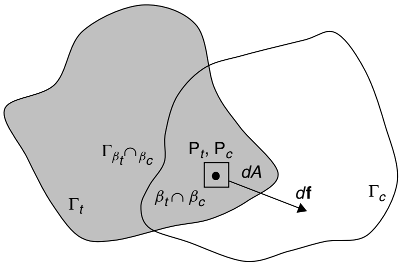

Figure 4.4: Contact force due to an infinitesimal overlap around points P_c and P_t (from Munjiza, 2004).

4.5.3 Discretization of contact force

In the combined finite-discrete element method, individual discrete elements are discretised into finite elements, and each discrete element can be represented as union of its finite elements:

$$\begin{aligned} \beta_c &= \beta_{c1} \cup \beta_{c2} \ldots \cup \beta_{ci} \ldots \cup \beta_{cn} \\ \beta_t &= \beta_{t1} \cup \beta_{t2} \ldots \cup \beta_{ti} \ldots \cup \beta_{tn} \end{aligned} \tag{4.12}$$

where β_c and β_t are the contactor and target discrete elements, respectively, while m and n are the total number of finite elements into which the contactor and target discrete elements are discretised. In this context, the potentials φ_c and φ_t can be written as a sum of potentials associated with individual finite elements:

$$\begin{aligned} \varphi_c &= \varphi_{c1} \cup \varphi_{c2} \ldots \cup \varphi_{ci} \ldots \cup \varphi_{cn} \\ \varphi_t &= \varphi_{t1} \cup \varphi_{t2} \ldots \cup \varphi_{ti} \ldots \cup \varphi_{tn} \end{aligned} \tag{4.13}$$

Integration over overlapping area may therefore be represented by summation over finite elements:

$$\mathbf{f}_c = \sum_{i=1}^{n} \sum_{j=1}^{m} \int_{\beta_{c_i} \cap \beta_{t_j}} \left[grad\varphi_{c_i} - grad\varphi_{t_j} \right] dA \tag{4.14}$$

By replacing integration over finite elements by equivalent integration over finite element boundaries (Equation4.11), the following equation for contact force is obtained:

$$\mathbf{f}_c = \sum_{i=1}^{n} \sum_{j=1}^{m} \int_{\Gamma_{\beta_{ci} \cap \beta_{tj}}} \mathrm{n}_{\Gamma_{\beta_{ci} \cap \beta_{t_j}}} \left(\varphi_{c_i} - \varphi_{t_j} \right) d\Gamma \tag{4.15}$$

where integration over finite element boundaries may be written as summation of integration over the edges of finite elements. In other words, the contact force between overlapping discrete elements is calculated by summation over the edges of corresponding finite elements that overlap.

4.5.4 Contact interaction between two triangular finite elements

As pointed out earlier, combined finite-discrete element problems involve a large number of separate bodies that are free to move and interact with each other. Thus, the evaluation of contact forces at each time step may involve a large number of contacting couples of discrete elements.

In this context, the summation as given by Equation 4.15 usually involves a large number of contacting couples of finite elements, and the total CPU time and overall efficiency of the contact algorithm critically depend upon implementation of part of the interaction that processes finite element to finite element contact.

It is therefore important to employ the simplest possible finite element and make that element work well for both contact and deformability. The simplest possible finite element in 2D is a tri-noded triangle.

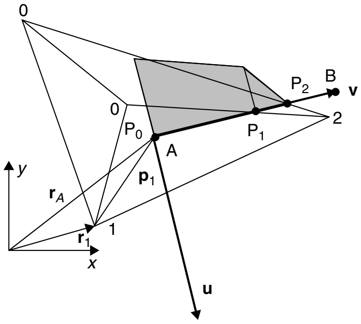

Figure 4.5: Distribution of contact force between the target triangle and an edge of contactor triangle (from Munjiza, 2004).

According to Equation 4.15, the problem of interaction between two triangles can be reduced to interactions between the contactor triangle and the edges of the target triangle, coupled with interactions between the target triangle and the edges of the contactor triangle.

Thus, in Figure 4.5 contact of edge AB of contactor triangle with target triangle is shown. To minimize the number of necessary operations and therefore CPU time to process this contact, a local coordinate system given by local axes **u** and **v** is introduced, and transformation of nodal coordinates of target triangle into local coordinate system is performed:

$$\mathbf{p}_i = \left((\mathbf{r}_i - \mathbf{r}_A) \cdot \mathbf{u}, (\mathbf{r}_i - \mathbf{r}_A) \cdot \mathbf{v} \right) \tag{4.16}$$

The **total contact force** exerted by the target triangle onto the edge AB is given by the area of the diagram of potential over the edge AB, i.e.

$$\mathbf{f}_{c,AB} = \frac{1}{\mathbf{u}^2} \mathbf{u} \int_0^L p \varphi \left(v \right) dv \tag{4.17}$$

where p is the **penalty term**, while the term $\mathbf{u}^2$ comes from the fact that vectors **u** and **v** are not unit vectors. This is computationally convenient as, that evaluation of the integral 4.17 does not involve a square root. In addition, in between the intersection points the potential φ is given by straight lines, which reduces integration to area calculation, as shown in Figure 4.5, where shaded areas represent the potential φ.

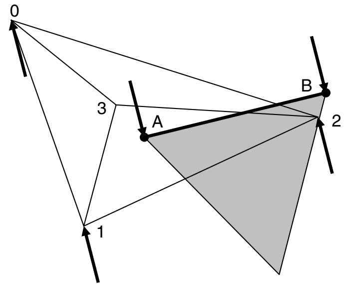

Figure 4.6: Equivalent nodal forces (from Munjiza, 2004).

The contact forces obtained are represented by **equivalent nodal forces at points A and B**, together with corresponding nodal forces at nodes of target triangle, as shown in Figure 4.6.

The whole process is repeated for the remaining edges of the contactor triangle, and in this way, contact forces due to penetration of the contactor triangle into the target triangle are obtained from the potential φ_t as defined for the target triangle. To take into account the contact force due to the potential φ_c associated with the contactor triangle, contact of each edge of the target triangle to the contactor triangle is analysed, and corresponding nodal forces for both the contactor and target triangle are updated. The potential associated with the contactor triangle is defined in exactly the same way as the potential associated with the target triangle, and evaluation of the nodal forces proceeds using the same procedure. The advantages of discretised distributed potential contact force include:

- distributed contact force - no artificial stress concentration due to contact is present; this has important implications when processing the deformability of brittle materials, stress concentrations would result in fracture and non-physical behaviour of the model;

- contact surface - this allows accurate representation of the physical contact conditions onto which friction, sliding, plasticity, surface roughness, wet-dry conditions, etc. can be incorporated following relatively simple rules of potential distribution over the finite element;

- energy preservation - without energy preservation, no proper physical behaviour can be modelled;

- the contact force is discretised with the same algorithm and the same piece of code, regardless of the shape (concave, convex, hollow, etc.) of discrete elements, thus algorithmic complexities are greatly reduced;
- the contact processing is in general faster than alternative solutions; this is due to the contact detection which finds the couples of finite elements that are in contact.

4.5.4.1 Physical interpretation of the penalty parameter

As explained earlier, the maximum allowed penetration is a function of the size of finite elements at the place of contact and **penalty parameter p**, which can be different for different finite elements.

The role of the penalty parameter is best illustrated by an example of contact between two solid finite elements, shown in Figure 4.7. Two elements are pushed against each other by the pressure σ. Relative displacement between points A and B in the case of a small strain elasticity and a zero Poisson's ratio is proportional to the pressure supplied:

$$u = \frac{\sigma h}{E} \tag{4.18}$$

In the same way, the penetration between the two solids is given by

$$d = \frac{\sigma h}{p} \tag{4.19}$$

Thus, to limit penetration, it is enough to select a penalty term to be proportional to the modulus of elasticity, i.e.

$$p = \alpha E \tag{4.20}$$

In this way, contribution of the allowed penetration to the displacement field is limited to

$$d = \frac{1}{\alpha} u \tag{4.21}$$

For $\alpha = 100$, for example,

$$d = \frac{1}{100} u \tag{4.22}$$

i.e. the total local error in displacements will be less than 1%. This is another advantage of the potential contact force approach. The error in the displacements is easily

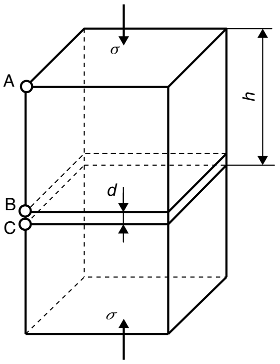

Figure 4.7: Contact between two finite elements (from Munjiza, 2004).

controlled through setting penalty p as a function of E. In addition, the error in displacements is reduced by reducing the size of finite element h. Thus, any mesh refinements automatically reduce error introduced by contact approximation.

4.5.4.2 Contact damping

Any energy dissipation in contact is due to friction or plastic straining of surface asperities. Plastic straining of surface asperities can be approximated by a *viscous damping model*. Damping parameters for contact are defined in a similar way to the definition of penalty parameters. For the situation in Figure 4.7, the frequency of the subsystem shown can be approximated by

$$\omega = \frac{2}{h}\sqrt{\frac{p}{\rho}} \tag{4.23}$$

where ρ is the density and h is the size of the finite element, as shown in the figure. The normal contact stress due to **critical viscous damping** is given by

$$\sigma_c = 2\omega\dot{d} \tag{4.24}$$

while in the general case of an under-damped system,

$$\sigma_c = 2\omega\xi\dot{d} \tag{4.25}$$

where ξ is the damping ratio. If $\xi = 0$, there is no energy dissipation. If $\xi = 1$, critical damping is obtained.
After substituting the frequency from equation 4.24,

$$\sigma_c = 4\xi \frac{\sqrt{p/\rho}}{h} \dot{d} \tag{4.26}$$

This damping is due to contact only. Physical interpretation of such damping is, for instance, plastic deformation or breaking of surface asperities.
This damping is not to be confused with damping such as energy dissipation due to deformation of the discrete elements. Material damping due to elastic or plastic deformation of discrete elements is naturally covered by discrete elements being discretised into finite elements.

Energy balance is especially important when discrete elements are confined so that repeated contact-contact release occurs. When discrete elements are closely packed together, these contact-contact release situations cannot be avoided. If numerical procedures employed were not to preserve the energy balance, the energy of the system would increase artificially. This energy increase is exponential, and results in the combined finite-discrete element system being "blown up", which is another way of saying that the algorithms employed are not stable.

It should be emphasized that the potential contact force contact algorithm has some other features apart from preservation of energy and momentum balance. For instance, due to the discretised nature of the evaluation of contacts, the algorithm is suitable for parallel or distributed computing. There is also an additional advantage from the fact that the geometry is treated in a discretised manner, which greatly reduces the complexity of the algebraic expressions used to evaluate the contact forces.

4.6 Formulation of friction

In the FDEM the friction between two interacting triangles is function of the normal stress σ_n on the triangles edges, i.e.

$$\sigma_t = \mu \sigma_n \tag{4.27}$$

where μ is the friction coefficient. This formulation of friction is called "dynamic friction" and is unsuitable for quasi-static problems. The alternative method which is suitable for quasi-static problems is the Coulomb friction law, implemented in the *contact interaction algorithm*, described in the previous section. The formulation of "quasi static friction" is based on the sliding distance of element edges.
Let's consider the interactions between two triangle, such as the target triangle and the edges of the contactor triangle. The finite increment of the sliding distance is expressed

as

$$\triangle\delta_s = v_{rel}\triangle t \tag{4.28}$$

where v_{rel} is the relative velocity of the two interacting edges and $\triangle t$ the time step size. Then the tangential stress σ_t is calculated using the penalty parameter p and the sliding distance:

$$\sigma_t = \triangle\delta_s p \tag{4.29}$$

If the tangential stress calculated in such a way is greater than the tangential stress calculated with the dynamic formulation (Equation 4.27), i.e. $\sigma_t > \mu\sigma_n$ then the tangential stress and the sliding distance calculated along the edge of the two interacting triangle are adjusted:

$$\begin{cases} \sigma_t = \sigma_t \left| \frac{\mu\sigma_n}{\sigma_t} \right| \\ \Delta\delta_s = \frac{\sigma_t}{p} \end{cases} \tag{4.30}$$

The updated tangential stress is then transformed in equivalent tangential forces and distributed at nodes of the interacting elements in the same way as the normal forces (see Section4.5.3).

4.7 Contact Detection

Large-scale combined finite-discrete element simulations involve contact of a large number of separate bodies, each body being represented by a single discrete element. It is evident that processing of contact interaction involves the summation of contact forces over contacting couples comprising target and contactor elements as explained in Section 4.5.

Thus, processing contact interaction for all possible contacts would involve a total number of operations proportional to N^2, where N is the total number of discrete elements comprising the problem.

This would be very CPU intensive, and would limit application of the combined finite-discrete element method to simulations comprising a very small number (a few thousand) discrete elements. To reduce CPU requirements of processing contact interaction, it is necessary to eliminate couples of discrete elements that are far from each other and are not in contact.

A set of combined finite-discrete element procedures designed to detect discrete or finite elements that are close to each other is usually called a *contact detection algorithm*, or sometimes a contact search algorithm. Examples of linear contact detection algorithms are:

- Munjiza-NBS (No binary search) contact detection algorithm;
- Williams C-grid contact detection algorithm;
- Screening contact detection algorithm.

These algorithms have appeared relatively recently, starting with Munjiza-NBS (1995), which was the first linear contact detection algorithm employed in the combined finite-discrete element method.

4.7.1 Munjiza NBS contact detection algorithm

The algorithm was developed in 1995 by Munjiza, and is called the *Munjiza No Binary Search* (i.e. Munjiza-NBS) contact detection algorithm. The Munjiza-NBS contact detection algorithm assumes a simplified contact detection problem in 2D, i.e. a system comprising N identical discrete elements occupying a finite space of rectangular shape (Figure 4.8), although extensions to non-identical discrete elements are possible.

The task is to find all the discrete element couples that are close to each other in a sense that the distance between their closest points is less than or equal to zero, in other words, that they overlap or touch.

Discrete elements are mapped onto cells. In addition to the mapping of discrete elements onto cells, mapping of discrete elements onto columns and rows of cells is also introduced. A discrete element is said to be mapped to a particular row of cells if it is mapped to any cell from that row. For instance, discrete element 1 is mapped to row 7 of cells, discrete element 2 is mapped to row 8, and discrete element 3 is mapped to row 6 of cells (Figure 4.8). In a similar way, a discrete element is said to be mapped to a particular column of cells if it is mapped to any cell from that column. For instance, discrete element 1 is mapped to the column 4 of cells, discrete element 2 is mapped to column 5 and discrete element 3 is mapped to column 4 of cells (Figure 4.8).

Detection of contact is performed only for cells that have one or more discrete elements mapped to them, i.e. for cells with a non-empty list of discrete elements. This is accomplished by employing a loop over discrete elements. Discrete elements mapped to each such cell are checked for contact against all discrete elements mapped to neighbouring cells, as shown in Figure 4.9.

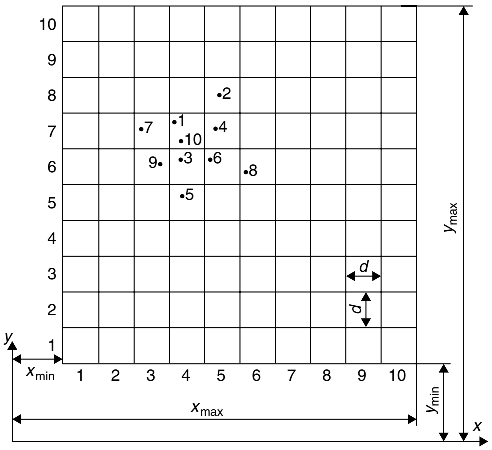

Figure 4.8: Space subdivided into identical square cell of size *d* for the NBS contact detection algorithm (from Munjiza, 2004).

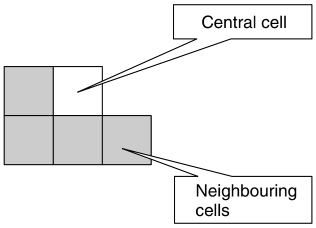

Figure 4.9: Contact checking mask (from Munjiza, 2004).

4.8 Deformability of Discrete Elements

4.8.1 Deformation

Discrete elements were originally introduced to model problems that continuum models cannot model correctly. A large class of problems of discontinua involves individual bodies (discrete elements) that can deform, fail, fracture and even fragment. Such discrete elements are termed "deformable discrete elements". Each discrete element represents a single deformable body, which at any instance of time occupies a region of space.

Special meaning is given to some of these regions; for instance, one such region $\mathscr{B}$ is termed the initial or reference configuration, while $\mathbf{p} \in \mathscr{B}$ are called material points, and bounded sub-regions of the body are called parts. Body deforms via mapping $\mathbf{x} = \mathbf{f}(\mathbf{p})$, where $\mathbf{f}$ is one to one smooth mapping which maps $\mathscr{B}$ onto a closed region $\mathscr{E}$, and which satisfies $\det \nabla \mathbf{f}(\mathbf{p}) > 0$ for any material point $\mathbf{p}$. This condition simply states that no part with non-zero volume can map into zero volume space, i.e. parts of the body occupy space before and after deformation. The volume of such space may defer, but is always greater than zero.

4.8.2 Deformation gradient

Deformation can also be written as $\mathbf{x} = \mathbf{f}(\mathbf{p}) = \mathbf{p} + \mathbf{u}(\mathbf{p})$, where $\mathbf{u}(\mathbf{p})$ is called displacement. Mapping $\mathbf{F}(\mathbf{p}) = \nabla \mathbf{f}(\mathbf{p}) = \mathbf{I} + \nabla \mathbf{u}$ describes change in deformation in the vicinity of each material point, and is referred to as the deformation gradient.

4.8.2.1 Frames of reference

To describe the deformation of a particular discrete element in the vicinity of the material point $\mathbf{p}$, four reference frames are used (Figure 4.10):

- *Global frame* $(\mathbf{i}, \mathbf{j}, \mathbf{k})$.
- *Local frame* $(\bar{\mathbf{i}}, \bar{\mathbf{j}}, \bar{\mathbf{k}})$. It is associated with the initial position of a particular discrete element.
- *Deformed local frame* $(\tilde{\mathbf{i}}, \tilde{\mathbf{j}}, \tilde{\mathbf{k}})$. This frame is fixed to the material point $\mathbf{p}$ of the discrete element and moves with that point.
- *Initial frame* $(\hat{\mathbf{i}}, \hat{\mathbf{j}}, \hat{\mathbf{k}})$. It is linked to the material point $\mathbf{p}$ and is associated with the initial position of a particular discrete element.

- *Deformed initial frame*: $(\check{\mathbf{i}}, \check{\mathbf{j}}, \check{\mathbf{k}})$. This frame is fixed to the material point $\mathbf{p}$ of the discrete element, and moves with that point.

The *global*, *local* and *initial* frames are inertial frames, while the *deformed local frame* and *deformed initial frame* are non-inertial frames. The relationship between a *local* and *deformed local frame* can be obtained using the deformation gradient.

The physical meaning of the deformation gradient can be explained by taking an infinitesimal material element in the vicinity of point $\mathbf{p}$, as shown in Figure 4.11. It is assumed that this material element coincides with a cube of edge of unit length. By choosing a very small unit for the length, the edge of the cube is made infinitesimally small.

Because the unit for length is conveniently chosen to be infinitesimally small, the base vectors of the local triad coincide with the edges of the material element. As the material in the vicinity of point $\mathbf{p}$ deforms, these base vectors are mapped through deformation into corresponding base vectors of the deformed local triad:

$$\tilde{\mathbf{i}} = \left(1 + \frac{\partial \bar{u}}{\partial \bar{x}}\right) \bar{\mathbf{i}} + \frac{\partial \bar{v}}{\partial \bar{x}} \bar{\mathbf{j}} + \frac{\partial \bar{w}}{\partial \bar{x}} \bar{\mathbf{k}} \tag{4.31}$$

$$\tilde{\mathbf{j}} = \frac{\partial \bar{u}}{\partial \bar{x}} \bar{\mathbf{i}} + \left(1 + \frac{\partial \bar{v}}{\partial \bar{x}}\right) \bar{\mathbf{j}} + \frac{\partial \bar{w}}{\partial \bar{x}} \bar{\mathbf{k}} \tag{4.32}$$

$$\tilde{\mathbf{k}} = \frac{\partial \bar{u}}{\partial \bar{x}} \bar{\mathbf{i}} + \frac{\partial \bar{v}}{\partial \bar{x}} \bar{\mathbf{j}} + \left(\frac{1 + \partial \bar{w}}{\partial \bar{x}}\right) \bar{\mathbf{k}} \tag{4.33}$$

As can be seen from Figure 4.11, these vectors are in general non-orthogonal to each other. In addition, these vectors are not unit vectors. Thus, a cube shaped material element of unit volume changes both its volume and it original cubic shape.

Special types of deformation include the deformation with constant displacement $\mathbf{u}(\mathbf{p}) = const$ and deformation with constant deformation gradient $\mathbf{F}(\mathbf{p}) = const$. The deformation with constant displacement is referred to as *translation*. In this type of deformation, the initial material element is identical in shape, size and orientation to the deformed initial volume, except that it is translated. Translation therefore does not produce any straining of the material. The deformation with constant deformation gradient is referred to as *homogeneous*.

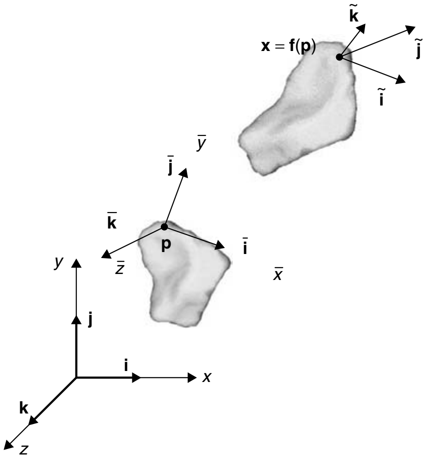

Figure 4.10: Frames of reference (from Munjiza, 2004).

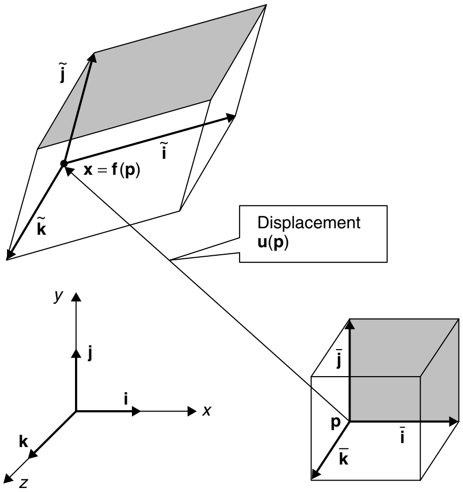

Figure 4.11: Physical meaning of deformation gradient (from Munjiza, 2004).

4.8.3 Homogeneous deformation

Homogeneous deformation can be expressed as a composition of *rotation* **g** and *stretch* **s**:

$$\mathbf{f}(\mathbf{p}) = \mathbf{g} \circ \mathbf{s}_1 = \mathbf{s}_2 \circ \mathbf{g} \tag{4.34}$$

The deformation gradient for homogeneous deformation is therefore given by

$$\mathbf{F} = \mathbf{RU} = \mathbf{VR} \tag{4.35}$$

where $\mathbf{R} = \nabla \mathbf{g}$, $\mathbf{U} = \nabla \mathbf{s}_1$and $\mathbf{V} = \nabla \mathbf{s}_2$.
It is worth mentioning that by definition of homogeneous deformation tensors **F**, **R** and **U** are constant tensors, i.e. they do not change from point to point (over the spatial domain). Tensor **U** is called the right stretch tensor. Tensor **V** is called the left stretch tensor. Tensors **U** and **V** are symmetric and positive definite tensors with

$$\det \mathbf{U} = \det \mathbf{V} = |\det \mathbf{F}| > 0 \tag{4.36}$$

representing the ratio between the volume of the deformed material element and the initial material element. Both right and left stretch tensors can be decomposed into a succession of three extensions in three mutually orthogonal directions:

Right stretch tensor

$$\mathbf{U} = \sum_{i=1}^{3} \lambda_i \bar{\mathbf{e}}_i \otimes \bar{\mathbf{e}}_i = \mathbf{I} + (s_i - 1)\bar{\mathbf{e}}_i \otimes \bar{\mathbf{e}}_i \tag{4.37}$$

Left stretch tensor

$$\mathbf{V} = \sum_{i=1}^{3} \lambda_i \bar{\mathbf{e}}_i \otimes \bar{\mathbf{e}}_i = \mathbf{I} + (s_i - 1)\bar{\mathbf{e}}_i \otimes \bar{\mathbf{e}}_i \tag{4.38}$$

where scalars s_1, s_2 and s_3 represent principal stretches. Principal stretches are in essence elongation in the principal directions, i.e. the ratio between the deformed length and initial length. Principal stretches are the same for both right and left stretch tensor. The right stretch tensor **U** therefore represents successive stretching of the material element in three mutually orthogonal directions. This stretching is applied before any rotation. In contrast, left stretch tensor **V** represents successive stretching of the material element in three mutually orthogonal directions applied after rotation. Thus, the principal directions of left stretch tensor **V** are obtained by simply rotating the principal directions associated with the right stretch tensor **U**.

4.8.4 Strain

Using stretch tensors **U** and **V**, different strain tensors can be defined. For instance,

$$\begin{aligned} \mathbf{C} &= \mathbf{F}^T\mathbf{F} = (\mathbf{RU})^T(\mathbf{RU}) = \mathbf{U}^T\mathbf{R}^T\mathbf{RU} = \mathbf{U}^T\mathbf{U} \\ \mathbf{B} &= \mathbf{FF}^T = (\mathbf{VR})(\mathbf{VR})^T = \mathbf{VRR}^T\mathbf{V}^T = \mathbf{VV}^T = \mathbf{V}^2 \end{aligned} \tag{4.39}$$

are the **right** and **left Cauchy-Green strain tensor**, respectively. In the case of the right Cauchy-Green strain tensor **C**, rotation occurs after stretch. Thus, the left Cauchy-Green strain tensor is best represented using a *local frame*, i.e. using configuration before any rotation has taken place. In the case of the left Cauchy-Green strain tensor **B**, stretch occurs after rotation. Thus, the left Cauchy-Green strain tensor is best represented using a *deformed local frame*, i.e. using configuration after the rotation has taken place.

4.8.5 Stress - Cauchy stress tensor

Cauchy's theorem makes it possible for integral relations of momentum balance to be replaced by partial differential equations.

The necessary and sufficient condition for the momentum balance law to be satisfied is the existence of a spatial tensor field **T** (also called Cauchy stress) such that:

- for a vector **m**, the surface traction force is given by $\mathbf{s}(\mathbf{m}) = \mathbf{Tm}$;
- **T** is symmetric and positive, i.e. for any vector **a**, $\mathbf{a} \cdot \mathbf{Ta} > 0$ unless $\mathbf{a} = 0$;
- **T** satisfies the equation of motion $div\mathbf{T} + \mathbf{b} = \rho\dot{\mathbf{v}}$;

where **s** is the traction force corresponding to the surface of deformed configuration, **b** is the body force per unit volume of the deformed configuration, ρ is the density measured per unit volume of the deformed configuration, and **m** is the normal to the boundary of deformed configuration.

The Cauchy stress tensor in essence represents a linear mapping where a given outward surface normal **m** is mapped onto a total surface traction force **s**. The surface normal **m** is of magnitude equal to the surface area it represents. Thus, for instance, if the magnitude of **m** is doubled, the total surface traction is doubled. This is easily understood, for doubling the normal **m** is equivalent to doubling the surface area.

The matrix of Cauchy stress tensor in the *global frame* $(\mathbf{i}, \mathbf{j}, \mathbf{k})$ is given by

$$\mathbf{T} = \begin{bmatrix} t_{xx} & t_{xy} & t_{xz} \\ t_{yx} & t_{yy} & t_{yz} \\ t_{zx} & t_{zy} & t_{zz} \end{bmatrix} \tag{4.40}$$

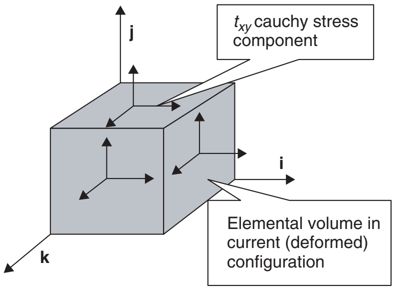

Figure 4.12: Cauchy stress tensor components in deformed configuration. Note that the material element is taken in the directions of the global base vectors (from Munjiza, 2004).

where the first index indicates the direction of the stress component (direction of traction force) and the second index denotes the corresponding surface normal. Thus, t_{xy} is the traction force in the x-direction on the surface "in the y-direction", i.e. force $t_{xy}\mathbf{i}$ on the surface $1\mathbf{j}$.

Cauchy stress refers to the force per unit area of the deformed configuration. Components of Cauchy stress tensor are shown in Figure 4.12.

4.8.6 Constitutive Law

For an elastic body a constitutive law (physical equations) can be written as

$$\mathbf{T}(\mathbf{x}) = \hat{\mathbf{T}}(\mathbf{F}(\mathbf{p}), \mathbf{p}) \tag{4.41}$$

where $\mathbf{T}$ is Cauchy stress tensor, $\mathbf{x}$ represents deformed configuration and $\mathbf{p}$ represents initial configuration. A necessary and sufficient condition that the response is independent of the observer is that

$$\mathbf{R}\hat{\mathbf{T}}(\mathbf{F}(\mathbf{p}), \mathbf{p})\mathbf{R}^T = \hat{\mathbf{T}}(\mathbf{R}\mathbf{F}(\mathbf{p}), \mathbf{p}) \tag{4.42}$$

i.e. if rotation $\mathbf{R}$ is applied to the elastic body, the stress should not change. Actually, this rotation could also be viewed as rotation of the global triad. Rotation of an elastic body is equivalent to the rotation of the global coordinate system in the opposite direction by

$$\mathbf{R}^{-1} = \mathbf{R}^T$$

The body is called isotropic if

$$\hat{\mathbf{T}}(\mathbf{F}(\mathbf{p}), \mathbf{p}) = \hat{\mathbf{T}}(\mathbf{F}(\mathbf{p})\mathbf{R}, \mathbf{p}) \tag{4.43}$$

Many materials cannot undergo large (finite) strains, and often it is the case that only small strains are possible before fracture or failure occurs. In addition, in many problems of practical engineering importance the deformation gradients are also small, resulting in the deformed configuration being almost identical to the initial configuration.

The first case is the case of small strains, and the second case is the case of small displacements. In the case of small strains and small displacements, a suitable strain tensor is the so-called infinitesimal strain:

$$\mathbf{E} = \frac{1}{2}\left(\nabla\mathbf{u} + \nabla\mathbf{u}^T\right) \tag{4.44}$$

In the combined finite-discrete element method, the strain may be small in most problems of practical importance. However, the displacements are almost never small, thus Equation 4.44 does not apply. Small strains only imply small stretches, while rotations and displacements are large. In such a case of small strains and large rotations, the deformation gradient can be decomposed into a stretch followed by rotation

$$\mathbf{F} = \mathbf{R}\mathbf{U} \tag{4.45}$$

Stretch **U** is a result of displacements **u**, i.e.

$$\mathbf{U} = \mathbf{I} + \nabla\mathbf{u} \tag{4.46}$$

Also,

$$\mathbf{C} = \mathbf{F}^T\mathbf{F} = \mathbf{U}^2 \tag{4.47}$$

where

$$\mathbf{U}^2 = \begin{bmatrix} 1 + 2\frac{\partial u}{\partial x} & \frac{\partial u}{\partial y} + \frac{\partial v}{\partial x} & \frac{\partial u}{\partial z} + \frac{\partial w}{\partial x} \\ \frac{\partial u}{\partial y} + \frac{\partial v}{\partial x} & 1 + 2\frac{\partial v}{\partial y} & \frac{\partial v}{\partial z} + \frac{\partial w}{\partial y} \\ \frac{\partial u}{\partial z} + \frac{\partial w}{\partial x} & \frac{\partial v}{\partial z} + \frac{\partial w}{\partial y} & 1 + 2\frac{\partial w}{\partial z} \end{bmatrix} \tag{4.48}$$

after neglecting higher order terms yields. This means that the *small strain tensor* can be approximated by

$$\mathbf{E} = \frac{1}{2}(\mathbf{U}^2 - \mathbf{I}) \tag{4.49}$$

In other words, if the strains are small, a small strain tensor (engineering strain) is obtained using the formula

$$\bar{\mathbf{E}} = \frac{1}{2}(\mathbf{F}^T\mathbf{F} - \mathbf{I}) = \frac{1}{2}[(\mathbf{R}\mathbf{U})^T(\mathbf{R}\mathbf{U}) - \mathbf{I}] = \frac{1}{2}(\mathbf{U}^T\mathbf{U} - \mathbf{I}) \tag{4.50}$$

This strain tensor is called a **right Green-St.Venant strain tensor**. It is worth mentioning that although strains are small, rotations in the combined finite-discrete element method are always finite.
With the right stretch tensor **U** a material is first stretched in the principal directions. This is followed by rotation. Thus, the right small strain tensor corresponds to the initial configuration in a sense that strain components expressed using a global triad are correct when applied to the initial configuration.

An equivalent small strain tensor is obtained using the left stretch tensor **V**:

$$\tilde{\mathbf{E}} = \frac{1}{2}(\mathbf{F}\mathbf{F}^{\mathbf{T}} - \mathbf{I}) = \frac{1}{2}[(\mathbf{V}\mathbf{R})(\mathbf{V}\mathbf{R})^{T} - \mathbf{I}] = \frac{1}{2}(\mathbf{V}\mathbf{V}^{\mathbf{T}} - \mathbf{I}) \tag{4.51}$$

This strain tensor is called the **left Green-St.Venant strain tensor**. The left stretch tensor is defined in such a way that rotation occurs before stretching, i.e. stretching in three principal directions occurs on the rotated configuration. As rotation in the combined finite-discrete element method is always finite regardless of the strains, the strain tensor defined by Equation 4.51 is generally different from the strain tensor obtained using Equation 4.50. The right Green-St.Venant strain tensor refers to the initial configuration. The left Green-St.Venant strain tensor refers to the deformed (current) configuration.

Since strains are small, to obtain stresses from strains a small strain elasticity constitutive law can be employed. For homogeneous isotropic material the stress-strain relationship is given by Hooke's law.

4.9 Temporal discretization

4.9.1 The central difference time integration scheme

Contact between discrete elements together with the deformability of discrete elements is described in terms of nodal forces and nodal displacements. Since each discrete element is discretised into finite elements, the shape of each discrete element and its position in space at any time instance is given by the *current coordinates* of the finite element nodes, i.e. nodal coordinates.

In a similar way, the velocity field over the discrete element is defined by nodal velocities **v;** the acceleration field **a** over the discrete element is given by $\mathbf{a} = \dot{\mathbf{v}} = \ddot{\mathbf{x}}$ with $x = \begin{bmatrix} x_1, & x_2, & x_3, & ..., & x_i, & ..., & x_n \end{bmatrix}$ where n is the total number of degrees of freedom for a particular discrete element. The inertia of the discrete element is defined by the mass of the discrete element, which is obtained by integration of density over the volume of the discrete element, i.e.

$$dm = \rho dV \tag{4.52}$$

Discretization of the discrete element into finite elements also results in discretization of the mass. The most convenient way of discretization of the mass used in the FDEM is a so-called **lumped mass approach**. In essence, instead of considering the mass being distributed over the discrete element, it is assumed that the mass is lumped into the nodes of the finite element mesh. It is worth noting that in the finite element literature, discretization of mass is done through the mass matrix, which is in general non-diagonal. However, elimination of non-diagonal terms leads to a diagonal lumped mass matrix where all non-diagonal terms are zero. This approach, in conjunction with the stiffness matrix for dynamic problems, is suitable for both implicit and explicit direct integration in the time domain.

In the context of the combined finite-discrete element method, deformability together with rigid rotation and translation is considered, and contact interaction is resolved together with fracture and fragmentation. Assembling a stiffness matrix and a non-diagonal mass matrix would lead nowhere, for any available implicit time integration scheme could not be used without significant modifications. Thus, no stiffness matrices are calculated. A time integration scheme is applied on element-by-element, node-by-node and degree of freedom by degree of freedom bases in an explicit form. Nodal forces from contact interaction, deformation of a discrete element, external loads, and damping forces (due to either "external" damping or "internal" damping) are all added together, and a vector $\mathbf{f}$ of nodal forces is obtained. The dynamic equilibrium of the discrete element is therefore given by $\mathbf{f} = \mathbf{ma}$. The mass matrix $\mathbf{m}$ may be constant when no fracture occurs.

For integration of the above equations, the central difference time integration scheme has been traditionally employed. It is an explicit scheme resulting in no need for stiffness matrices to be assembled or stored. In addition, it is conditionally stable, meaning that the stability of the scheme is achieved through reducing the size of the time step. The accuracy of the scheme is also controlled by the size of the time step.

The essence of the **central difference time integration scheme** is the explicit integration of the governing equation for each degree of freedom separately. In the case of the constant time step, formulation of the central difference time integration scheme is given as follows:

$$\begin{aligned} v_{next} &= v_{current} + a_{current}h \\ x_{next} &= x_{current} + v_{next}h \end{aligned} \tag{4.53}$$

where

$$a_{current} = \frac{f_{current}}{m} \tag{4.54}$$

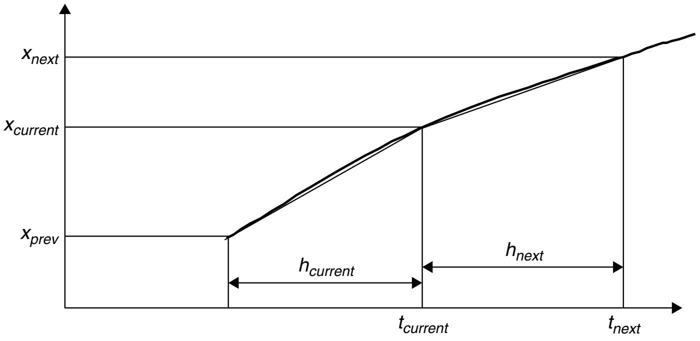

Figure 4.13: The central difference time integration scheme (from Munjiza, 2004).

is the sum of body forces, contact forces and external loads, together with any damping forces (friction, viscous drag, material viscous damping), and m is the mass associated with the particular degree of freedom. A graphical interpretation of the central difference time integration scheme is given in Figure 4.13.

4.9.1.1 The combined finite-discrete element simulation of the state of rest

Many combined finite-discrete element problems include transient motion that leads to the state of rest. Through energy dissipation mechanisms such as fracture, friction and permanent deformations, the energy of the combined finite-discrete element system is steadily reduced until all the discrete elements are virtually at a state of rest.

In the FDEM, the state of rest and static cases in general are treated as special cases of transient dynamics problems, where energy dissipation mechanisms are such that in a relatively short time a state of rest is achieved or the load is applied at a such a slow rate that no dynamic effects are induced. The method is called *dynamic relaxation*.

In *dynamic relaxation* the static system is replaced by an equivalent transient dynamic system

$$\mathbf{K}\mathbf{x} + \mathbf{M}\ddot{\mathbf{x}} + \mathbf{C}\dot{\mathbf{x}} = \mathbf{p} \tag{4.55}$$

where $\mathbf{K}$ is the stiffness matrix, $\mathbf{M}$ is the mass matrix and $\mathbf{C}$ is the damping matrix. The *dynamic relaxation* is said to converge if the steady state solution of the equivalent dynamic system is identical to the static solution. The most important advantage of *dynamic* *relaxation* in comparison to iterative methods in general is probably the physical meaning, which can be attached to the convergence process itself through gradual motion of the system toward the steady state, which can be expressed in terms of inertia forces. This is very useful in problems with slow monotonic loading and non-linear problems, in which non-unique solutions may exist. However, the path through which a steady state is reached and the speed at which it is reached are heavily dependent on both the **C** and **M** matrices.

4.10 Transition from Continua to Discontinua algorithm

Transition from continua to discontinua occurs through fracture and fragmentation processes. Generally, fracture occurs through alteration, damage, yielding or failure of micro-structural elements of the material.

To describe this complex, material dependent phenomenon, the alteration of stress and strain fields due to the presence of micro structural defects and stress concentrations must be taken into account. Several approaches are available: global approaches, local approaches, smeared crack models and single crack models.

Global approaches to fracture are based on the representation of the singularity of the stress field at the crack tip. It was shown by Griffith that the failure of a brittle elastic medium due to such singularity can be characterised by the energy release rate G. The critical value of $G = 2\gamma$ (where γ represents the surface energy) is a material characteristic. The alternative formulation of the Griffith method is achieved through stress intensity factors, which characterize the stress singularity on a semi-local basis in terms of force, while the same singularity is characterised in terms of energy by contour integrals.

Local approaches to crack analysis usually employ a smeared crack approach, with a single crack being replaced by a blunt crack band. This approach has been justified by the fact that engineering materials show a reduction in the load-carrying capacity accompanied by strain localization after the maximum load-carrying capacity is reached.

Beyond the peak load (when the material gradually disintegrates), two types of failure mechanism are observed, namely *decohesion* and *frictional slip*. In the first type of failure fracture, zones are observed (cracks), while in the latter failure zones propagate along shear bands (faults).

Smeared crack models attempt to describe these processes through constitutive laws, such as a strain softening constitutive law or damage mechanics based formulation. However, standard continuum mechanics formulations incorporating softening fail, as the underlying mathematical problem becomes ill-posed. As a result, the numerical solution predicts a vanishing energy dissipation upon spatial discretization refinement. A mathematically well-posed problem is obtained by using an enriched continuum formulation (such as a Micro-polar Cosserat) or higher-order constitutive law (such as a non-local constitutive law, where the higher order gradients of the deformation field are included in the formulation). A relatively straightforward alternative utilizing a fracture energy based softening plasticity framework has also been successfully adopted in the past, where a mesh size dependent softening modulus ensures objective energy dissipation.

The local approaches to crack analysis based on a single crack concept are usually based on the Dugdale model or Barenblatt model. The Dugdale model is a relatively simple non-linear model for a crack with a plastic zone at its tip, where the zone of plastically strained material is replaced by a zone of weakened bonds between the crack walls. As the crack walls separate the bond stress reaches maximum. At the point when the separation reaches a critical value, the bonding stress drops to zero.

The main tasks in describing fracture in the combined finite-discrete element method are to predict crack initiation, predict crack propagation, perform the necessary remeshing, transfer variables from the old to the new mesh and replace the released internal forces with equivalent contact forces. Robustness, accuracy, simplicity and CPU requirements of the fracture algorithms implemented are of major importance, and both single and smeared crack models have been employed in the past.

4.10.1 Strain softening based smeared fracture model

In experimental tests of rock and rock-like materials, a gradual load decrease with an increase in displacements is observed. The phenomenon occurs under uniaxial tension as well as under uniaxial compression and triaxial stress states.

Figure 4.14 shows a typical stress-displacement diagram for a rock specimen under uniaxial tension. Due to stress decreasing with increasing strain, pre-failure strains are highly localized in a narrow band, which eventually results in a discontinuity in the form of a crack. The phenomenon of decreasing stress in a localization band area with increasing strains is called “strain-softening”.

Localization is the intense straining of a material within thin bands. The strains for real engineering softening materials such as rock, are localized over a relatively small (far smaller than the size of the actual physical or engineering problem) yet finite lengths (characteristic lengths) that reflect the micro-structure of the rock, and energy dissipation is therefore well defined.

Actual implementation of strain softening material models into finite element codes has been associated with great difficulties regarding both sensitivity to mesh size and mesh orientation. The localization zone width corresponds to the element size, and with

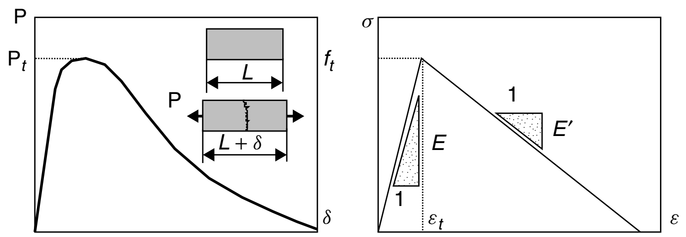

Figure 4.14: A typical stress-displacement diagram for rock under uniaxial tension and idealized stress-strain diagram in the localization zone (from Munjiza, 2004).

a finer mesh the localization zone width is smaller and, in addition, localization zones tend to follow preferred directions (along the finite element edges or diagonals) dictated by the mesh.

Localization is closely related to smeared crack models, where the localization zone (crack band) is usually assumed to propagate into the next finite element when the stress in that element reaches a strength limit. In this way, the propagation of the zone is influenced and largely determined by the zone width, because the narrower the zone the larger the stresses ahead.

The *smeared fracture model* implemented in the FDEM also uses the concept of localization band propagation. The underlying assumptions of the model are:

- the localization (tensile fracture) occurs on the finite element integration point level;
- the size of the overall model is significantly larger than the size of the finite elements employed (h);
- the strain energy accumulated before the peak stress is reached within an area associated with the integration point undergoing softening can be neglected;
- the plasticity model is assumed to be isotropic, i.e. the accumulated effective plastic strain is monitored in the principal directions only. If, after the strength limit is reached, a full breakage does not occur (stress state on the softening branch), the effective plastic strain is treated as a scalar state variable for the next state of deformation, which will be valid for any new rotated principal direction.

To deal with mesh size sensitivity, the local softening material law is formulated in terms of the **fracture energy release rate in tension**, $\mathbf{G_f}$, and the local control length h:

$$h = \sqrt{\frac{4A}{\pi}} \tag{4.56}$$

where A is the area associated with the Gauss integration point considered. To avoid limitations to the upper limit of the element size to be used, which arises from the difficulties in numerically capturing the so-called snap back in the constitutive law (softening slope return), the fracture energy is assumed to control only the post-peak behaviour, i.e. after the peak stress f_t is reached. The local softening slope for each Gauss-point is then obtained from the energy balance

$$\frac{f_t^2}{2E'}A = 2\gamma h = G_f h \tag{4.57}$$

This modification of the constitutive law resolves the problem of sensitivity of the fracture energy release rate to the mesh size. However, the sensitivity of crack initiation to element size remains. This is because the crack is replaced by a localization band which is equal to the element size. A further consequence of this is also the sensitivity to mesh orientation. With a deformable discrete element, discretised into finite elements, a critical state of stress (or strain) is reached when an element separates into two or more discrete elements, or a discrete element changes its boundary (if the failure is only partial). At the stage when the strength of material in some Gauss-points is reduced to zero, a crack is assumed to open. The direction of the crack coincides with the direction of the greater principal plastic stretch. A re-meshing of finite elements within every discrete element is therefore performed, and when breakage occurs new boundaries are created.

4.10.2 Discrete crack model

As explained above, the *smeared crack model* for fracture and fragmentation is coupled with numerical difficulties and algorithmic complexities. Recent research efforts regarding fracture modelling in the context of the combined finite-discrete element method have therefore also included the single crack model.

The model presented in this section is actually a *combination of the smeared and single crack approaches*. It was designed with the aim of modelling multiple-crack situations, progressive fracture and failure, including fragmentation and the creation of a large number of rock fragments of general shape and size. It is aimed at mode I loaded cracks only and based on the approximation of stress-strain curves for rock in direct tension (Figure 4.15).

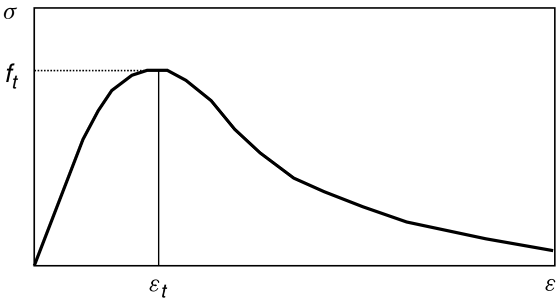

Figure 4.15: Typical strain softening curve defined in terms of strains (from Munjiza, 2004).

A typical stress-strain curve for rock consists of the hardening branch (before the peak stress is reached) and strain-softening part, which represents decreasing stress with increasing strain. The strain-hardening part of the stress-strain curve presents no difficulties when implemented in the combined finite-discrete element method, and is therefore implemented in a standard way through the constitutive law. The strain-softening part of the stress-strain curve is connected with localization of strains, loss of ellipticity (hyperbolicity) of the governing equation, ill-posed problems and general sensitivity to mesh size and mesh orientation. To deal with these problems, formulation of the strain softening by means of stress and displacements is adopted, as shown in Figure 4.16.

The area under the stress-displacement curve represents the **energy release rate**, $G_f = 2\gamma$, where γ is the surface energy, i.e. the energy needed to extend the crack surface by unit area. The softening stress-displacement relationship is implemented in the FDEM through the single crack model, i.e. using bonding stress, as shown in Figure 4.17.

In theory, the separation $\delta = \delta_t = 0$ coincides with the bonding stress being equal to the tensile strength f_t , i.e. no separation occurs before the tensile strength is reached.

With increasing separation $\delta > \delta_t$ the bonding stress decreases, and at separation $\delta = \delta_c$ the bonding stress drops to zero. Bonding stress for separation $\delta_t < \delta < \delta_c$ is given by

$$\sigma = z f_t \tag{4.58}$$

i.e. a scaled tensile strength, with the scaling (softening) function z being defined in such a way that it represents a close approximation of the stress-displacement curve. Thus, a

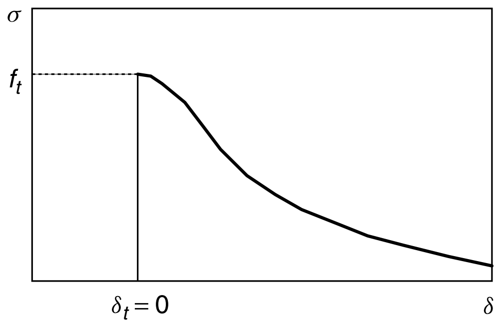

Figure 4.16: Strain softening defined in terms of displacements (from Munjiza, 2004).

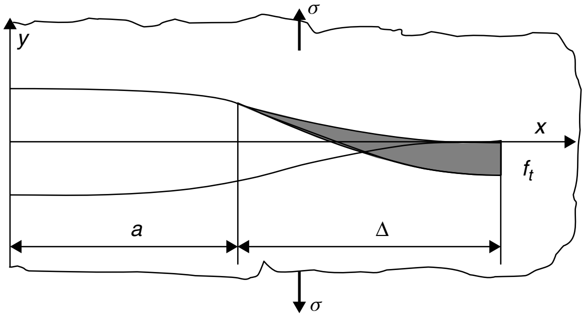

Figure 4.17: Single crack model with bonding stress (from Munjiza, 2004).

heuristic formula for z is adopted:

$$z = \left[1 - \frac{a+b-1}{a+b}\exp\left(D\frac{a+cb}{(a+b)(1-a-b)}\right)\right]\left[a(1-D)+b(1-D)^{c}\right] \tag{4.59}$$

where the variable D is given by

$$D = \begin{cases} 0 & \text{if} \quad \delta \leq \delta_t \\ 1 & \text{if} \quad \delta > \delta_c \\ \frac{\delta-\delta_t}{\delta_c-\delta_t} & \text{otherwise} \end{cases} \tag{4.60}$$

while the parameters a, b and c are obtained from experimental stress-displacement curves by curve fitting.
Note that for any value of these parameters, the above heuristic formula results in a bonding stress of f_t for $D = 0$ and a bonding stress equal to zero for $D = 1$. The tangent at the stress displacement curve at $D = 0$ is horizontal. Thus, parameters a, b and c control the slope of the curve at $D = 1$ and the shape of the curve (curvature) at $D = 0$ together, with the inflection point.

In the discrete crack model, it is assumed that the crack walls coincide with the finite element edges. Thus initially the total number of nodes for each of the finite element meshes (every single discrete element is associated with its separate finite element mesh) is doubled, and nodes are held together through a penalty function method.

Thus the separation δ_t is a function of the penalty term p employed. In the limit no separation of adjacent edges takes place before stress f_t is reached, i.e.

$$\lim_{p\to\infty} \delta_t = 0 \tag{4.61}$$

With increasing separation $\delta > \delta_t$ the bonding stress decreases, and at separation $\delta > \delta_c$ it is zero and the crack is assumed to propagate.

In finite element discretization of the governing equations, only approximate stress and strain fields close to the crack tip are obtained. With the bonding stress model as described above, the stress and strain fields close to the crack tip are influenced by the magnitude and distribution of the bonding stress close to the crack tip.

For the bonding stress to have a significant effect on stress distribution results, it is necessary that the size of finite elements close to the crack tip be smaller than the actual size of the plastic zone. The coarser mesh results in bonding stress in all elements close to the crack walls being reduced to zero, except for the few elements adjoining the crack tip. The propagation of the crack is therefore influenced by the orientation of those elements close to the crack tip. The coarse finite element mesh does not accurately represent the stress field in the proximity of the crack tip, and as a result, the stress field obtained is influenced by the mesh topology close to the crack tip. i.e. the de-bonding and separation of crack walls occurs on an element-by-element basis. One way to avoid this problem is to have an element size close to the crack tip much smaller than the size of the plastic zone. Sensitivity to mesh size and orientation is due to the singularity of the stress field at the crack tip. The influence of such singularity can be illustrated on the example of the following function:

$$\sigma = \frac{1}{\sqrt{x}} \tag{4.62}$$

being approximated by constant value finite elements, as shown in Figure 4.18. The relative error of such an approximation can be estimated by

$$\varepsilon = \frac{\frac{1}{\sqrt{(n-1)h}} - \frac{1}{\sqrt{nh}}}{\frac{1}{\sqrt{(n-1)h}}} 100\% = \left(1 - \sqrt{\frac{n-1}{n}}\right) 100\% \tag{4.63}$$

It is evident that the relative error of approximation does not decrease with the decreasing element size. This means that, for a zero length plastic zone, no mesh refinement would increase the ability of the model to predict the fracture pattern. In other words, fracture models (often found in the literature) based on the sudden release of stress (acoustic release) cannot be objective, regardless of the finite element mesh or other type of grid employed.

In contrast, the *combined single and smeared crack model* is based on the assumption of a finite plastic zone. Thus, very fine meshes in conjunction with the combined single and smeared crack model should result in accurate prediction of both the critical load and fracture pattern.

The problem is that such fine meshes are in many practical applications simply not affordable. Coarser meshes when coupled with the combined single and smeared crack model, result in stress and strain fields in the vicinity of the crack tip being inaccurate by an order of magnitude. Thus, the resulting fracture patterns are extremely sensitive to the local element size and element orientation.

4.10.3 Mohr Coulomb failure criterion

The fracture model presented in the previous aimed at mode I loaded cracks only and assume that tensile strength f_t is a material constant; in this approach also the shear strength f_s (mode II) is assumed to be a material constant.

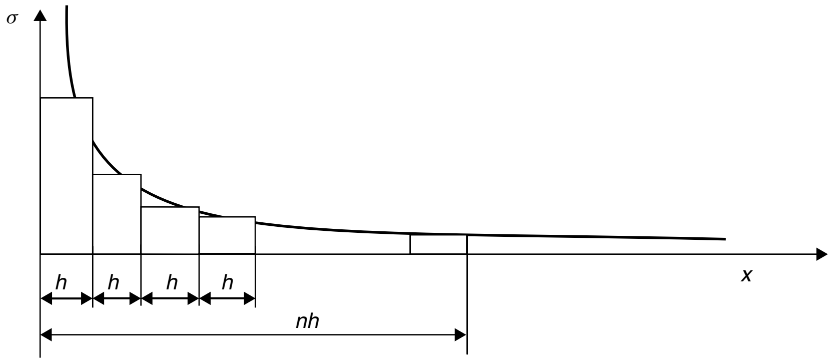

Figure 4.18: A singular stress field approximated by constant stress finite elements (from Munjiza, 2004).

To take into account the dependence of shear strength of the material on the confinement pressure, the Mohr-Coulomb failure criterion with tension cut-off is then considered:

$$\begin{array}{lll} \text{if} & \sigma_n \geq f_t & f_s = c + \mu_i \sigma_n \\ \text{if} & \sigma_n < f_t & f_s = f_t \end{array} \tag{4.64}$$

where c is the internal material cohesion, μ_i is the coefficient of internal friction and σ_n is the normal stress acting on the finite element edges.
The Mohr-Coulomb together with the quasi-static friction law implemented in the *interaction algorithm,* describe the behaviour of pre-existing and newly developed fractures.

4.10.4 A need for more robust fracture solutions

The fracture and fragmentation algorithms proposed in the context of the FDEM are in general sensitive to both element size and element orientation. This is true for both the smeared strain-softening localization based fracture algorithms (proposed in the early days of the combined finite-discrete element development), and the single crack based models proposed in recent years, including the most recent combined single and smeared fracture algorithm.

Only for extremely fine meshes can one expect accurate representation of the stress and strain fields close to the crack tip. In such cases, these fields are not a function of either relative size of individual elements or relative orientation of individual elements.

The errors in the local crack wall geometry are a function of the size of the finite elements employed, and reduce with decreasing size of finite elements, while the length of plastic zone remains constant. This leads to the logical conclusion that with very fine meshes both critical load and fracture pattern are not sensitive to either mesh size or mesh orientation.

However, extremely fine meshes for complex fracture patterns are difficult to realize due to extensive CPU requirements. Thus a problem of this type is and remains a so called "grand challenge problem" that is likely to be addressed by hardware of the future (Munjiza, 2010).

4.11 Summary

The combined finite discrete element method (FDEM) was proposed by A. Munjiza in 1990 and further developed by several research centres until these days.

In FDEM each body is represented by a single discrete element that interacts with the discrete elements close to it. Contact detection and interaction between interacting individual particles, deformability and fracture of the bodies are the characteristic processes of the method. Transition from continua to discontinua is done through fracture and fragmentation processes. The fracture modes considered are:

- Mode I crack - opening mode (a tensile stress normal to the plane of the crack is applied);
- Mode II crack - sliding mode (a shear stress acts parallel to the plane of the crack and perpendicular to it).

The fracture model is actually a combination of the smeared and single crack approaches. The fractures propagate at the boundaries of the discrete elements (i.e. the crack does not propagate inside the discrete element), once the fracture conditions in the material is reached. The FDEM has been implemented in the Y code, which is a robust and efficient two-dimensional research code suitable for modelling continuum/discontinuum behaviour.

References

Harrison, J. P. and Hudson, J. A. (**2000**). *Engineering Rock Mechanics Part II. Illustrative Worked Examples*. Elsevier Ltd.

Jing, L. (**2003**). "A review of techniques, advances and outstanding issues in numerical modelling for rock mechanics and rock engineering." *International Journal of Rock Mechanics and Mining Sciences*, 40(3): 283 – 353.

Mahabadi, O., Grasselli, G., and Munjiza, A. (**2010**). "Y-GUI: A graphical user interface and pre-processor for the combined finite-discrete element code, Y2D, incorporating material heterogeneity." *Computers & Geosciences*, 36: 241–252.

Munjiza, A. (**2004**). *The combined finite-discrete element method*. John Wiley & Sons.

Munjiza, A. (**2010**). "Stability Problems and the Combined Finite-Discrete Element Method." In B. Pàtron Editore, editor, "Mir 2010. Problemi di stabilità nelle opere geotecniche. A cura di G. Barla e M. Barla.", pages 17–33.

Munjiza, A., Owen, D., and Bicanic, N. (**1995**). "A combined finite-discrete element method in transient dynamics of fracturing solids." *Engineering Computations*, 12(2): 145–174.

Chapter 5

Realistic simulation of simple slope failure mechanisms

5.1 Introduction

The purpose of this chapter is to present a numerical code based on the combined finite-discrete element method and to verify its applicability to properly simulate simple slope failure mechanisms. A series of numerical tests have been carried out to highlight the advantages of the combined finite-discrete element method with respect to the conventional numerical techniques in the simulation of such geomechanical problems, specially with reference to the rock fracture process applied to slope stability. The numerical code used in the present thesis is the Y2D code developed by Munjiza (2004). In the first part of the chapter a review of the Y-GUI and Y2D input file data structure is presented. Then, in the second part the results of Y2D numerical modelling are illustrated and discussed. With the purpose to provide a validation of the Y2D code, for each example, a description of the model set up and the relevant aspects which allow for a reliable simulation is given.

5.2 Y2D code

The Y2D code, developed by Munjiza (2004), is a two-dimensional FDEM research code capable of modelling continuum and discontinuum behaviour. The first obstacle one would face in using this code is related to the creation and verification of input files, which had to be typed in an ASCII text editor. To overcome difficulties in the creation of input file, also referred to as ''Y input file'', a graphical user interface, Y-GUI, has been developed for Y2D by the Geomechanics research group of the University of Toronto (Mahabadi et al., 2010).

5.2.1 Y-GUI

Y-GUI is a Graphical User Interface (GUI) for the Y2D code (Munjiza, 2004). It can significantly help the user in the process of setting up a Y2D model. At the same time, the visualization tools implemented allow one to avoid erroneous model set-up.

For simplicity, the interface has been divided into several sections mainly using tab-pages for different data input and graphics. The main features implemented in Y-GUI are listed below:

- easy data input for control database, interaction database, material properties and boundary conditions;
- mesh import from Phase^2 (Rocscience, 2010) or Cubit (Sandia, 2009) as Abaqus mesh, which are the Y2D mesh formats;
- mesh manipulation tools for moving a mesh node, translating selected nodes of a mesh, drawing a mesh and merging two meshes;
- graphical assignment of material properties, boundary and initial conditions to selected elements and selected nodes of a mesh, respectively;
- save screenshot, i.e. the contents in the Graphics page as an image (Bitmap, GIF or JPEG formats);
- graphically define output history points;
- heterogeneity: material properties can be randomly assigned to each individual finite element using a user defined normal distribution. The percentage of each set of material property is defined in the Heterogeneity tab-page. This tool helps count for the natural inhomogeneity of rock masses.

For a more detailed explanation of the Y-GUI refer to Mahabadi et al. (2010).

5.2.2 Y2D data structure

The different databases of the code, with a brief explanation of their functionality and some example parameters of each database, are given in Table 5.1. The "Y input file" typical structure is based on such databases. Moreover, Y-GUI is divided into different components, as shown in Figure 5.1. Most of the data input and graphical processes are done in their corresponding tab-page. The structure of different tab-pages together with their functionalities is given in the following.

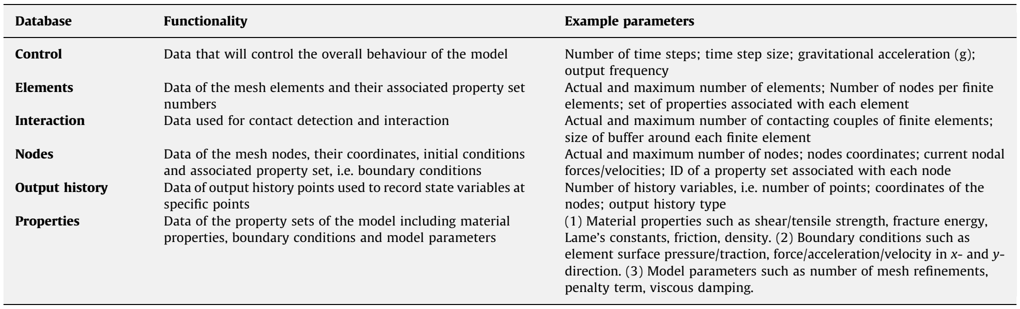

Database	Functionality	Example parameters
Control	Data that will control the overall behaviour of the model	Number of time steps; time step size; gravitational acceleration (g); output frequency
Elements	Data of the mesh elements and their associated property set numbers	Actual and maximum number of elements; Number of nodes per finite elements; set of properties associated with each element
Interaction	Data used for contact detection and interaction	Actual and maximum number of contacting couples of finite elements; size of buffer around each finite element
Nodes	Data of the mesh nodes, their coordinates, initial conditions and associated property set, i.e. boundary conditions	Actual and maximum number of nodes; nodes coordinates; current nodal forces/velocities; ID of a property set associated with each node
Output history	Data of output history points used to record state variables at specific points	Number of history variables, i.e. number of points; coordinates of the nodes; output history type
Properties	Data of the property sets of the model including material properties, boundary conditions and model parameters	(1) Material properties such as shear/tensile strength, fracture energy, Lame's constants, friction, density. (2) Boundary conditions such as element surface pressure/traction, force/acceleration/velocity in x- and y-direction. (3) Model parameters such as number of mesh refinements, penalty term, viscous damping.

Table 5.1: Data structure of Y2D code (from Mahabadi et al., 2010).

Control DB tab-page. This database allows to input the control parameters for each simulation, including the number of time steps, their size, output frequency, gravitational acceleration, as well as the maximum number of elements and nodes (important if the built-in mesh refinement of Y2D is used).

Interaction tab-page. It allows to input the interaction parameters. The most important is the maximum number of contacting couples and the size of buffer used for contact detection. Following a brief description of the meaning of size of buffer is given:

- *size of buffer*: a buffer zone is used to locate nodes close to any surface during contact detection. The larger the zone, the more expensive the contact interaction computations are, but the cheaper is the contact detection computation. Usually a value equal to 1/5 of the size of the smallest finite element mesh has to be set.

Properties tab-page. It includes all the properties that can be assigned to the elements of the mesh, such as Young's modulus, Poisson's ratio, friction coefficient and density, as well as model parameters including viscous damping, penalty term, amount of mesh

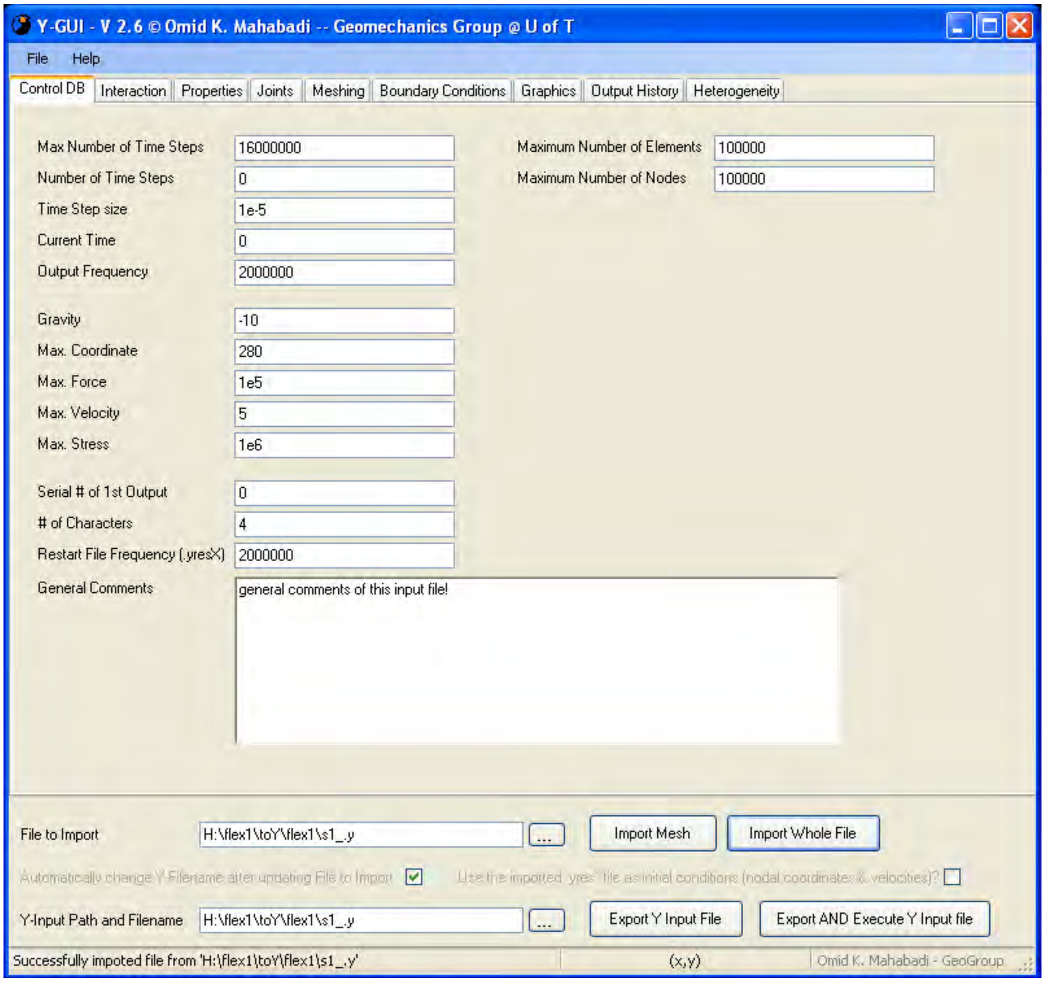

Max Number of Time Steps	16000000
Number of Time Steps	0
Time Step size	1e-5
Current Time	0
Output Frequency	2000000
Gravity	-10
Max. Coordinate	280
Max. Force	1e5
Max. Velocity	5
Max. Stress	1e6
Serial # of 1st Output	0
# of Characters	4
Restart File Frequency (.yresX)	2000000
General Comments	general comments of this input file!
Maximum Number of Elements	100000
Maximum Number of Nodes	100000
File to Import	H:\flex1\toY\flex1\s1_.y
Y-Input Path and Filename	H:\flex1\toY\flex1\s1_.y

Automatically change Y-Filename after updating File to Import ☑

Use the imported .yres* file as initial conditions (nodal coordinates & velocities)? ☐

Successfully impoted file from 'H:\flex1\toY\flex1\s1_.y'

Figure 5.1: Screenshot of Y-GUI interface.

refinement and the type of property. A brief description of several important parameters is given as follows:

- *viscous damping*: the purpose of viscous damping is to minimize high frequencies oscillations which are unavoidably introduced when contact surfaces frequently alternate between contact and non-contact states. The damping modifies the penalty force in order to soften the oscillations. The value of the viscous damping depends on the material properties (E, ρ) and on the finite elements size (h). It is defined as $2h\sqrt{E\rho}$ (finite element smaller than h is critically damped).

- *penalty term*: the penalty parameters are used to evaluate the normal and tangential contact forces. The value for the normal penalty is usually in the range $E < p_n < 10E$, where E is the Young's modulus, and the tangential penalty about 0.1 of the normal penalty. If one or more nodes penetrate through an element the the penalty term should be increased. This may also require a reduction in the time step size (defined in the *Controls DB*) in order to maintain stability of the solution.

Boundary conditions tab-page. The choice of boundary conditions including force, acceleration, or velocity in x- and/or y-direction, as well as element surface pressure or traction can be entered here. These parameters can be also used to constrain elements, e.g., confining the movement of elements by setting velocities to zero.

Graphics tab-page. This page is the main window for all graphical interactions with the user. The imported mesh or file is drawn on it.

Output History tab-page. Here, general parameters for output database, including accuracy of output and factors to scale time and value, can be specified. As soon as output history points are inserted in the graphics page, they will be automatically displayed in a table in the Output History page.

Heterogeneity tab-page. It allows to specify the percentage of different property sets. Once the summation adds up to 100%, property sets can be assigned to selected or all elements in a random way.

It is important to highlight that no units are mentioned for any of the variables in the Y-GUI. Therefore, the user can use any consistent set of units.

5.3 Application of fracture mechanics to rock slope stability

The application of fracture mechanics to rock slope stability has been demonstrated by numerous authors. Tharp and Coffin (1985) and Singh and Sun (1989) analysed both single isolated and edge cracks in a variety of loading conditions including mode I and mode II, and mixed mode I-II. Tharp and Coffin (1985), using a comparison with limit equilibrium techniques, demonstrated the importance of joint persistence. Singh and Sun (1989) similarly, using a finite element approach, demonstrated the importance of both joint persistence and fracture toughness on stability. Scavia (1990) and Scavia and Castelli (1996) successfully applied the displacement discontinuity method in the investigation of the mechanical behaviour of intact rock bridges and rock slope instability due to an array of joints.

Consideration of damage mechanics in geotechnical engineering has increased in the last decade including applications in blasting, underground excavation, petroleum geomechanics and fluid flow studies. Applications to date in rock slope analysis have been less common. The first application has been provided by Eberhardt et al. (2004) who simulated the influence of damage due to unloading by glacial ice and cohesive strength degradation with time, in the stability of the Randa rockslide, using finite element modelling first, then using combined finite-discrete element technique.

Coupled finite-discrete element modelling with fracture propagation has been used successfully in varied geotechnical fields including blasting (Munjiza et al., 1995), underground excavation design (Klerck, 2000), wellbore breakout (Crook et al., 2003) and rock slope instability (Stead and Coggan, 2006). Eberhardt et al. (2004) showed how the use of coupled finite-discrete element models with fracture propagation could be used in conjunction with conventional continuum and discontinuum codes, to further investigate the factors influencing the progressive failure of a major complex rock slope.

The use of the combined finite-discrete element method with fracture propagation capability enables the simulation of the failure initiation stage and also its progressive development and the fragmentation of the rock mass as it translates and is deposited at the slope toe. This is demonstrated in the following examples, based on the work of Stead et al. (2004) and Karami and Stead (2008). A series of numerical tests have been carried out to asses the suitability of Y2D code to properly and efficiently simulate some geotechnical and geomechanical problems. To this purpose some standard rock failure mechanisms have been modelled. The results have been analysed in terms of a “global mechanical response”, evaluating if the tendency of the fracturing response is realistic.

The slope instability mechanisms studied in the present thesis are:

- planar failure;
- bi-planar failure;
- multi-step path slope failure.

5.3.1 Planar failure

The planar failure mechanism has been the first slope instability example modelled using the Y2D code. Figure 5.2 shows the Y2D model geometry of a 100 m high rock slope with a through-going 45° dipping failure surface. In this hypothetical case study, a linear elastic isotropic behaviour was assumed for the rock mass whose properties are shown in Table 5.7 together with the required parameters to characterise the pre-existing joint. The slope geometry was imported in Cubit (Sandia, 2009) and meshed using a Delaunay triangulation scheme with an element size of 1 m for the sliding block. Delaunay triangulation scheme maximizes the minimum angle of all the angles of the triangles in the triangulation; in this way, it tends to avoid skinny triangles.

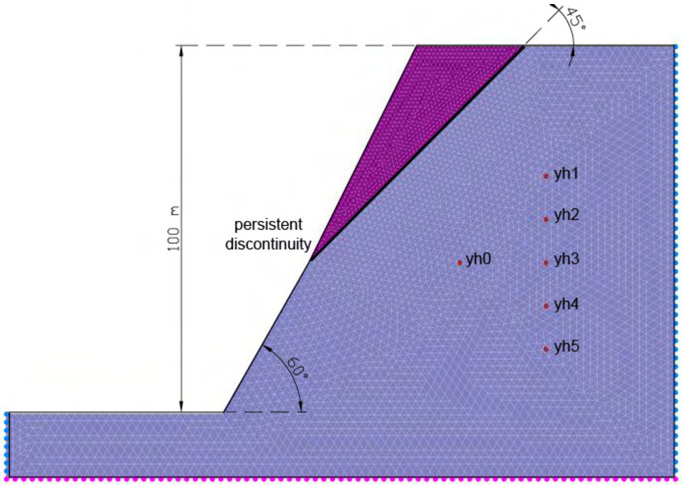

Figure 5.2: Mesh configuration and material distribution for rock slope with persistent joint profile.

The numerical simulation was performed in two stages in order to set the initial stress conditions (*stage1*), and to simulate the instability of the slope (*stage2*). During both stages computation was led to equilibrium and the total kinetic energy of the model was recorded and stored in the *yh0* history file. Initial in situ stress conditions were based on a horizontal to vertical stress ratio *k* of 0.43; during the numerical calculation the vertical and horizontal stress were monitored at five points along a vertical line and stored in the corresponding *yh1-yh5* history files (Figure 5.2). Plane-strain conditions were assumed.

The boundary constraints were: zero x-velocity on the sides and zero x and y-velocity on the base. The first equilibrium state was reached under the gravitational acceleration which was set to 10 m/s^2, during the first stage. Then, in the second stage, the fracture process was activated with the intent to simulate the slope instability. The results show how the Y2D code is able to simulate progressive failure, from the trigger to the material deposition (Figure 5.3). Due to the low tensile strength, as the block starts moving, fractures develop. If the tensile strength of the block was higher (>3 MPa), the block would start sliding along the weak surface and fracturing when it hits the ground.

Figure 5.4 shows the same slope where the persistent joint was characterised by a higher friction angle ($\varphi = 44°$); the same value was given to the internal friction angle of the rock mass and block. It was found that, starting from an early stage of sliding, some fracture develops, then the lower part of the block becomes heavily fractured, also if the block is not moved far away from its initial position. Due to the higher value of the friction angle of the rock mass, at final equilibrium the fragmented rock mass is deposited at the base of the slope with an overall angle approximately equal to 27°.

Intact material properties	*rock mass*	*block*
Elastic modulus, E (GPa)	10	5.6
Poisson's Ratio, ν	0.3	0.3
Density, ρ (kg/m^3)	2400	2400
Internal cohesion, c_i (MPa)	2.75	2
Internal friction angle, φ_i (°)	27	27
Tensile strength, σ_t (MPa)	11	0.16
Fracture energy release rate, G_f (J/m^2)	100	10
Numerical parameters		
Viscous damping (kg/ms)	1.96E+07	7.33E+06
Normal contact penalty (GPa)	100	56
Tangential contact penalty (GPa)	10	5.6
Fracture penalty (GPa)	100	56
Discontinuity properties		
Friction angle, φ (°)	27	
Cohesion, c (Pa)	0	

Table 5.2: Rock mass and discontinuity properties.

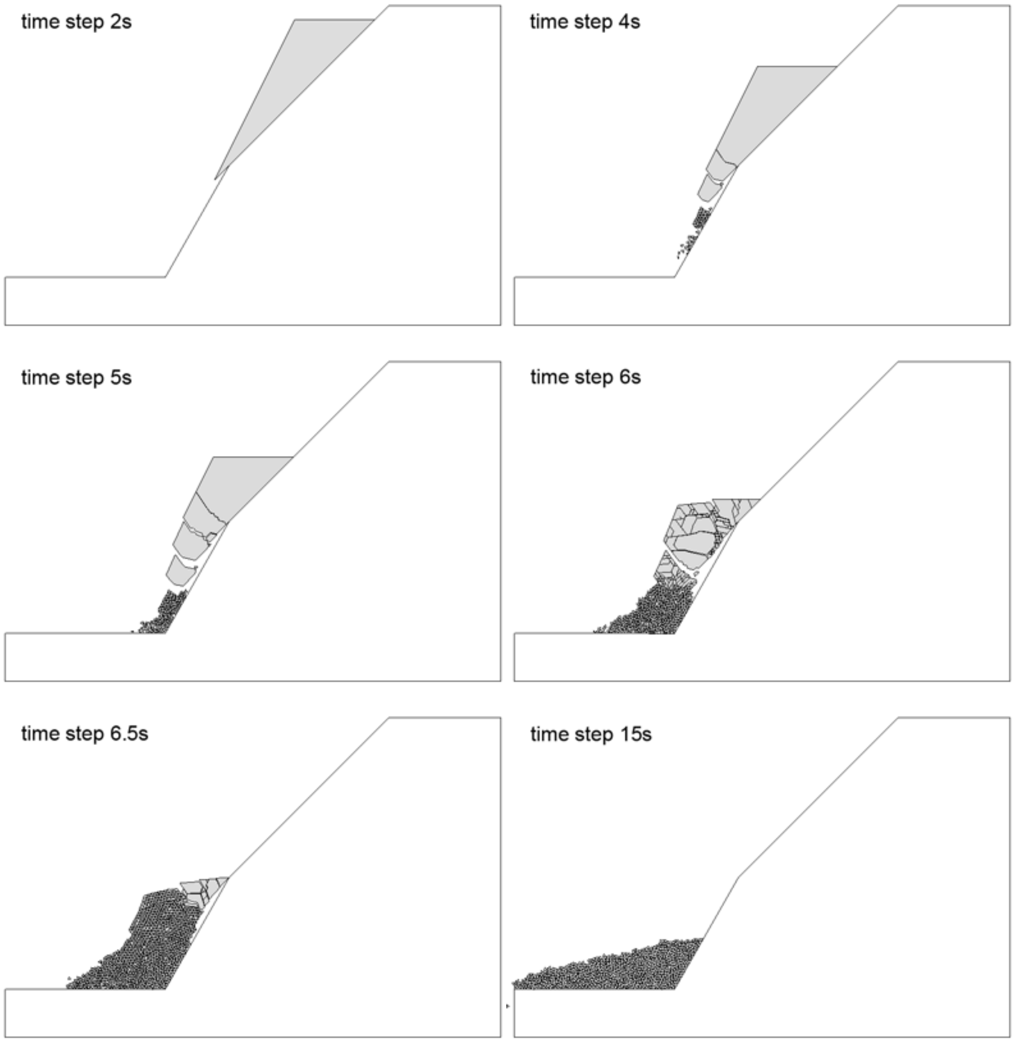

Figure 5.3: Selected output of numerical simulation of planar failure mechanism modelled using Y2D code.

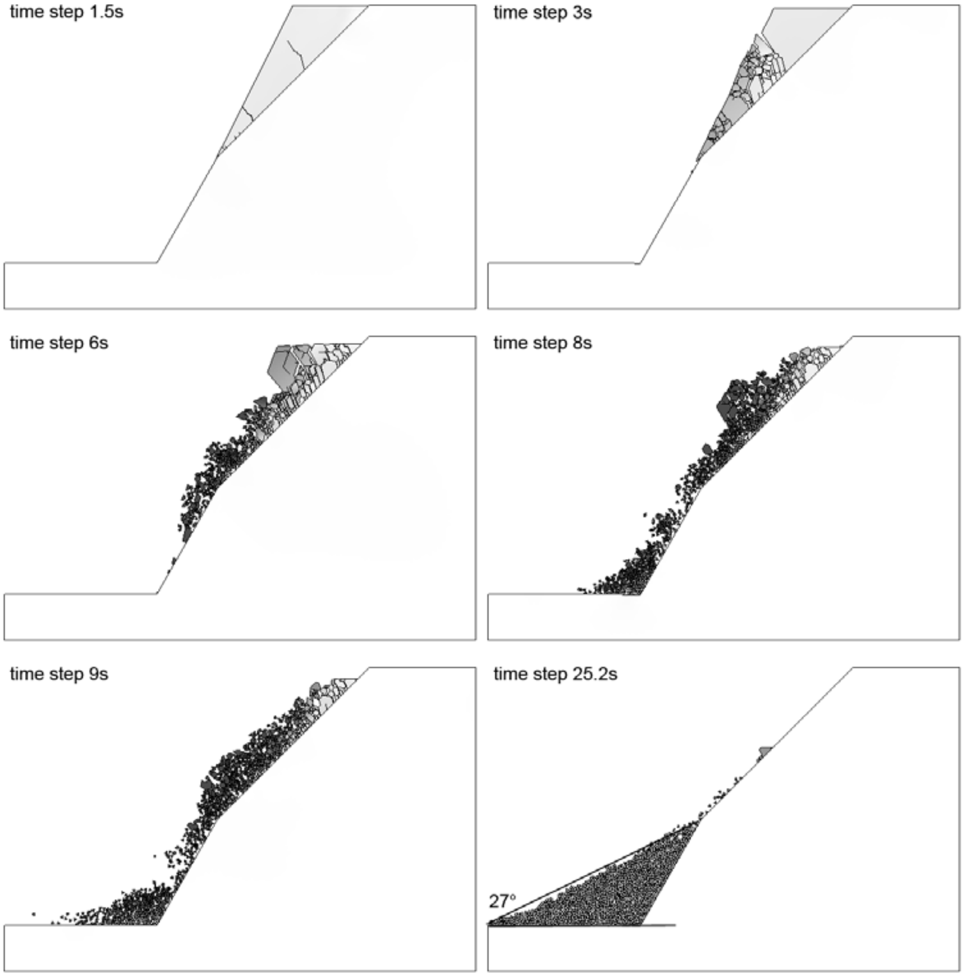

Figure 5.4: Selected output of numerical simulation of planar failure mechanism modelled using Y2D code (joint friction angle φ = 44°).

5.3.2 Bi-planar failure

The bi-planar failure mechanism is the second example of simple slope instability modelled using the Y2D code. In this analysis an attempt is made to model damage accumulation within a block which leads to an active-passive wedge failure. For purpose the geometry adopted for the Y2D model is characterised by a sub-horizontal and vertical joint (Figure 5.5). The upper failure surface may be, for example, a high angle fault and the lower failure surface a weak bedding plane. A linear elastic isotropic behaviour was assumed for the rock mass whose properties represent a weak rock mass (Table 5.3). The geometry of the slope was imported in Phase^2 (Rocscience, 2010) and meshed with an element size of 1m for the block, whereas the base of the model was discretised with a coarse mesh. The boundary conditions consist of setting the x and y-velocity to zero at the lower edge of the model and the x-velocity to zero at the lateral edges.

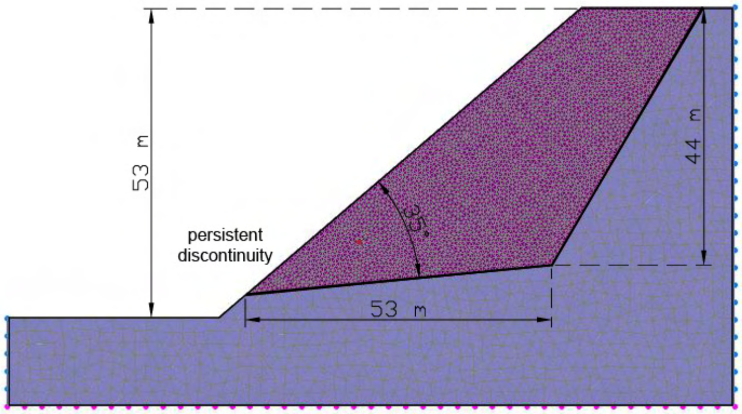

Figure 5.5: Mesh configuration and material distribution.

As observed in the numerical simulation, the pre-existing joints lead to a bi-planar failure involving an active-passive wedge geometry. First a zone of yield due to shear damage develops along the persistent discontinuities and transforms into a tensile failure zone approximating located at the contact between the sub-horizontal and the vertical joint. Then, the tensile failure zone continues upward through the intact rock material. As shown in Figure 5.6, during the development of instability, tensile fractures develop inside the block dividing the rockslide in two distinct blocks, the active and passive block. These fractures create the required space to allow kinematic release as shown in some screenshot of the evolution of the failure. Evidence of the internal fracturing and progressive damage can be observed as surface faults and graben features on the topografic surface of the slope. Note that, in the specialised literature, such failure mechanism is conventionally analysed using an active-passive wedge approach based on the assumption of an interface between the upper active driving block and the lower passive or resisting block, in order to allow a solution that satisfies the kinematics of the failure geometry. As shown in this example, the combined finite-discrete element method can realistically simulate the complex processes that occur in such bi-planar rock slope failure.

Intact material properties	*rock mass*	*block*
Elastic modulus, E (GPa)	10	5.6
Poisson's Ratio, ν	0.3	0.3
Density, ρ (kg/m^3)	2400	2400
Internal cohesion, c_i (MPa)	2.75	2
Internal friction angle, φ_i (°)	27	27
Tensile strength, σ_t (MPa)	11	1
Fracture energy release rate, G_f (J/m^2)	100	50
Numerical parameters		
Viscous damping (kg/ms)	1.96E+07	7.33E+06
Normal contact penalty (GPa)	10	5.6
Tangential contact penalty (GPa)	1	0.56
Fracture penalty (GPa)	10	5.6
Discontinuity properties		
Friction angle, φ (°)	15	
Cohesion, c (Pa)	0	

Table 5.3: Rock mass and discontinuity properties.

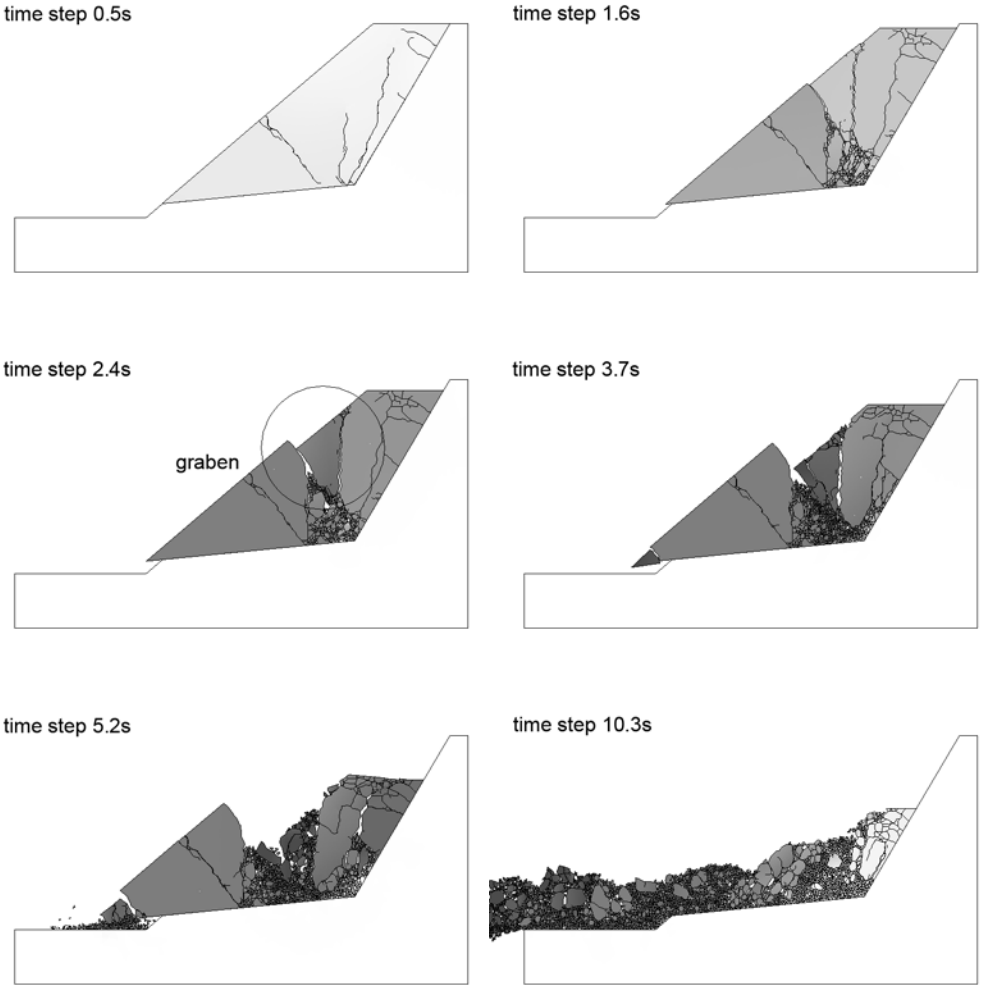

Figure 5.6: Selected output of bi-planar rock failure mechanism simulated with Y2D code.

5.3.3 Multi step-path failure

The third example is based on the work of Karami and Stead (2008). Pre-existing joints within a rock mass influence the slope stability and, if oriented in an unfavourable direction (i.e. dipping out of the slope), may lead to failure. In addition, rock bridges between discrete fractures must fail before large scale movements can be initiated. In this example, an attempt is made to model damage accumulation within a rock slope using the combined finite-discrete element method.

The case study simulated is a 300 m high pit slope with 30 m high 70° benches. The overall pit slope angle is 50°. It is assumed that there is a major joint set 35° inclined, dipping out of the slope face. Each joint can have different properties (i.e. friction, dilation angle and cohesion), with rock bridges in between discrete joints having properties of intact rock. Figure 5.7 shows a rock slope modelled using the Y2D code with several rough joints of various length. Once rock bridges fail by fracturing, movement is expected to initiate. In this hypothetical case study, it is assumed that all the joints have the same strength properties. A rock mass whose properties is assumed to represent a medium strength rock mass is considered for this analysis. Table 5.4 lists the material properties considered for the rock slope and pre-existing joints. Figure 5.7 shows the mesh for the rock slope model with indication of the pre-existing joints. The maximum mesh size at the joint planes is 5 m.

An early stage of fracturing in the slope is shown in Figure 5.8. During the numerical simulation joint surfaces experience progressive damage as in the rock slope. Rock bridges fail as higher tensile stresses develop, accommodated by differential movements across the joints. Progressive damage and failure of rock bridges may facilitate large scale slope instability and movement. Actually, fractures develop along the joints at the rock bridges to form a rough yet planar stepped failure surface. Once the failure surface is through going, the upper blocks start to slide down the slope. This is preceded by normal and shear displacements along the joint.

In order to simulate a large scale slope instability, a FEM analysis with the computation of the critical strength reduction factor (SRF), i.e. safety factor, was carried out with Phase^2 (Rocscience, 2010). The FEM analysis shows that the slope is unstable (Figure 5.9). In order to obtain the development of the instability with the Y2D code, it has been necessary to reduce the internal friction angle of the rock mass which has been set equal to the joint one. The numerical simulation of slope instability is shown in Figure 5.10. The screenshots show the generation of predominantly sub-vertical tensile fractures normal to the direction of downslope movement (i.e. driven by extensional strain). As the density of these fractures increases, the shear plane progressively develops perpendicular to them forming a curvilinear failure surface typical of more ductile failures.

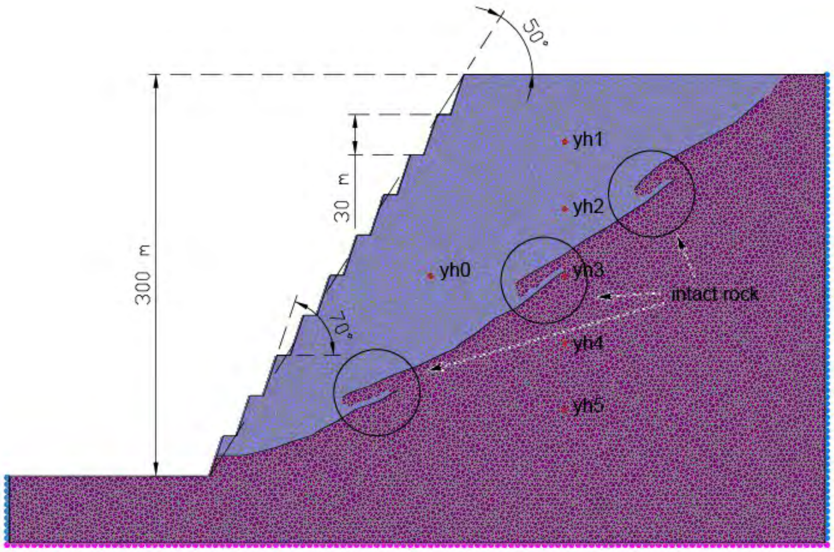

Figure 5.7: Mesh configuration for rock slope with irregular joint profiles.

Intact material properties	
Elastic modulus, E (GPa)	10
Poisson's Ratio, ν	0.25
Density, ρ (kg/m^3)	2600
Internal cohesion, c_{i} (MPa)	5
Internal friction angle, φ_{i} (°)	40
Tensile strength, σ_t (MPa)	2
Fracture energy release rate, G_f (J/m^2)	200
Discontinuity properties	
Friction angle, φ (°)	15
Cohesion, c (Pa)	0
Numerical parameters	
Viscous damping (kg/ms)	1.61E+08
Normal contact penalty (GPa)	100
Tangential contact penalty (GPa)	10
Fracture penalty (GPa)	100

Table 5.4: Rock mass and discontinuity properties.

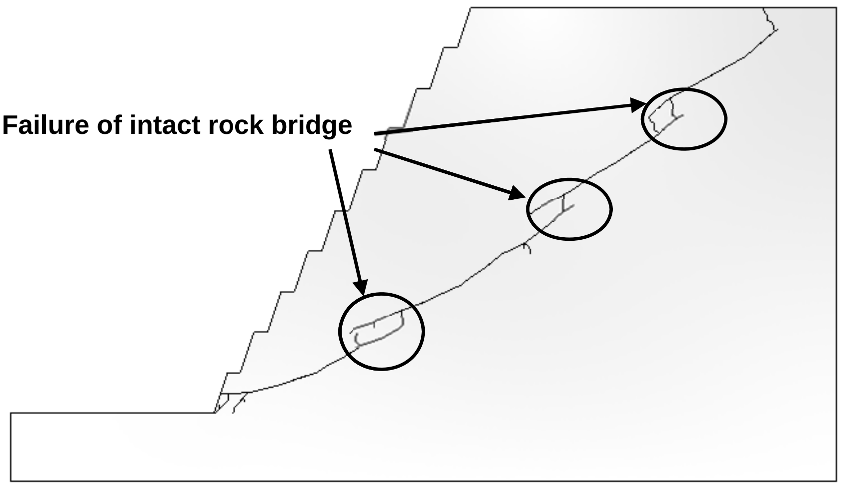

Figure 5.8: Numerical simulation of multi step-path failure using Y2D code: intact rock bridges failure.

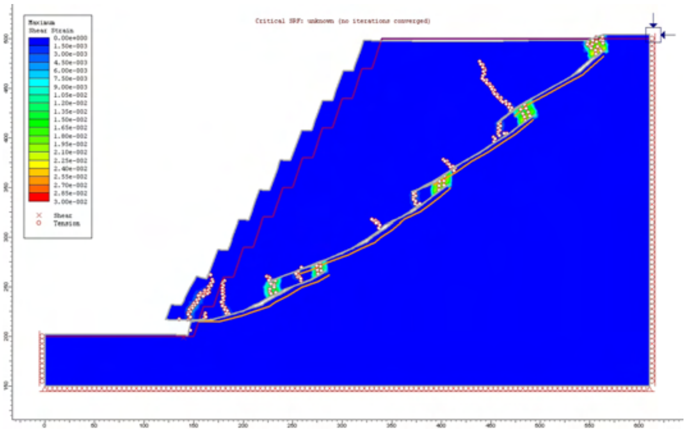

Figure 5.9: FEM simulation: maximum shear strain and deformed mesh when sliding occurs.

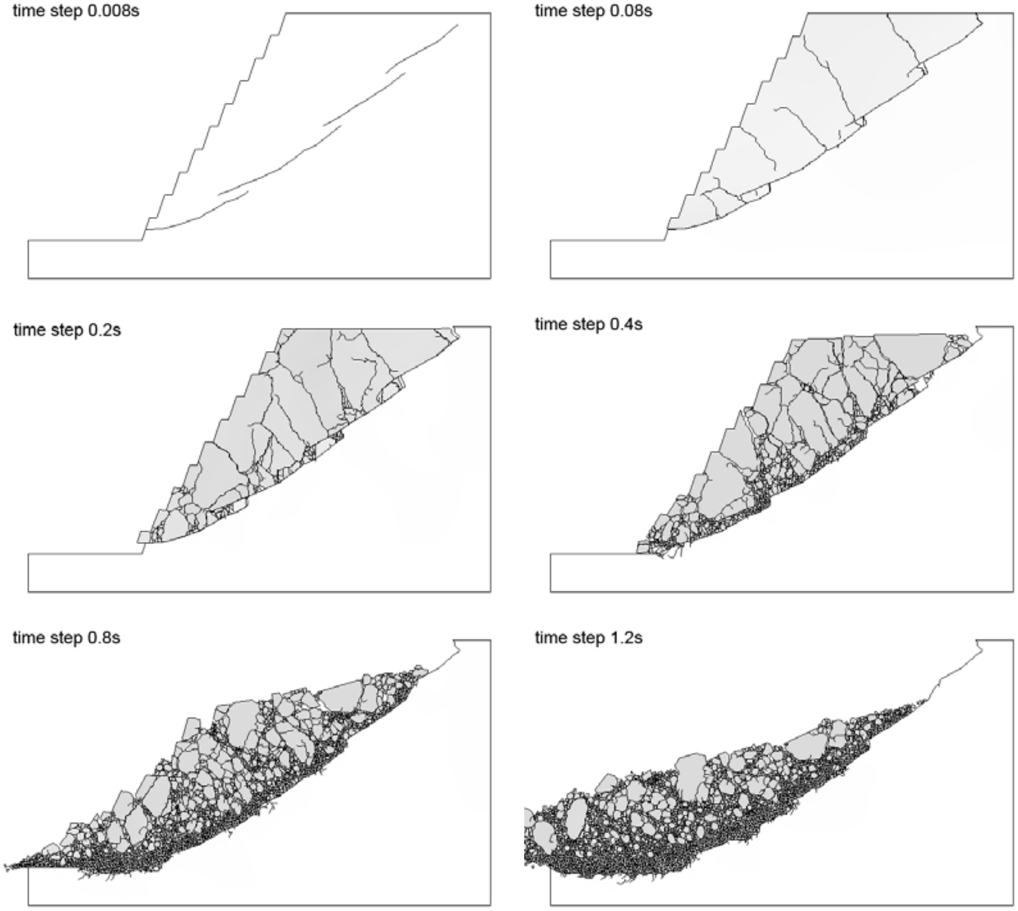

Figure 5.10: Subsequent screenshots of the slope instability simulated with Y2D.

5.4 Block toppling failure

Block toppling failure is a typical rock slope failure mode and involves rotation of columns or blocks of rock around some fixed pointe. The first analytical method for studying the block toppling mechanism is the approach proposed by Goodman and Bray (1976).

According to the Goodman and Bray's classification, the block toppling failure is a primary toppling mode. It occurs when individual columns of hard rock are divided by widely spaced orthogonal joints. The short columns forming the toe of the slope are pushed forward by the loads due to the longer overturning columns behind, and this sliding of the toe allows further toppling to develop up the slope (Figure 5.11).

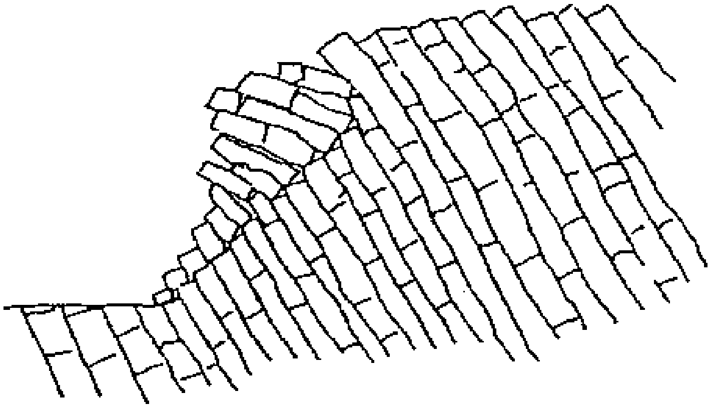

Figure 5.11: Block toppling (Goodman and Bray, 1976).

5.4.1 Limit equilibrium analysis of block toppling on a stepped base

Block toppling can be analysed by the limit equilibrium method (Goodman and Bray, 1976). Consider the regular system of blocks shown in Figure 5.12, in which a slope at angle θ is excavated in a rock mass with layers dipping at $90\text{-}\alpha$. The base is stepped upward with overall inclination β.
The constant a_1, a_2 and b (Figure5.12) are given by:

$$\begin{aligned} a_1 &= \Delta x \tan(\theta - \alpha) \\ a_2 &= \Delta x \tan\alpha \\ b &= \Delta x \tan(\beta - \alpha) \end{aligned} \tag{5.1}$$

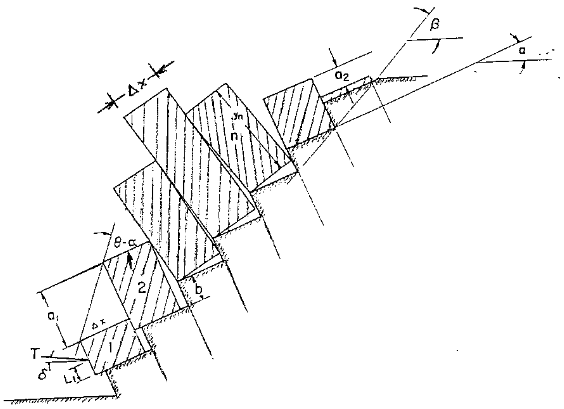

Figure 5.12: Geometric scheme for limit equilibrium analysis of toppling on a stepped base (Goodman and Bray, 1976).

Blocks are numbered from the toe upward. In this idealised model, the height of block n in a position below the crest of the slope is equal to:

$$y_n = (a_1 - b) \tag{5.2}$$

while above the crest

$$y_n = y_{n-1} - a_2 - b \tag{5.3}$$

In the top of the slope, where blocks are shorter, $y_n/\Delta x < \cot\alpha$ and blocks are stable unless $\alpha > \varphi$. However, in the latter case, all blocks slide and further analysis is not necessary.

Below the stable zone, the blocks tend to topple, being restrained from doing so by the normal force transmitted upward from each lower block and the shear forces on the sides of the columns.

Proceeding down the slope, the blocks become shorter, and as the toe region is reached, wherein again $y_n/\Delta x < \cot\alpha$, a block will not topple under its own weight. However, toe blocks may still topple under the normal load transmitted from the toppling zone above. Thus both sliding and toppling must be examined within the toe region.

The minimum force on the downslope side of *block 1*, required to prevent both toppling and sliding, will be negative if the slope is stable, positive if the slope in unstable, or zero if the slope is exactly at limiting equilibrium. To find the friction coefficient required for limiting equilibrium, one can iterate on the choice of μ to find a value making the required toe force equal to zero.

If the friction coefficient is known and the slope is unstable, a support force can be calculated to provide equilibrium.

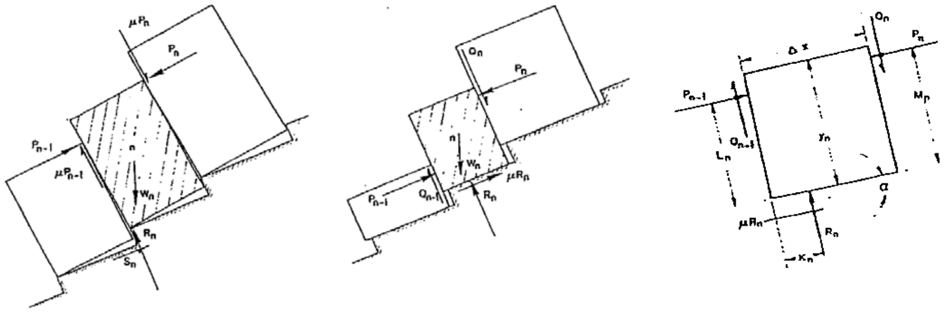

BLOCK n TOPPLING BLOCK n SLIDING

Figure 5.13: Conditions for toppling and for sliding of the *nth* block (Goodman and Bray, 1976).

Figure 5.13 shows the conditions for sliding and toppling in block *n*. The forces in block *n* include: the weight of the block W_p; P_n and Q_n, representing the normal and shear forces acting on the upper side of the block *n* at height M_n; P_{n-1} and P_{n-1} representing the normal and shear forces acting on the lower side of block *n* at height L_n; and R_n and S_n representing the normal and shear forces on the base of block *n* at distance K_n above the lower corner. If block *n* is tending to topple, the points of application of all forces are known, as shown in Figure 5.13.
Below the crest:

$$\begin{aligned} M_n &= y_n \\ L_n &= y_n - a_1 \end{aligned} \tag{5.4}$$

For the crest block:

$$\begin{aligned} M_n &= y_n - a_2 \\ L_n &= y_n - a_1 \end{aligned} \tag{5.5}$$

and above the crest:

$$\begin{aligned} M_n &= y_n - a_2 \\ L_n &= y_n \end{aligned} \tag{5.6}$$

Since the sides of toppling blocks are slipping past one another, the shear forces on the block sides are determined by the normal forces and friction coefficient. There are three unknowns: $P_{n\text{-}1}$, R_n and S_{n} and the problem is determinate. To avoid toppling, a force $P_{n\text{-}1}$ is required:

$$P_{n-1,t} = \frac{P_n\left(M_n - \mu\Delta x\right) + \frac{W_n}{2}\left(y_n \sin\alpha - \Delta x \cos\alpha\right)}{L_n} \tag{5.7}$$

If toppling proves critical for block *n*,

$$R_n = W_n \cos\alpha - \mu\left(P_{n-1,t} - P_n\right) \tag{5.8}$$

and

$$S_n = W_n \sin\alpha - \left(P_{n-1,t} - P_n\right) \tag{5.9}$$

with the condition that

$$R_n > 0 \quad \text{and} \quad \frac{|S_n|}{R_n} \leq \mu \tag{5.10}$$

It is assumed that the coefficient of friction μ along the base of blocks is the same as between blocks. If $S_{\mathrm{n}}<0$, the leading corner of block *n* tends to slide uphill. It will slide into the riser of the stepped base if $S_{\mathrm{n}}<R_{\mathrm{n}}\mu$, mobilizing a force to take the excess base shear.

If block *n* tends to slide, the side forces *Q* are not known nor are their points of application. Assuming P_n, Q_n and M_{n} were known from the previous calculation step, there are five new unknowns: forces $Q_{n\text{-}1}$, $P_{n\text{-}1}$ and R_{n}, and distances $L_n$and K_n. Though the problem is indeterminate, $P_{n\text{-}1,s}$ required to prevent sliding of block *n* can be determined if an assumption is made about the magnitude of $Q_{n\text{-}1}$. If we assume that $Q_{n\text{-}1}=\mu P_{n\text{-}1}$ then the normal force required to prevent sliding of block *n* is:

$$P_{n-1,s} = P_n - \frac{W_n\left(\mu\cos\alpha - \sin\alpha\right)}{1-\mu^2} \tag{5.11}$$

$R_n$is given by Equation A.8 with $P_{n\text{-}1,s}$in place of $P_{n\text{-}1,\mathrm{t}}$ and $S_{n\text{-}1}=R_{n\text{-}1}$.

It should be noted that the above assumption has no effect on the problem as regards the values of forces within the toppling zone, the condition for limiting equilibrium, computation of support force; identical results would be obtained adopting any other reasonable assumption regarding forces in the sliding zone.

If $P_{n\text{-}1,t}>P_{n\text{-}1,s}$ block n tends to topple and $P_{n\text{-}1}=P_{n\text{-}1,t}$. For analysis of the next block, set $P_n=P_{n\text{-}1}$ and proceed. If both $P_{n\text{-}1,t}$ and $P_{n\text{-}1,s}$ are negative, the slope is stable. To determine μ for equilibrium, reduce μ and start again from the highest block.

If $P_{n\text{-}1}$ is positive for block 1, the slope is unstable. Start again with a larger value of μ or compute a support force to achieve the stability. The factor of safety for toppling can be defined from the ratio between the coefficient of friction of the last block without support to the coefficient of friction with support.

Example of block toppling Limit Equilibrium Analysis (LEM). An idealized example is shown in Figure 5.14. A rock slope, 92.5 m high is cut on a 56.6° slope in a layered rock mass, dipping 60° into the hill. A regular system of 16 blocks is placed on a base stepped 1 m every 5 m (β-α = 5.8°). The constant values are:

$$a_1=5.0\text{ m};\ a_2=5.0\text{ m};\ b=1.0\text{ m};\ \Delta x=10.0\text{ m and }\gamma=25\text{ kN/m}^3$$

Block 10 is at the crest, which rises 4° above the horizontal.

Since cotα is 1.78, blocks 16, 15 and 14 comprise a stable zone for all cases in which $\phi > 30°$ ($\mu > 0.577$). In example 1a from Goodman and Bray (1976), μ is set as 0.7855 ($\phi = 38.15°$): P_{13} is then equal to 0 and P_{12} calculated as the greater of $P_{12,t}$ and $P_{12,s}$ given by equation A.7 and equation A.11, respectively.

As shown in Table 5.5, $P_{n\text{-}1,t}$ turns out to be larger until a value of $n=3$, whereupon $P_{n\text{-}1,s}$ remains larger. Thus blocks 4 through 13 constitute the potentially toppling zone and blocks 1 to 3 constitute a sliding zone. The force required to prevent sliding in block 1 tends to zero and the slope is very close to the limit of equilibrium.

In the present thesis, two *cases* referred to slope geometry shown in Figure 5.14, have been studied. In *Case 1*, μ is set as 0.7813 ($\phi = 38°$) and in *Case 2*, μ is set as 0.5773 ($\phi = 30°$). In both cases, the limit equilibrium solution of block toppling has been obtained by an iterative method that gave both the interaction forces between blocks and the stability conditions of each block.

Table 5.5 refers to limit equilibrium solution of *Case 1*: most blocks are unstable - blocks 1,2 and 3 are sliding, whereas blocks from 4 to 13 are overturning. In the upper part of the slope, blocks are stable (i.e. blocks 14, 15 and 16).

The limit equilibrium analysis of *Case 2* (Table 5.6) indicates that all blocks are unstable, i.e. blocks 1,2,3,4,5 on the toe and blocks 13,14,15 on the top of the slope are sliding, whereas the blocks from 6 to 13 are overturning.

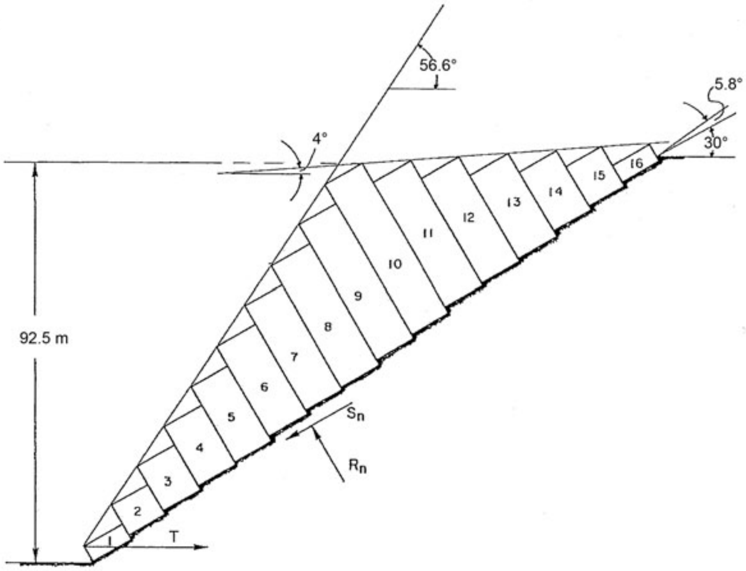

Figure 5.14: Geometry of a toppling slope (Goodman and Bray, 1976).

n	y_n	$y_n/\Delta x$	M_n	L_n	$P_{n,t}$	$P_{n,s}$	P_n	R_n	S_n	S_n/R_n	Mode
16	4.0	0.4	—	4	0	0	0	866	500	0.577	
15	10.0	1.0	5	10	0	0	0	2165	1250	0.577	STABLE
14	16.0	1.6	11	16	0	0	0	3464	2000	0.577	
13	22.0	2.2	17	22	0	0	0	4533.4	2457.5	0.542	
12	28.0	2.8	23	28	292.5	-2588.7	292.5	5643.3	2966.8	0.526	
11	34.0	3.4	29	34	825.7	-3003.2	825.7	6787.6	3520.0	0.519	TOPPLING
10	40.0	4.0	35	35	1556.0	-3175.0	1556.0	7662.1	3729.3	0.487	
9	36.0	3.6	36	31	2826.7	-3150.8	2826.7	6933.8	3404.6	0.491	
8	32.0	3.2	32	27	3922.1	-1409.4	3922.1	6399.8	3327.3	0.520	
7	28.0	2.8	28	23	4594.8	156.8	4594.8	5872.0	3257.8	0.555	
6	24.0	2.4	24	19	4837.0	1300.1	4837.0	5352.9	3199.5	0.598	
5	20.0	2.0	20	15	4637.5	2013.0	4637.5	4848.1	3159.4	0.652	
4	16.0	1.6	16	11	3978.1	2284.1	3978.1	4369.4	3152.5	0.722	
3	12.0	1.2	12	7	2825.6	2095.4	2825.6	3707.3	2912.1	0.7855	
2	8.0	0.8	8	3	1103.1	1413.5	1413.5	2471.4	1941.3	0.7855	SLIDING
1	4.0	0.4	4	-	-1485.1	472.2	472.2	1237.1	971.8	0.7855	

Table 5.5: Example - μ = 0.7855 (from Goodman and Bray, 1976).

<table>
<tr><th colspan="11"><i>Case 1</i></th></tr>
<tr><th>n</th><th>y_n</th><th>M_n</th><th>L_n</th><th>$P_{n,t}$</th><th>$P_{n,s}$</th><th>P_n</th><th>R_n</th><th>S_n</th><th>S_n/R_n</th><th>NOTE</th></tr>
<tr><td>16</td><td>4.</td><td>-1.</td><td>4.</td><td>0.</td><td>0.</td><td>0.</td><td>866.</td><td>500.</td><td>.577</td><td>STABLE</td></tr>
<tr><td>15</td><td>10.</td><td>5.</td><td>10.</td><td>-833.</td><td>-453.</td><td>0.</td><td>2165.</td><td>1250.</td><td>.577</td><td>STABLE</td></tr>
<tr><td>14</td><td>16.</td><td>11.</td><td>16.</td><td>-458.</td><td>-1133.</td><td>0.</td><td>3464.</td><td>2000.</td><td>.577</td><td>STABLE</td></tr>
<tr><td>13</td><td>22.</td><td>17.</td><td>22.</td><td>-83.</td><td>-1813.</td><td>0.</td><td>4535.</td><td>2458.</td><td>.542</td><td>TOPPLING</td></tr>
<tr><td>12</td><td>28.</td><td>23.</td><td>28.</td><td>292.</td><td>-2493.</td><td>292.</td><td>5645.</td><td>2966.</td><td>.525</td><td>TOPPLING</td></tr>
<tr><td>11</td><td>34.</td><td>29.</td><td>34.</td><td>826.</td><td>-2881.</td><td>826.</td><td>6790.</td><td>3519.</td><td>.518</td><td>TOPPLING</td></tr>
<tr><td>10</td><td>40.</td><td>35.</td><td>35.</td><td>1557.</td><td>-3027.</td><td>1557.</td><td>7666.</td><td>3728.</td><td>.486</td><td>TOPPLING</td></tr>
<tr><td>9</td><td>36.</td><td>36.</td><td>31.</td><td>2830.</td><td>-2976.</td><td>2830.</td><td>6936.</td><td>3401.</td><td>.490</td><td>TOPPLING</td></tr>
<tr><td>8</td><td>32.</td><td>32.</td><td>27.</td><td>3929.</td><td>-1250.</td><td>3929.</td><td>6398.</td><td>3322.</td><td>.519</td><td>TOPPLING</td></tr>
<tr><td>7</td><td>28.</td><td>28.</td><td>23.</td><td>4607.</td><td>302.</td><td>4607.</td><td>5867.</td><td>3251.</td><td>.554</td><td>TOPPLING</td></tr>
<tr><td>6</td><td>24.</td><td>24.</td><td>19.</td><td>4856.</td><td>1433.</td><td>4856.</td><td>5346.</td><td>3192.</td><td>.597</td><td>TOPPLING</td></tr>
<tr><td>5</td><td>20.</td><td>20.</td><td>15.</td><td>4664.</td><td>2136.</td><td>4664.</td><td>4839.</td><td>3151.</td><td>.651</td><td>TOPPLING</td></tr>
<tr><td>4</td><td>16.</td><td>16.</td><td>11.</td><td>4013.</td><td>2398.</td><td>4013.</td><td>4360.</td><td>3146.</td><td>.722</td><td>TOPPLING</td></tr>
<tr><td>3</td><td>12.</td><td>12.</td><td>7.</td><td>2867.</td><td>2200.</td><td>2867.</td><td>3661.</td><td>2860.</td><td>.781</td><td>SLIDING</td></tr>
<tr><td>2</td><td>8.</td><td>8.</td><td>3.</td><td>1145.</td><td>1507.</td><td>1507.</td><td>2440.</td><td>1907.</td><td>.781</td><td>SLIDING</td></tr>
<tr><td>1</td><td>4.</td><td>4.</td><td>4.</td><td>-1459.</td><td>600.</td><td>60.</td><td>1220.</td><td>953.</td><td>.781</td><td>SLIDING</td></tr>
<tr><th colspan="11"><i>Case 2</i></th></tr>
<tr><td>16</td><td>4.</td><td>-1.</td><td>4.</td><td>0.</td><td>0.</td><td>0.</td><td>866.</td><td>500.</td><td>.577</td><td>SLIDING</td></tr>
<tr><td>15</td><td>10.</td><td>5.</td><td>10.</td><td>-833.</td><td>0</td><td>0.</td><td>2165.</td><td>1250.</td><td>.577</td><td>SLIDING</td></tr>
<tr><td>14</td><td>16.</td><td>11.</td><td>16.</td><td>-458.</td><td>0.</td><td>0.</td><td>3464.</td><td>2000.</td><td>.577</td><td>SLIDING</td></tr>
<tr><td>13</td><td>22.</td><td>17.</td><td>22.</td><td>-83.</td><td>0.</td><td>0.</td><td>4594.</td><td>2458.</td><td>.535</td><td>TOPPLING</td></tr>
<tr><td>12</td><td>28.</td><td>23.</td><td>28.</td><td>292.</td><td>0.</td><td>292.</td><td>5742.</td><td>2945.</td><td>.513</td><td>TOPPLING</td></tr>
<tr><td>11</td><td>34.</td><td>29.</td><td>34.</td><td>847.</td><td>292.</td><td>847.</td><td>6914.</td><td>3476.</td><td>.503</td><td>TOPPLING</td></tr>
<tr><td>10</td><td>40.</td><td>35.</td><td>35.</td><td>1621.</td><td>847.</td><td>1621.</td><td>7879.</td><td>3647.</td><td>.463</td><td>TOPPLING</td></tr>
<tr><td>9</td><td>36.</td><td>36.</td><td>31.</td><td>2974.</td><td>1621.</td><td>2974.</td><td>7024.</td><td>3218.</td><td>.456</td><td>TOPPLING</td></tr>
<tr><td>8</td><td>32.</td><td>32.</td><td>27.</td><td>4255.</td><td>2974.</td><td>4255.</td><td>6371.</td><td>3035.</td><td>.476</td><td>TOPPLING</td></tr>
<tr><td>7</td><td>28.</td><td>28.</td><td>23.</td><td>5221.</td><td>4255.</td><td>5221.</td><td>5694.</td><td>2863.</td><td>.503</td><td>TOPPLING</td></tr>
<tr><td>6</td><td>24.</td><td>24.</td><td>19.</td><td>5858.</td><td>5221.</td><td>5858.</td><td>5029.</td><td>2711.</td><td>.539</td><td>TOPPLING</td></tr>
<tr><td>5</td><td>20.</td><td>20.</td><td>15.</td><td>6147.</td><td>5858.</td><td>6147.</td><td>4330.</td><td>2500.</td><td>.577</td><td>SLIDING</td></tr>
<tr><td>4</td><td>16.</td><td>16.</td><td>11.</td><td>6053.</td><td>6147.</td><td>6147.</td><td>3464.</td><td>2000.</td><td>.577</td><td>SLIDING</td></tr>
<tr><td>3</td><td>12.</td><td>12.</td><td>7.</td><td>5594.</td><td>6147.</td><td>6147.</td><td>2598.</td><td>1500.</td><td>577</td><td>SLIDING</td></tr>
<tr><td>2</td><td>8.</td><td>8.</td><td>3.</td><td>4897.</td><td>6147.</td><td>6147.</td><td>1732.</td><td>1000.</td><td>577</td><td>SLIDING</td></tr>
<tr><td>1</td><td>4.</td><td>4.</td><td>4.</td><td>3008.</td><td>6147.</td><td>577</td><td>866.</td><td>500.</td><td>.577</td><td>SLIDING</td></tr>
</table>

Table 5.6: Analytical solution of block toppling.

5.4.2 Numerical simulation of block toppling using DEM

The two cases described in the previous section and analysed with the Goodman and Bray's limit equilibrium method, were also analysed with the distinct element method (DEM). In the following pages, the numerical simulations are described.

5.4.2.1 Block toppling model (elastic blocks)

The model built with UDEC (ITASCA Consulting Group, 2004), consists of 16 prismatic blocks and one big block (block number 202) representing the slope (Figure 7.2). The block 202 was fixed, whereas other blocks were free to move. Blocks behave as isotropic linear elastic material according to parameters defined in Table 5.7. The Coulomb slip constitutive model was used for discontinuity strength. This requires the following input parameters: joint normal stiffness, shear stiffness, friction angle, dilation angle, cohesive strength, and tensile strength (Table 5.7). Normal and tangential stiffness applied to joint sets were respectively equal to $4 \cdot 10^9$ Pa/m and $0.0144 \cdot 10^9$ Pa/m.

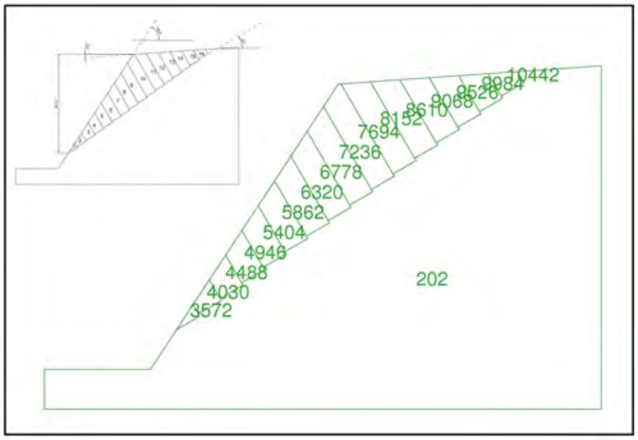

Figure 5.15: Basic slope geometry used in the numerical modelling.

Case 1. The block toppling failure, simulated with UDEC, is characterised by sliding blocks at the toe of the slope, overturning blocks in the middle region of the slope, and stable blocks at the top (Figure 5.16). Consequently, except for the blocks that are stable on the top of the slope, the numerical solution agree with the analytical one. Actually, the sligth difference may be due to the different geometry of blocks.

Intact material properties	*Case 1*	*Case 2*
Elastic modulus, E (GPa)	6	6
Poisson's Ratio, ν	0.25	0.25
Density, ρ (kg/m^3)	2500	2500
Discontinuity properties		
Vertical joints friction angle, φ_{vj} (°)	38	30
Base plane friction angle, φ_{bp} (°)	38	30
Tensile strength, σ_{t}(MPa)	0	0
Cohesion, c (MPa)	0	0

Table 5.7: Rock mass and joints properties.

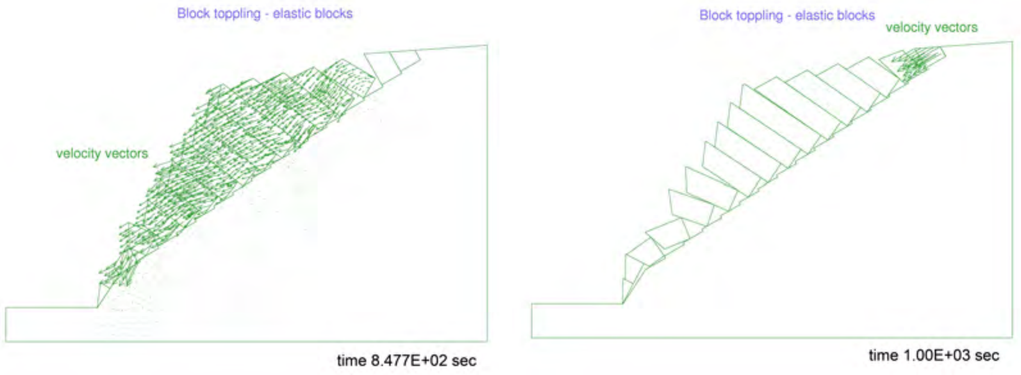

Figure 5.16: Block toppling model with elastic blocks: velocity vectors obtained in UDEC numerical simulation.

Case 2. The same geometry was modeled with UDEC by assigning to joints a friction angle of 30° (Table 5.8). It was found that, movement begins at the toe of the slope, where four blocks are sliding, and block toppling occurs upslope (Figure 5.16). Although the overall stability is the same, in the analytical solution, one more block is sliding.

5.4.2.2 Block toppling model (elastoplastic blocks)

Other numerical analyses were performed using the Mohr Coulomb elastoplastic constitutive law for modelling the blocks behaviour. The parameters required for blocks are summarized in Table 5.8: they are internal friction angle, dilation angle, cohesion, and tensile strength. The properties assigned to joints are the same as the previous ones used in the UDEC analyses.

Case 1. The numerical results are shown in Figure 5.18 in terms of velocity vectors and yielded elements. The yielded elements are "yielded in the past", i.e. they yielded at the beginning of the simulation, and a subsequent stress redistribution had unloaded the yielding elements so that their stress no longer satisfies the yield criterion. According with previous solutions (analytical and numerical), blocks are all unstable except for the two blocks at the top of the slope.

Intact material properties	*Case 1*	*Case 2*
Elastic modulus, E (GPa)	6	6
Poisson's Ratio, ν	0.25	0.25
Density, ρ (kg/m^3)	2500	2500
Internal cohesion, c_{i} (MPa)	2.75	2.75
Internal friction angle, φ_{i} (°)	38	30
Dilation angle, ψ (°)	0	0
Tensile strength, σ_{t}(MPa)	11	11

Table 5.8: Rock mass properties.

Case 2. If the friction angle of rock the mass and joints is set equal to 30°, the final result of the block toppling analysis is characterised by instability of all blocks, except for the uppermost block (Figure 5.17).

5.4.3 Numerical simulation of block toppling using FDEM

In this subsection the FDEM analyses of block toppling are described. Actually, in order to compare results, the UDEC analyses have been performed also with Y2D code.

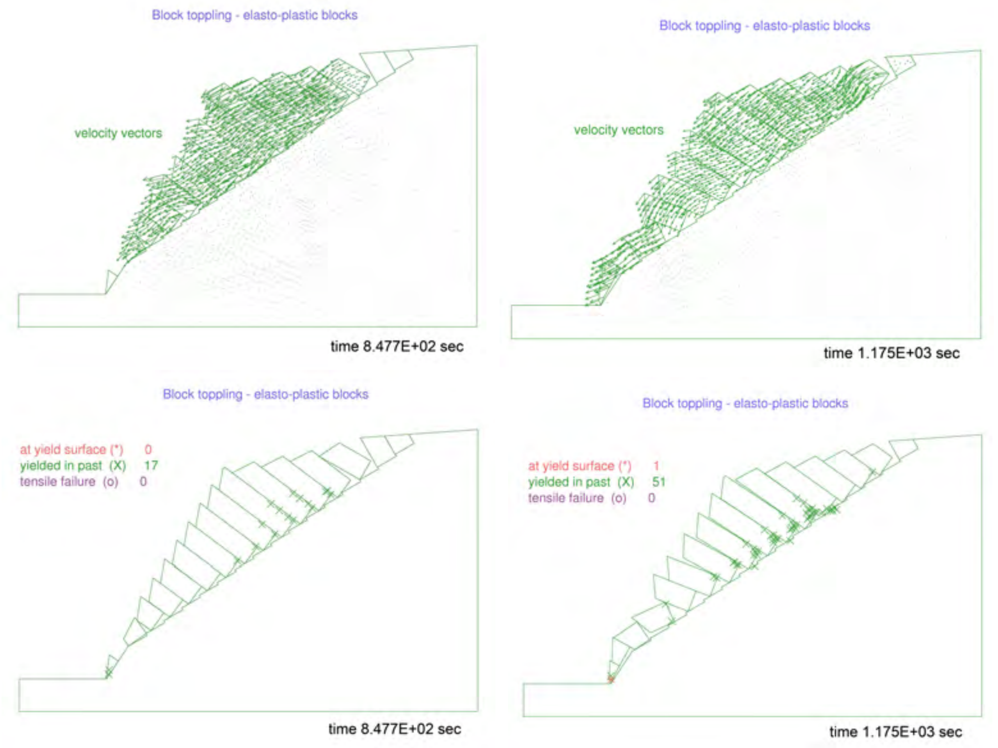

Figure 5.17: Block toppling model with elastoplastic blocks: velocity vectors at the end of simulation and yielded elements from UDEC.

The geometry of the slope, shown in Figure 5.24, was imported in Phase^2 (Rocscience, 2010) and meshed with a nominal element size of 2 m (Figure 5.18). The generated mesh has 15524 elements and 8201 nodes. The rock mass was assumed to behave according to an isotropic linear elastic constitutive law with material parameters summarized in Table 5.7. The boundary conditions assigned to the model were: x and y displacements fixed on the base and x displacements fixed on the sides.

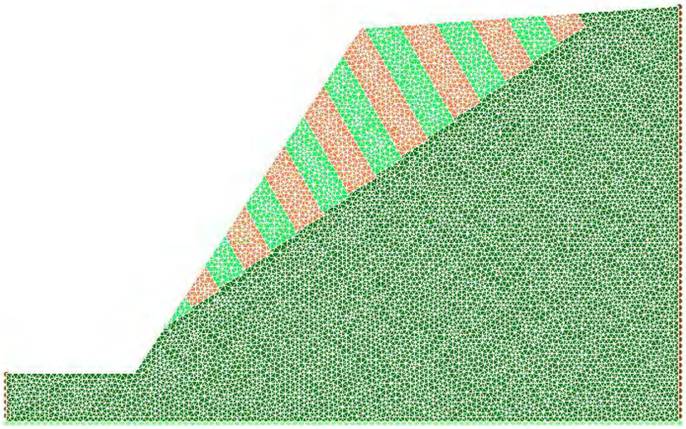

Figure 5.18: Finite element mesh used for FDEM analysis of block toppling.

The simulation was performed in two stages. In the first stage all the blocks were fixed and a state of equilibrium was reached as shown in Figure 5.19 where the total kinetic energy versus the simulation time is plotted. The first stage was performed to assign the initial in situ stress conditions to the slope. Initial in situ stress conditions were based on a horizontal to vertical stress ratio k of 0.33. In the second stage, the constraints applied to the blocks slope removed and the new equilibrium condition was achieved.

Case 1. According to the UDEC analysis, the block toppling analysed with the Y2D code shows that all the blocks are unstable except for the two blocks at the top of the slope (Figure 5.20). In both numerical analyses, at the beginning of simulation, the lower three blocks were sliding, whereas blocks in the middle of the slope were overturning. On the other hand, the final static configuration was very different (Figure 5.16 vs 5.20).

Case 2. In this case, the friction angle of joints was set equal to 30°. The results obtained with the Y2D code simulation of block toppling instability are shown in Figure

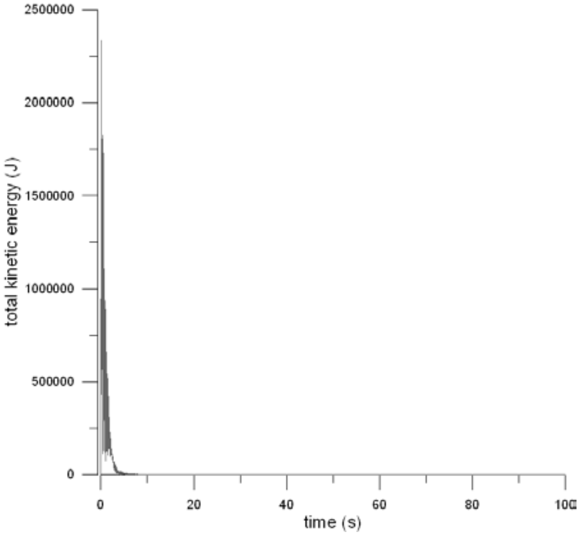

Figure 5.19: Total kinetic energy during the first stage of FDEM analysis.

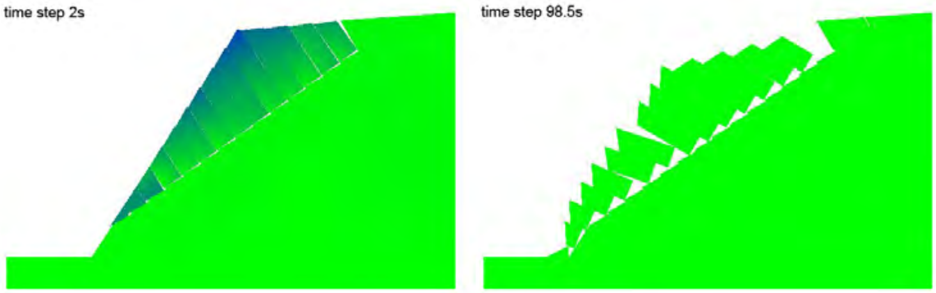

Figure 5.20: *Case 1*. Velocity distribution at $t = 2s$ (left) and at the end of simulation (right).

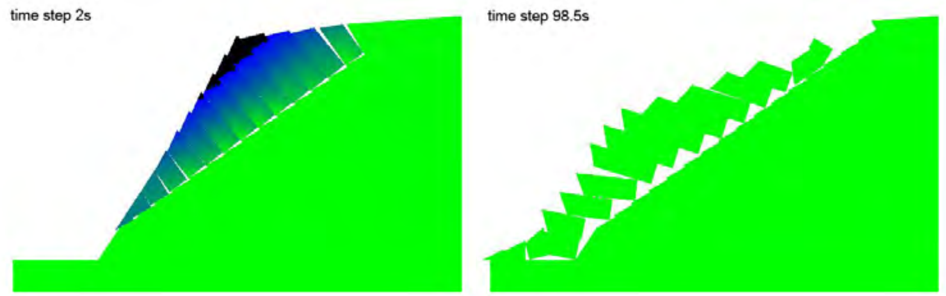

Figure 5.21: *Case 2*. Velocity distribution at $t = 2s$ (left) and at the end of simulation (right).

5.21. UDEC and Y2D analyses show that all blocks were unstable, and the lower three blocks were sliding, whereas the other blocks were overturning. On the other hand, the final static configuration is very different (Figure 5.16 vs 5.21).

Case 1 - Case 2: simulation of total block toppling instability The main advantage of the combined finite-discrete element method is its capacity to model the transition from continua to discontinua by explicitly considering fracture and fragmentation processes. Such a unique characteristic can be used to apply the "total slope failure" approach to study block toppling instability.

If in the second stage of the Y2D analysis, the fracturing process is allowed, the complete development of instability, from the trigger to the final state of rest of the material mobilized, can be simulated. A fracture energy of 100 N/m was used. Figure 5.22 shows subsequent screenshots of instability due to a block toppling mechanism obtained with the Y2D code.

Concerning the overall stability of the slope, once again it was similar. Actually, all the blocks were unstable except for the uppermost block. Despite this, the most important difference is that the plastic zone in the UDEC analysis was not so extended to presume the blocks fragmentation obtained with Y2D analysis. Moreover, the run out distance obtained in the two simulation was quite different. The same conclusion remarks can be drawn for *Case 2* (Figure 5.23).

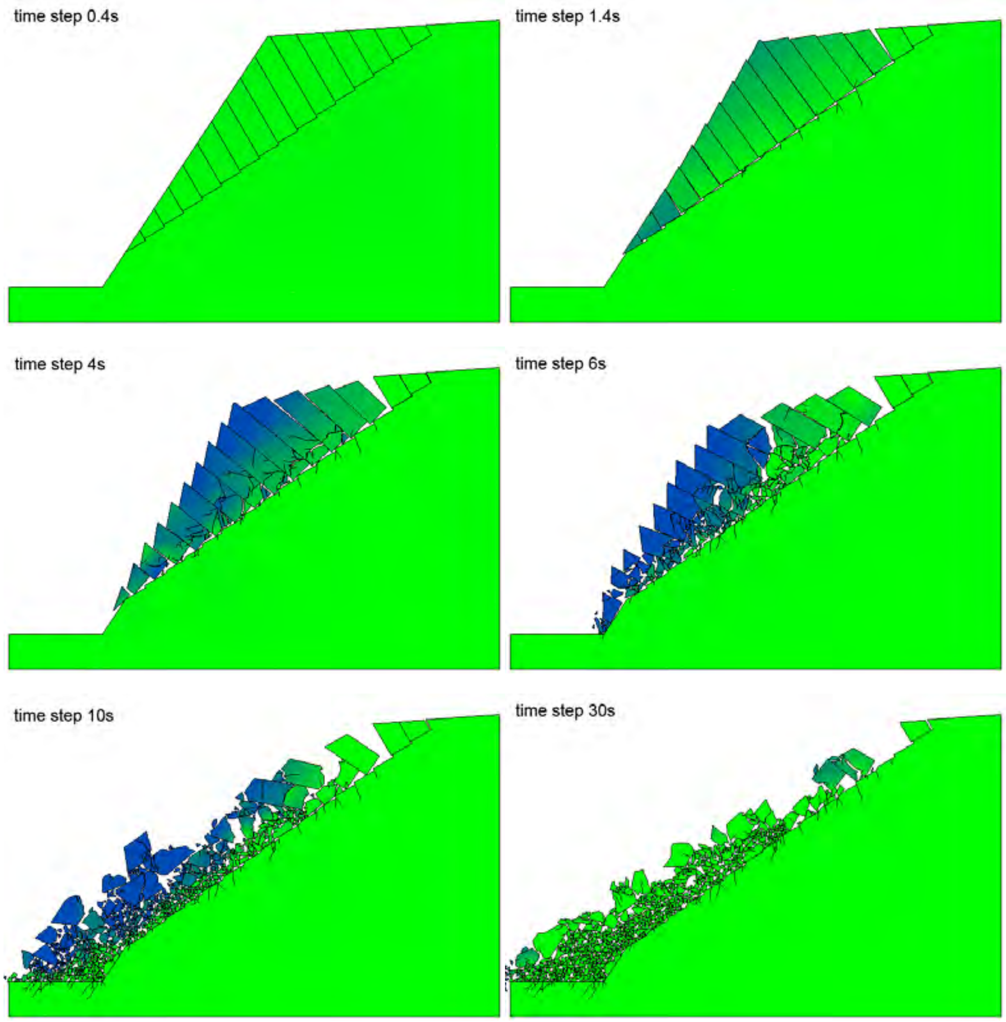

Figure 5.22: *Case 1*. Y2D analysis of block toppling. Selected output.

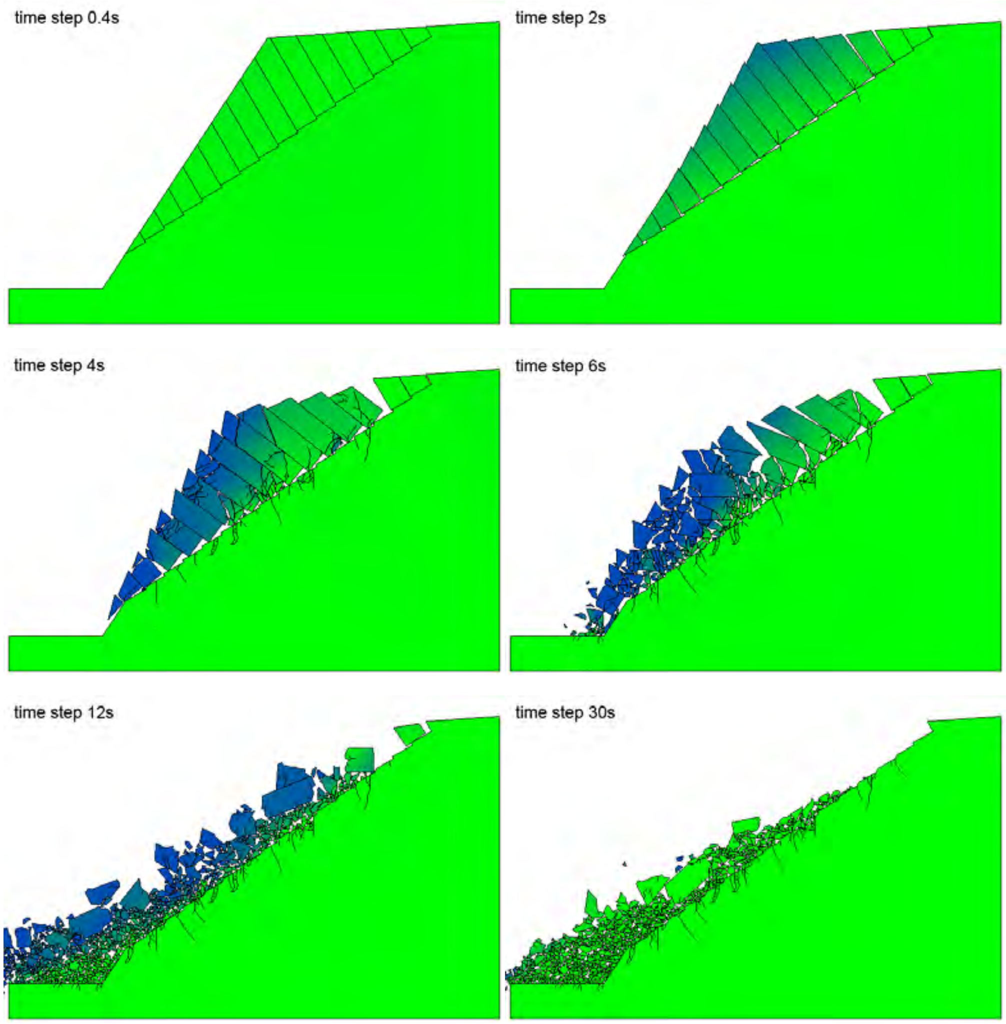

Figure 5.23: *Case* 2. Y2D analysis of block toppling. Selected output.

5.5 Stability of an homogeneous slope

In this section the numerical simulation of the stability of an homogeneous slope using the limit equilibrium method (LEM), the finite element method (FEM) and the combined finite-discrete element method (FDEM), is described. The influence of the method used to simulate the initial stress conditions and the mesh size are considered. The attention is then posed on the calculation of the factor of safety for a slope instability along a circular sliding surface. This work was presented at the 13th IACMAG Conference, May 2011 in Melbourne, Australia (Piovano et al., 2011).

5.5.1 Definition of the slope problem

The slope to be considered in the following is shown in Figure 5.24. The slope angle with respect to the horizontal is taken to be equal to 33.7°. The ground is considered to be homogeneous with the material properties given in Table 5.9, where an elastic perfectly plastic constitutive behaviour is assumed with the Mohr Coulomb yield function.

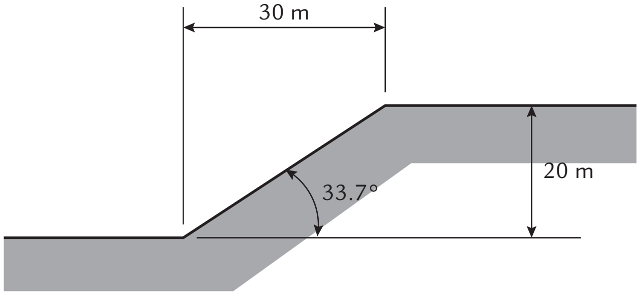

Figure 5.24: Geometry of the slope problem (Piovano et al., 2011).

5.5.2 Limit Equilibrium Method (LEM)

The LEM and the Slide code (Rocscience, 2007) were adopted to compute the factor of safety of the slope. The global minimum factor of safety of the slope under study, obtained from the limit equilibrium analysis with the Bishop simplified method, was found to be 1.781. The corresponding circular sliding surface is shown in Figure 5.25.

Intact material properties	
Elastic modulus, E (MPa)	50
Poisson's Ratio, ν	0.4
Density, ρ (kg/m^3)	1900
Internal cohesion, c_i (kPa)	28
Internal friction angle, φ_i (°)	30
Dilation angle, ψ (°)	0
Tensile strength, σ_t(kPa)	28
Fracture energy release rate, G_f (J/m^2)	10

Table 5.9: Ground properties.

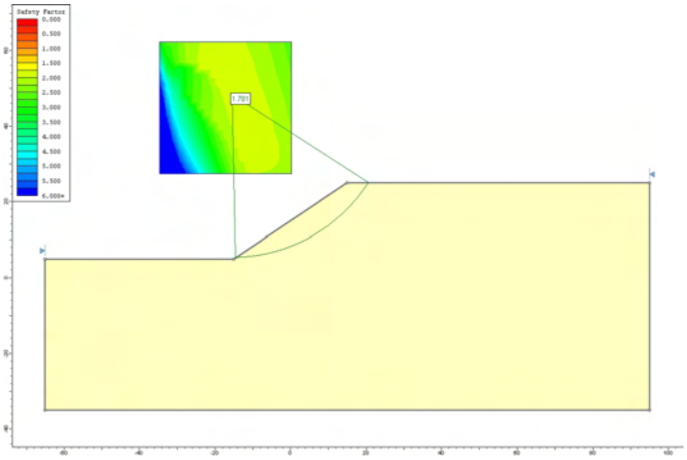

Figure 5.25: Global minimum sliding surface with the factor of safety computed with LEM (Piovano et al., 2011).

5.5.3 Finite Element Method (FEM)

Phase² (Rocscience 2009b) was used to compute the factor of safety of the slope shown in Figure 5.24 by the Shear Strength Reduction (SSR) method. The critical SRF is found to be equivalent to the safety factor of the slope. The mesh adopted in the numerical simulation performed consisted of 10705 elements and 21646 nodes. The element type is a 6-noded triangle with a 2 m side. Figure 5.26 shows the mesh and the boundary conditions adopted. Vertical displacements are fixed at the bottom while horizontal displacements are restrained along the vertical boundaries. With the mechanical properties given in Table 5.9, the SRF obtained with the SSR analysis results to be equal to 1.7 and agrees with the LEM value. Figure 5.27 shows a plot of the maximum shear strains in the model including the inferred sliding surface.

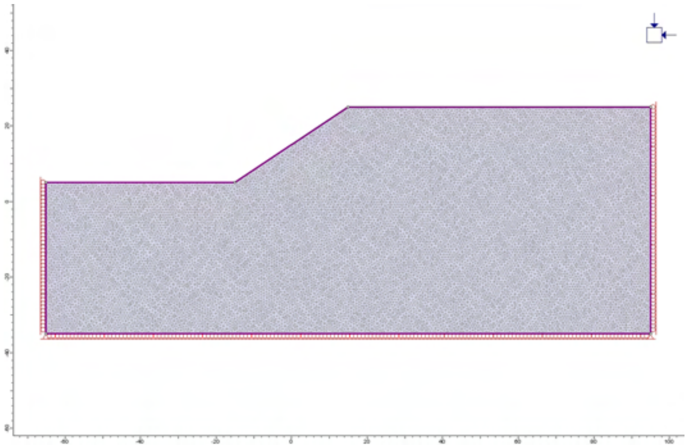

Figure 5.26: Finite Element mesh and boundary conditions (Piovano et al., 2011).

5.5.4 Combined finite-discrete element method (FDEM)

The FDEM model of the example slope was built according to the geometry shown in Figure 5.24. The mesh and boundary conditions are consistent with those adopted with FEM (Figure 5.26). The numerical simulations were performed in two stages: 1) set the initial stress conditions, 2) simulate the instability of the slope. The first stage was run with the intent to reproduce the initial state of stress within the slope with no fracturing being allowed between the finite elements. An isotropic linearly elastic behaviour was

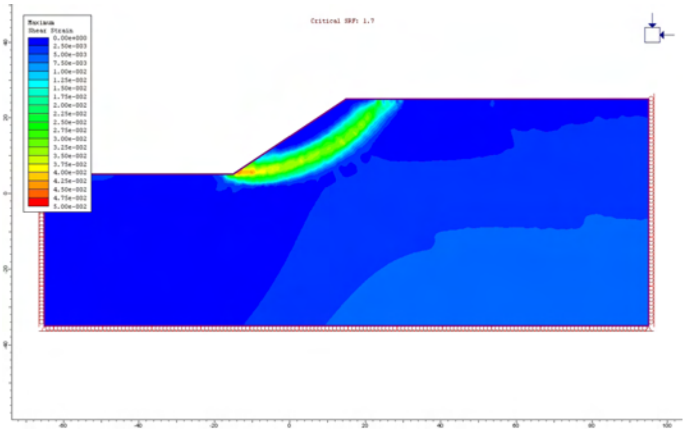

Figure 5.27: Maximum shear strains and deformed mesh when sliding occurs in the model (Piovano et al., 2011).

assumed for the ground during this stage with the material properties assigned as shown in Table 5.9. The fracture process was activated during the second stage with the intent to simulate the slope instability. During both stages computation was led to equilibrium.

5.5.4.1 In situ state of stress (Stage 1)

In order to initialize the state of stress in the slope prior to triggering instability, three different methods were adopted in Stage 1. The simplest method consisted in running to equilibrium by applying gravity to the model of Figure 5.24 (gravity-turn on). Initial in situ stress conditions were based on a horizontal to vertical stress ratio k of 0.67. Equilibrium was reached within $2 \cdot 10^6$ cycles.

An alternative method to set the initial state of stress was to simulate the erosion process by removing layers of elements in sequence, to create the slope. This method was tested with layers of different thickness equal to 5 and 2 m respectively. After the excavation of each layer, the computation was led to equilibrium. Figure 5.28 shows the model and the layers to be excavated. In these two cases the analyses required a greater number of cycles to reach the final equilibrium state: respectively $4.5 \cdot 10^6$ cycles and $12 \cdot 10^6$ cycles for the 5 m and the 2 m thick layer model.

Figure 5.29 shows the decrease of the total kinetic energy during Stage 1 for the three different analyses carried out. In all cases complete equilibrium is reached, with the number of cycles needed being different.

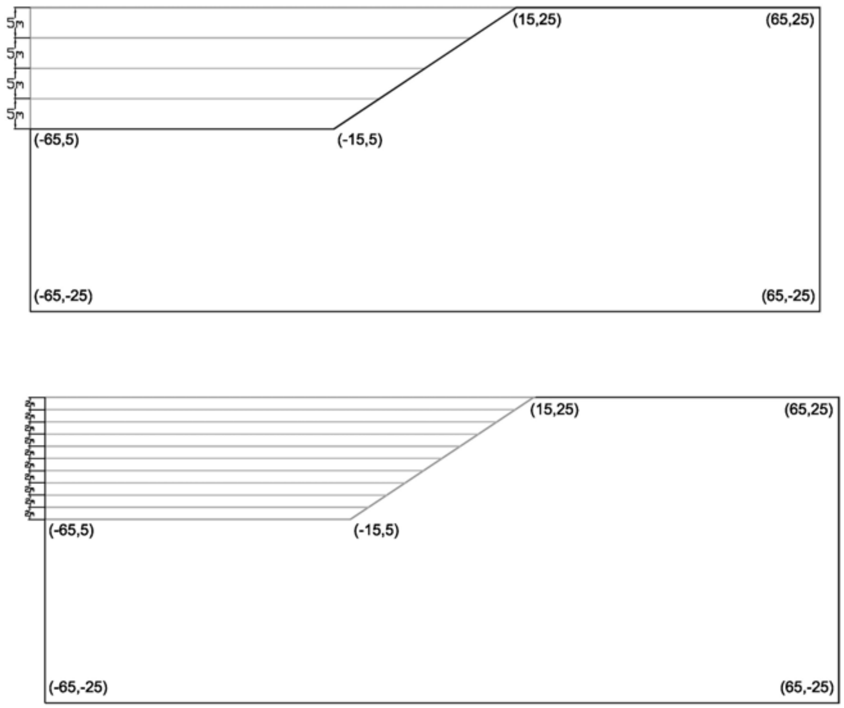

Figure 5.28: FDEM model with different excavation layers of 5 m and 2 m thickness (Piovano et al., 2011).

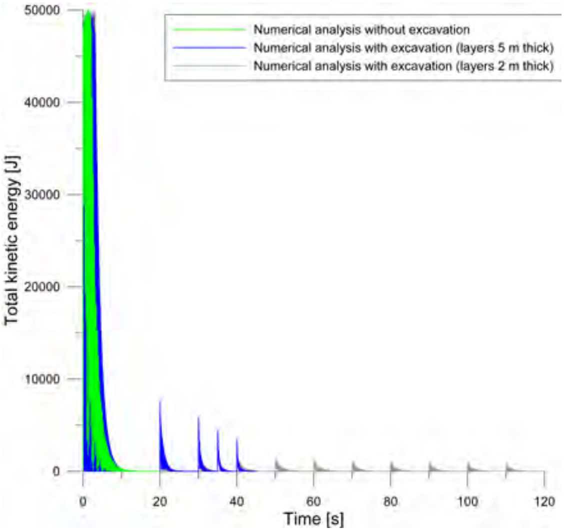

Figure 5.29: Total kinetic energy during Stage 1 in the FDEM simulation (Piovano et al., 2011).

In order to compare the results obtained, the vertical stress at a number of locations along three vertical lines (A, B and C) was monitored during computation. The monitored points are shown in Figure 5.30. Figure 5.31 compares the computed vertical stresses along the three vertical lines A, B and C with the expected theoretical values showing a good agreement. This is well evidenced along lines A and C, with limited scattering in the computed values resulting along line B. The results show that the best computed values of the vertical stress are obtained by the methods that include excavation. Nevertheless, the scattering among the different methods is not significant, thus leading one to conclude that the method to be preferred is that requiring less time to reach equilibrium. The number of cycles of the gravity turn-on analysis (no excavation is simulated) is 1/2 to 1/6 times that accounting for excavation. For this reason, the analyses described in the next subsection were run by using the results of Stage 1 given by the first method.

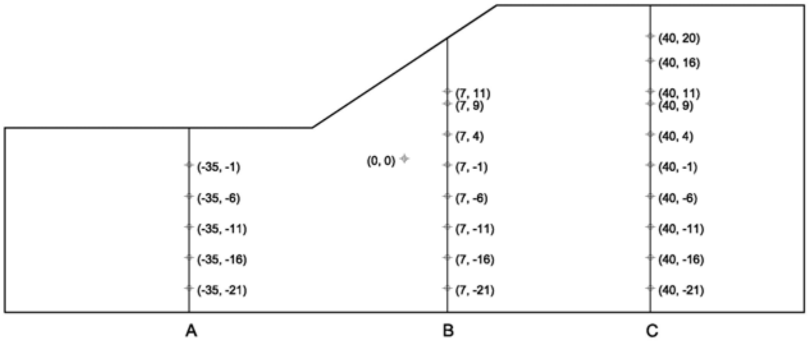

Figure 5.30: Monitored points during the FDEM simulation (Piovano et al., 2011).

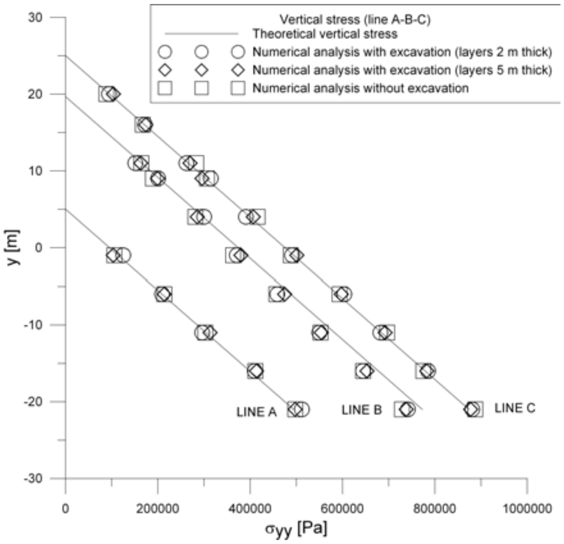

Figure 5.31: Comparison between computed with FDEM and expected vertical stresses along lines A, B and C (Piovano et al., 2011).

5.5.4.2 Computation of the factor of safety of the slope (Stage 2)

The second simulation stage was conducted to trigger slope instability and to determine the factor of safety, with the material now allowed to fracture. In order to calculate the factor of safety with the Y2D code the SSR method was reproduced with cohesion and friction coefficient being progressively reduced by a given factor, while the tensile strength was kept constant. The parameters which induce instability represent the critical ones allowing to compute the factor of safety of the slope (as the fraction between the real parameters and those triggering instability). Considering that the Y2D code is computer demanding this process is not straightforward and required a significant computation time (in terms of days) on a 2.33 GHz, 8 GB RAM pc.

In order to investigate the influence of the element size on the results obtained, Stage 2 was performed by adopting meshes with elements of different sizes (h). The SSR method to compute the factor of safety was first performed on a 4 m element size mesh and then repeated on a 2m, on a 1m and on a 0.5m element size mesh. A total of four element size meshes were tested.

Figure 5.32 shows a comparison of the plots at failure for the four types of mesh considered and the factors of safety obtained in the computations. The selection of the minimum factor of safety that triggers instability is not an automatic output of Y2D but needs to be based on personal judgement of the movie of subsequent screenshots. In this example the factor of safety selected is for a circular sliding surface involving the whole slope.

Figure 5.33 shows subsequent screenshots of the evolution of the slope instability for the case of the 0.5 m element size mesh. The influence of the element size is shown in Figure 5.34. It is noted that the results obtained with FDEM give a factor of safety which is dependent on the element size and converge to the results obtained with LEM and FEM.

Table 5.10 summarizes the computed factors of safety with the different methods. It is shown that the element size plays an important role on the results of the FDEM computations. If appropriate element sizes are used, the results compare satisfactorily well with those obtained by the well known methods (LEM and FEM-SSR), commonly adopted in design practice.

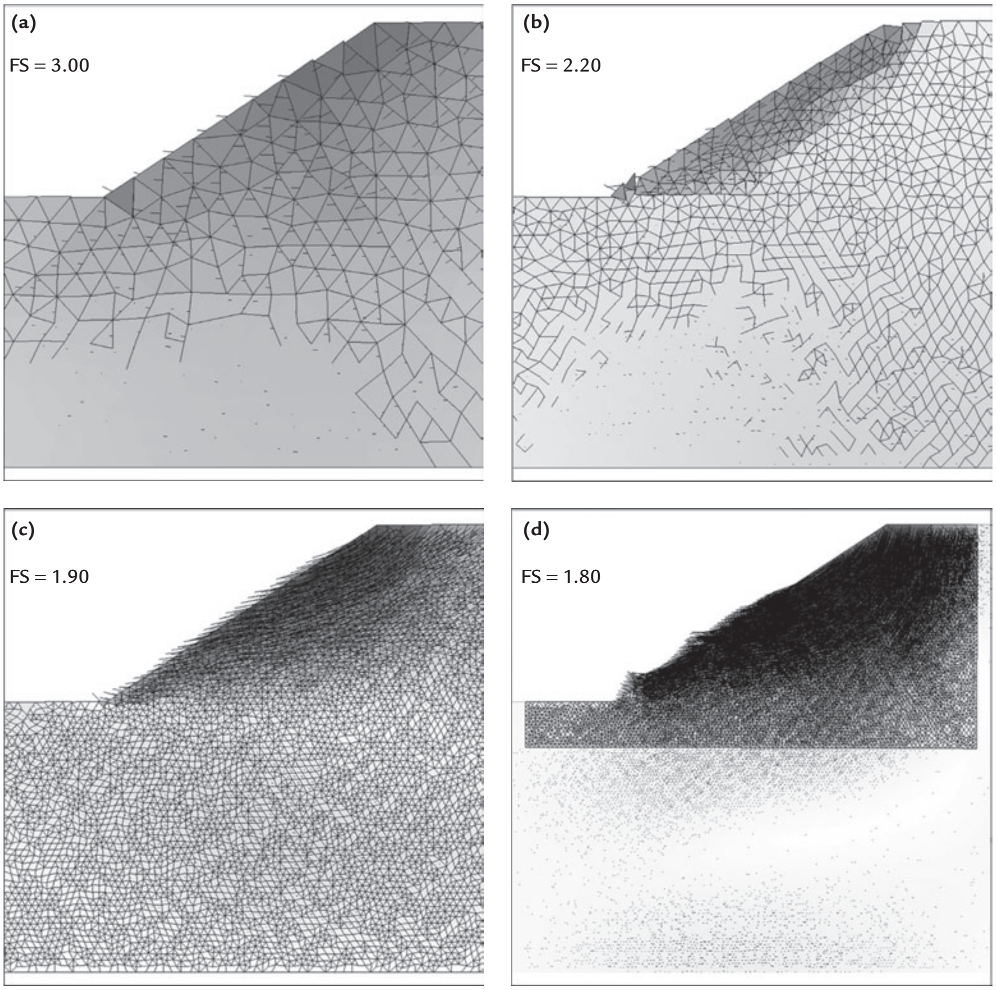

Figure 5.32: Displacement vectors and deformed assembly when instability is triggered in the FDEM model: (a) 4 m, (b) 2 m, (c) 1 m, (d) 0.5 m element size mesh. The value of the computed factor of safety is also shown (Piovano et al., 2011).

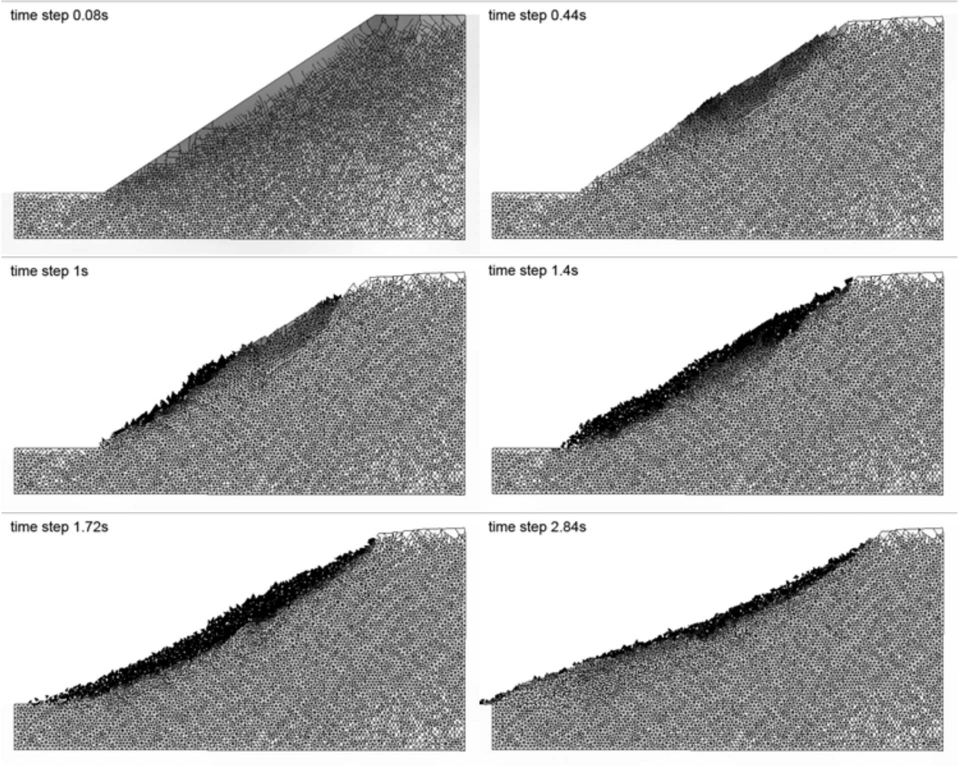

Figure 5.33: Subsequent screenshots of the slope instability simulated with FDEM (0.5 m element size mesh) (Piovano et al., 2011).

Computation method	*Factor of safety*
LEM	1.78
FEM-SSR	1.70
FEM/DEM	
4 m element size	3.00
2 m element size	2.20
1 m element size	1.90
0.5 m element size	1.80

Table 5.10: Computed factor of safety (Piovano et al., 2011).

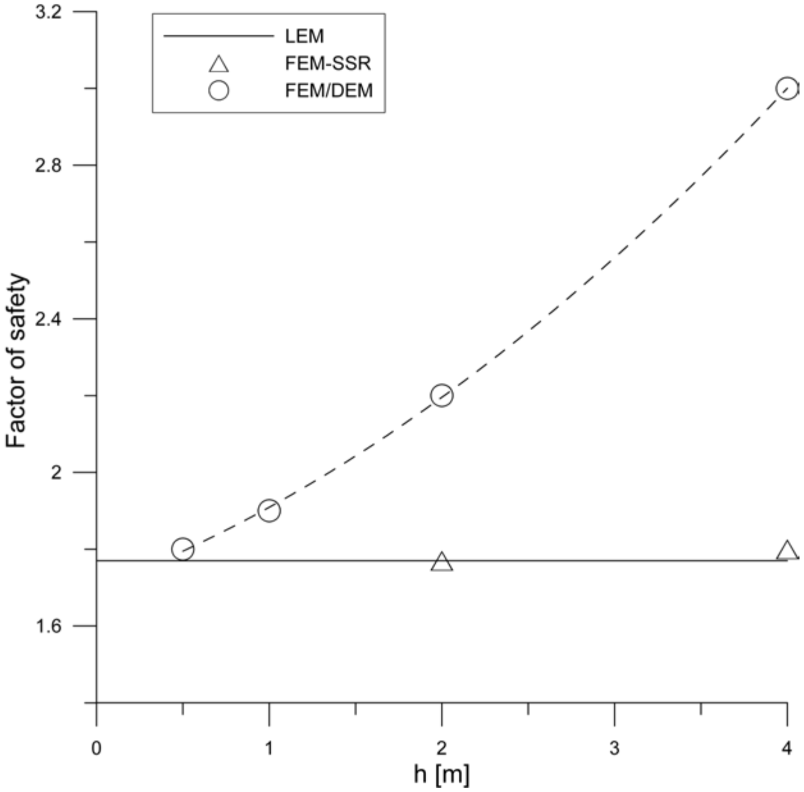

Figure 5.34: Factor of safety of the slope computed by the Y2D code versus the element size (Piovano et al., 2011).

5.6 Summary

Although individually both continuum and discontinuum numerical methods provide useful means to analyse rock slope stability problems, complex step-path failures which involve mechanisms related to both deformation along existing discontinuities and brittle fracture of intact rock, are better analysed with the combined finite-discrete element method (FDEM). This method was introduced as an effective alternative to conventional analysis methods. Since it can account for internal stress distribution, for the interaction between discrete bodies, and for the transition from continua to discontinua, it has the potential to overcome the drawbacks associated with conventional numerical techniques.

The first series of models presented is characterised by the assumption of pre-existing discrete discontinuities. The purpose has been to study typical slope problems with the Y2D code and to assess its potential in the analysis of simple instability mechanisms including sliding and block toppling.

The generation of a failure surface was analysed. The model indicated as “multi step-path failure” includes pre-existing sub-horizontal tectonic fractures. These fractures help to constrain the stepped development of the failure surface. Results show the generation of predominantly sub-vertical tensile fractures normal to the direction of downslope movement. As the density of fractures increases, a shear plane progressively develops perpendicular to them, forming a curvilinear failure surface typical of ductile failure.

The purpose of the block toppling study was to compare the results of the FDEM with the analytical solution. Further numerical simulations were performed to outline the advantages of the combined finite-discrete element method when compared with the explicit distinct element method (DEM).

The final example was dedicated to the study of the stability of an homogeneous slope using different methods such as the limit equilibrium method (LEM), the finite element method (FEM) and the combined finite-discrete element method (FDEM). The example involving a slope instability along a circular sliding surface, provides a validation of the combined approach.

References

Crook, T., Willson, S., Yu, J. G., and Owen, R. (**2003**). “Computational modelling of the localized deformation associated with borehole breakout in quasi-brittle materials.” *Journal of Petroleum Science and Engineering*, 38(3-4): 177–186.

Eberhardt, E., Stead, D., and Coggan, J. (**2004**). “Numerical analysis of initiation and progressive failure in natural rock slope - the 1991 Randa rockslide.” *International Journal of Rock Mechanics and Mining Sciences*, 41(1): 69–87.

Goodman, R. E. and Bray, J. W. (**1976**). “Toppling of rock slopes.” In “Rock Engineering for foundation and slopes ASCE,” volume 2, pages 201–234.

ITASCA Consulting Group, L. (**2004**). *UDEC 4.0 manuals*.

Karami, A. and Stead, D. (**2008**). “Asperity Degradation and Damage in the Direct Shear Test: A Hybrid FEM/DEM Approach.” *Rock Mechanics and Rock Engineering*, 41(2): 229–266.

Klerck, P. (**2000**). *The finite element modelling of discrete fracture of brittle material.* Ph.D. thesis, University of Wales, Swansea.

Mahabadi, O. K., Grasselli, G., and Munjiza, A. (**2010**). “Y-GUI: A graphical user interface and pre-processor for the combined finite-discrete element code, Y2D, incorporating material heterogeneity.” *Computers & Geosciences*, 36: 241–252.

Munjiza, A. (**2004**). *The combined finite-discrete element method*. John Wiley & Sons.

Munjiza, A., Owen, D. R. J., and Bicanic, N. (**1995**). “A combined finite-discrete element method in transient dynamics of fracturing solids.” *Engineering Computations*, 12(2): 145–174.

Piovano, G., Barla, M., and Barla, G. (**2011**). "FEM/DEM modeling of a slope instability on a circular sliding surface." In "13th International Conference of the IACMAG 2011 - Melbourne, Australia," pages 1–6.

Rocscience (**2007**). *Slide 5.0 manuals*. Rocscience Inc., Toronto, Ontario, Canada.

Rocscience (**2010**). *Phase2 7.0 manuals*. Rocscience Inc., Toronto, Ontario, Canada.

Sandia (**2009**). *Cubit 12.0*. Sandia National Laboratories.

Scavia, C. (**1990**). "Fracture mechanics approach to stability analysis of rock slopes." *Engineering Fracture Mechanics*, 35(4-5): 899 – 910.

Scavia, C. and Castelli, M. (**1996**). "Analysis of the propagation of natural discontinuities in rock bridges." In "Eurock '96," pages 445–451.

Singh, R. and Sun, G. (**1989**). "Fracture mechanics applied to slope stability analysis." In "International Symposium on Surface Mining - Future Concepts," pages 16–21. University of Nottingham, England.

Stead, D. and Coggan, J. S. (**2006**). "Numerical modelling of rock slopes using total slope failure approach." In S. G. Evans, G. Scarascia Mugnozza, A. L. Strom, and R. L. Hermanns, editors, "Landslides from Massive Rock Slope Failure," volume 49 of *NATO Science Series: IV: Earth and Environmental Sciences*, pages 129–138. Springer Netherlands.

Stead, D., Coggan, J. S., and Eberhardt, E. (**2004**). "Realistic simulation of rock slope failure mechanisms: the need to incorporate principles of fracture mechanics." In "International Journal of Rock Mechanics and Mining Sciences. SINOROCK 2004," volume 41, page 6.

Tharp, T. M. and Coffin, D. F. (**1985**). "Field application of fracture mechanics analysis to small rock slopes." In "Proceedings of the 26th U.S. Symposium on Rock Mechanics (USRMS)," pages 667–674.